UCONN LIBRARY

University of Connecticut
OpenCommons@UConn

Doctoral Dissertations | University of Connecticut Graduate School

10-11-2016

Co-operative Collective Motion of Benzoquinone Particles at the Air-Water Interface and Assessment of CD62L as a Protein Biomarker for Metastatic Bladder Cancer

Jennifer E. Satterwhite 4469944
University of Connecticut, jennifer.satterwhite@uconn.edu

Follow this and additional works at: https://opencommons.uconn.edu/dissertations

Recommended Citation
Satterwhite, Jennifer E. 4469944, "Co-operative Collective Motion of Benzoquinone Particles at the Air-Water Interface and Assessment of CD62L as a Protein Biomarker for Metastatic Bladder Cancer" (2016). *Doctoral Dissertations*. 1230.
https://opencommons.uconn.edu/dissertations/1230

Co-operative Collective Motion of Benzoquinone Particles at the Air-Water Interface and Assessment of CD62L as a Protein Biomarker for Metastatic Bladder Cancer

Jennifer Elizabeth Satterwhite, Ph.D.

University of Connecticut, 2016

Active matter is an entity observed in both animate and inanimate systems and exhibits spontaneous movement. An internal mechanism generates the self-driven unit to convert potential energy into mechanical movement. Biomotors and organisms are biologically well-known active systems; however, their movements are quite a complex phenomenon and understanding their driving motive forces and thermodynamic principles are essential. Therefore, the first portion of this thesis focused on the dynamics of an active multiple particle system at the air-water interface.

Benzoquinone active particles were studied and remarkable locomotion phenomena were observed at the air-water interface. Self-motion was evaluated with multiple symmetric circular disks, for which, spontaneous self-propulsion was observed alongside particle collisions and couplings, cycling and foraging for interfacial free energy fields at the interface. Initial studies demonstrated collective behavior could potentially be controlled by particle shape. Therefore, shape studies were conducted and a notable dynamic behavior merely between multiple irregularly shaped BQ collectives, termed *flocking* arose. This dissipative structure demonstrated perception-action capabilities as revealed by detection and response to thermotaxis and magnetotaxis conditions. Overall, collective self-motion with multiple particles was achieved and primitive thermodynamic principles emerged.

Cancer to-date is an incurable disease; while advances in research and technology have emerged, this disease remains the leading cause of death in the United States. Research cannot pinpoint a methodology proficient in detection, diagnosis, and surveillance. Current strategies remain a challenge due to the complexity of the disease, expense and invasiveness of the procedures. Therefore, development of a simple non-invasive test that specifies risk, stage, and reoccurrence is essential.

The manifestation of cancer involves alteration of protein levels (biomarkers). Biomarkers indicate and differentiate between diseased stricken and healthy states; therefore, a collection of biomarkers would lead to a more accurate and dependable diagnosis. Consequently, the second portion of this thesis involves assessing whether L-selectin (CD62L) can be acknowledged as a new bladder cancer biomarker; more precisely, be recognized as biomarker for metastatic bladder cancer. Assessment was reached by utilizing an established ultrasensitive online electrochemical immunoassay methodology. An eight-electrode nanostructured sensor was modified with CD62L capture antibodies. The sandwiched assay was complete upon antigen capture by magnetic beads massively labeled with both enzyme and secondary antibodies. Results demonstrated CD62L differentiated between bladder cancer stages; therefore, our established methodology revealed CD62L could act as a tumor marker for metastatic potential for distinctive bladder cancer stages.

Co-operative Collective Motion of Benzoquinone Particles at the Air-Water Interface and Assessment of CD62L as a Protein Biomarker for Metastatic Bladder Cancer

Jennifer Elizabeth Satterwhite

B.S., East Carolina University, 2010

M.S. East Carolina University, 2011

A Dissertation

Submitted in Partial Fulfillment of the

Requirements for the Degree of

Doctor of Philosophy

at the

University of Connecticut

2016

Copyright by

Jennifer Elizabeth Satterwhite

2016

APPROVAL PAGE

Doctor of Philosophy Dissertation

Co-operative Collective Motion of Benzoquinone Particles at the Air-Water Interface and Assessment of CD62L as a Protein Biomarker for Metastatic Bladder Cancer

Presented by

Jennifer Elizabeth Satterwhite, B.S., M.S.

Major Advisor

_____

Dr. James F. Rusling

Associate Advisor

_____

Dr. Mark W. Peczuh

Associate Advisor

_____

Dr. Jing Zhao

University of Connecticut

2016

Dedicated To

My husband, James Richard Warden
My parents, Mr. and Mrs. Jerry and Nancy Satterwhite
My late uncle, Uncle Carl Satterwhite

Acknowledgments

I would like to thank my research advisor, Dr. James F. Rusling for his wisdom, inspiration, and guidance to be fearless. I would like to thank Dr. Mark W. Peczuh and Dr. Jing Zhao for their constant support, valuable guidance, assistance and patience throughout my Ph.D. education. I am equally grateful for Dr. James A. Dixon for his guidance, diligence and valuable discussion during the course of our collaboration. I would like to acknowledge Dr. Edward Neth for being a teaching mentor and a part of my dissertation committee.

I extend my sincere gratitude to Gayatri Phadke for her dedication to our project, valuable and knowledgeable discussions, and for providing memorable moments on our Thursday nights out. I am also grateful for those that mentored and were a part of extending my scientific knowledge, thus thank you Dr. Colleen Krause, Dr. Brunah Otieno, Dr. Greg Bishop, Dr. Amit Joshi, Spundana Malla, and Karteek Kadimisetty.

To my friends that allowed my journey at UCONN to be memorable inside and outside of the Chemistry Department, please accept my sincere appreciation. Jill, thank you for being my meatball, but most importantly for answering every call and always being there. Julie, Kelli, and Nicole thank you all for always keeping my text notification above 10 a day, but most importantly for the bond we shared outside of the department. Chris Dietz, thank you for gracing us with your presence.

Thank you to my compassionate, remarkable husband, James Warden. I appreciate your undeniable support, but most importantly the sacrifice you made for me to achieve my dream. Lastly, thank you to my astounding parents, Mr. and Mrs. Jerry Satterwhite with who no gratitude suffices to show my appreciation for all of their passion shown during every life stage.

Table of Contents

Approval Page……..**v**
Dedication Page……..**vi**
Acknowledgments……**vii**
Table of Contents……..**viii**
List of Figures……...**xiii**
List of Schemes……..**xx**
List of Tables……**xxi**

Chapter 1: Introduction……**1**

1.1 Part One: Introduction for Co-operative Collective Motion of Benzoquinone Particles at the Air-Water Interface ……...**1**

1.1.1 Background and Significance of Motion……**1**

1.1.2 Active Systems……**2**

1.1.3 Basic Illustrations of Self-Organized Active Matter……...**3**

1.1.4 Thermodynamic Equilibrium and Nonequilibrium Systems……...**5**

1.1.5 Thermodynamics of Self-Organization in Far-From Equilibrium Systems……**7**

1.1.6 End-Directed Evolution……**10**

1.1.7 Electrically Driven Nonequilibrium System – Analogous to Chemical System...**12**

1.1.8 Self-motion in Chemical Systems……..…**16**

1.2 Part Two: Introduction for Assessment of CD62L as a Protein Biomarker for Metastatic Bladder Cancer……..……...…**19**

1.2.1 Background and Significance……**19**

1.2.2 Current Cancer Detection Methodologies……..…**22**

1.2.3 Cancer Biomarker……..**23**

1.2.4 Point-of-Care Detection Systems……...**25**

1.2.5 Electrochemical-Based Protein Detection……..…**28**

1.2.6 Microfluidic Electrochemical Immunoassay Detection…….**31**

1.3 Overview of Dissertation……...**35**

1.4 References……..……....**37**

Chapter 2: Co-operative Self-Motion of Multiple Benzoquinone Disks at the Air-Water Interface……**43**

2.1 Abstract……..**43**

2.2 Introduction……**43**

2.3 Experimental…….…**46**

2.3.1 Chemicals and Materials……**46**

2.3.2 Methods……..**46**

2.3.2.1 Benzoquinone Disk Preparation……**46**

2.3.2.2 Concentration Evaluation Protocol……..…..**46**

2.3.2.3 Monitoring Process of Self-Motion……...…**47**

2.4 Results……**47**

2.4.1 Continuous motion for Benzoquinone Disks…….**47**

2.4.2 Cooperative Collisions of Multiple Benzoquinone Disks……..…**49**

2.4.3 Cooperative Coupling of Multiple Benzoquinone Disks ……..…**50**

2.4.4 Evaluation of Concentration Gradient Formation……..**53**

2.4.5 High Frequency Cycling of Asymmetric Benzoquinone Disks……..…**54**

2.4.6 Evaluation of Driving Motive Force of Self-Motion…….**55**

2.4.7 Collective Cooperative Motion for Irregular Benzoquinone…….**56**

2.4.8 Effect of Salt Concentration on Self-Motion……..…**58**

2.5 Discussion……..**59**

2.5.1 Explanation for Emergence of Spontaneous Continuous Self-Motion……**59**

2.5.2 Explanation for Emergence of Disk Collisions……**61**

2.5.3 Explanation for Cooperative Disk Coupling……**63**

2.5.4 Rationalization for Asymmetrical Disk Locomotion……**63**

2.5.5 Interpretation of Driving Motive Force of Self-Motion……**64**

2.5.6 Collective Cooperative Motion of Irregularly Shaped Benzoquinone Particles…**64**

2.6 Conclusion……**67**

2.7 Acknowledgments……**68**

2.8 References……**69**

Chapter 3: Flocking, Thermo-taxis, and Magneto-taxis in Collective Active Matter Benzoquinone Particles at the Air-Water Interface……**71**

3.1 Abstract……**71**

3.2 Introduction……**72**

3.3 Experimental……**75**

3.3.1 Materials……**75**

3.3.2 Methods……**76**

3.3.2.1 Preparation of Benzoquinone Circular Disks and Irregularly Shaped Particles……**76**

3.3.2.2 Protocol and Evaluation Process for Self-Motion at the Air-Water Interface.....**76**

3.3.2.3 Experimental Procedure and Conditions for Thermotaxis……**77**

3.3.2.4 Investigational Process and Experimental Conditions for Magnetotaxis…**77**

3.3.2.5 Assessment Practice for Determining the Rate of Entropy Production.....**78**

3.4 Results……**78**

3.4.1 Flock Structure Formation……**78**

3.4.2 Thermotaxis of the Flock……**80**

3.4.2.1 Warmer Temperature Conditions……**80**

3.4.2.2 Cooler Temperature Conditions……**82**

3.4.3 Magnetotaxis and Control of the Flock……**83**

3.4.3.1 Magnetotaxis of the Flock Structure……**83**

3.4.3.2 Evaluation of the Magnetotaxis with Control Experiments……**85**

3.4.4 Statistical Analysis on a Flock……**87**

3.5 Discussion……**89**

3.5.1 Flock Formation……**91**

3.5.2 Thermotaxis on the Flock……**93**

3.5.3 Magnetic Sensing by the Flock……**95**

3.5.4 Rate of Entropy Production of the Flock……**96**

3.6 Conclusions……**101**

3.7 Acknowledgments……**102**

3.8 References……**103**

Chapter 4: Online Microfluidic Protein Capture Electrochemical Assay of CD62L for the Assessment of Metastasis in Bladder Cancer……**106**

4.1 Abstract……**106**

4.2 Introduction……**107**

4.3 Experimental……**110**

4.3.1 Materials……**110**

4.3.2 Methods……**111**

4.3.2.1 Fabrication of Microfluidic System Device Chambers…….……**111**

4.3.2.2 Immobilization of Proteins to Form Immunoarray Sensor……..……..…**112**

4.3.2.3 Preparation of Bioconjugates……**114**

4.3.2.4 On-line Capture and Detection Protocol……...**115**

4.3.2.5 Patient Sample Analysis and Data Processing……..…**116**

4.4 Results……..…**117**

4.4.1 Optimization of Enzyme Label……**117**

4.4.2 Optimization of Antibodies for Protein CD62L……..**117**

4.4.3 Immunoarray Standard Calibration of Protein CD62L……**119**

4.4.4 Assay Validation Using Spiked Calf Serum Samples…….**121**

4.4.5 Bladder Cancer Patient Serum Sample Analysis…….**122**

4.5 Discussion……**123**

4.5.1 Modification of Immunoassay Protocol……...**123**

4.5.2 Assessment of Soluble CD62L Level for Staging Bladder Cancer…….**124**

4.5.3 Investigation of Differential Recoveries for ELISA and Immunoarray……..**127**

4.5.2 Statistical Studies on Immunoarray vs ELISA Data……**129**

4.5.2.1 T-Test Analysis for Assay Accuracy with Spiked Sample Analysis……**129**

4.5.2.2 Assay Validation for Patient Sample Analysis with T-Tests……**131**

4.5.2.3 Assessing Specificity of Immunoarray Method in Bladder Cancer Tumor Staging……...**132**

4.6 Conclusions……..**134**

4.7 Acknowledgments……**136**

4.8 References……**137**

List of Figures

Figure 1.1: Examples of self-organized dissipative collective motion in biological systems. A) Bacterial colony swimming from a central colony and leaving trace of bacteria behind. B) Collections of cytoskeletal filament within living cells. C) Slime mold aggregating or forming fruiting bodies when deficient and in search of food. D) A school of thousands of fish E) A flock of thousands of starling birds. F) Swirling tornado.……**4**

Figure 1.2: Three classified thermodynamic systems. A) An isolated system exchanges neither energy nor mass, B) A closed system that exchanges energy but not matter with the surroundings. C) Open system that interchanges both energy and mass with the surroundings….**6**

Figure 1.3: The exchange of entropy between the system and surrounding. …….**9**

Figure 1.4: Schematic illustration of the basic experimental setup for the voltage-driven self-organized system Adapted and reprinted with permission from Reference 36……..…**13**

Figure 1.5: Extracted example from video analysis of the organism-like dynamic filamentous dissipative structure that is formed during the electrically-driven system. ……..**15**

Figure 1.6: Evolution of the tree structure formation at four different time snapshots and the corresponding rate of entropy production output during the formation of the tree structure. Once the dissipative tree structure forms and makes contact with the ground electrode, there is a distinctive sharp increase in Σ. Adapted and reprinted with permission from Reference 36……**15**

Figure 1.7: Illustration of the bladder demonstrating depth of cancer invasion into bladder wall for the five different stages of bladder cancer. …….**21**

Figure 1.8: The gold standard ELISA based assays with individual wells coated with the capture primary antibody, which is specific and selective to the target protein. A conjugate solution with

labeled detection antibody incubates on the surface and selectively binds; therefore, when substrate is added a color change occurs and is proportional to target protein concentrations….**26**

Figure 1.9: A single carbon electrode with a sandwiched immunoassay coated on the surface. Secondary detection antibody is labeled with an electroactive enzyme, where a cyclic voltammogram is acquired upon generation of electrons at the electrode surface via a catalytic reduction-oxidation cycle with horseradish peroxidase (HRP). ……...**30**

Figure 2.1: Extracted [x,y] trajectories for a single BQ disk from a 4 BQ disk experiment over a 12 min time frame. The [x,y] pixel trajectories demonstrates the clockwise circular motion observed during symmetrical disk shape.……..**41**

Figure 2.2: Illustration of BQ particle collisions. A) Superimposed snapshots at 1 s time intervals demonstrating the progression of BQ particle collision. Two different 3 mm BQ disk voyage from different directions [1] collide with one another [2] then deflect in different trajectories [3]. B) A linear increase in the number of collisions was observed during a 20 min time frame as the number of BQ disks contained in a single dish increased (black line). Blue line from theory of random collisions, calculated by the empirical formula (**Equation 2.1**)……..**50**

Figure 2.3: Illustration of two BQ particles voyaging in tandem. A) Superimposed snapshots at 1 s time intervals demonstrating the progression of BQ particle coupling. B) A linear increase in the number of couplings was acquired during a 20 min time frame as the number of BQ disks contained in a single dish increased……...**51**

Figure 2.4: Snapshots at 1 sec time intervals for 10 BQ disks, individual numbered, contained in a single petri dish. Each frame demonstrates multiple co-operative coupling events can occur and through self-motion the co-operative couplings may acquire other BQ disks. ……**52**

Figure 2.5: Concentration of BQ for each particle series acquired at different time variations to demonstrate heterogeneous BQ dissolution during self-motion progression. Change in concentration was estimated using a standard BQ calibration curve…….**54**

Figure 2.6: Trajectories demonstrating high frequency cycling were observed once the BQ particle becomes irregularly shaped. (A) Full [x,y] trajectories for 1 BQ disk from a 4 BQ disk series. B) Superimposed snapshots at 0.5 s time intervals to illustrate the irregular BQ particle shape. C) Extracted [x,y] trajectories after 12 min of self-motion to represent high frequency cycling…….**55**

Figure 2.7: Superimposed snapshots at 4 s time intervals demonstrating the collective motion of multiple irregularly shaped BQ particles. The initial position of particles is shown in green [1] after 4 s of translational motion collectively they travelled to position [2] and after an additional 4 s of translational motion the collectives groups were at position [3]. Individual particles maintained their own characteristic motion. …….**57**

Figure 2.8: Extracted the superimposed snapshots at 4 s time intervals of Figure 7B to highlight the flocks described in the Results section. A) Blue circle around green BQ pieces highlights two co-operative flocks formed during self-motion. B) Blue circle around yellow BQ pieces highlights one co-operative flock that formed after an additional 4 s translational motion. C) Blue circle around pink pieces highlights the new co-operative flock that transpired after an additional 4 s translational motion. …….**58**

Figure 2.9: Schematic representation of mechanism for BQ self-motion on water surface. A) Surface tension (γ) fields are shown for $\boldsymbol{\gamma}_{SW}$ (solid-water), $\boldsymbol{\gamma}_{AW}$ (air-water), and $\boldsymbol{\gamma}_{SA}$ (solid-air) B) Illustration of net interfacial tension force (F) C) Diagram of attractive interactions between BQ disks…….**60**

Figure 3.1: Illustration of collective, flocking structure formation among 15 irregularly shaped BQ particles at 30 s time intervals. Please view **Video S1** (ESI). ……**80**

Figure 3.2: Snapshots at different time intervals and the corresponding temperature gradient for 15 irregularly shaped BQ particles under warm thermotaxis conditions. A) Particle addition to the surface lead to flock formation B) under ambient conditions, then C) after 7 s of self-motion the in-house temperature probe was added to the interface and the assembly began to migrate to the D) warmer conditions seen by the small purple and blue diameter circle, and then E) at 30 s a majority of the particles were hovered and continued to voyage around F) the warmer temperature zone seen by larger purple diameter. Please view **Video S3.2** (ESI). ……..**81**

Figure 3.3: Snapshots at different time intervals and the corresponding temperature gradient for 15 irregularly shaped BQ particles under cold thermotaxis conditions. A) Particle addition to the surface lead to grouped collections B) under ambient conditions, then C) after 15 s of self-motion the in-house cold probe was added to the interface and the assembly migrated in the opposite direction of the D) cooler conditions seen by small red zone, and then E) at 25 s a majority of the particles continued voyaging distant the probe F) the cooler temperature zone seen by larger dark green and red diameter region. Please view the **Video S3.3** (ESI) ……...**83**

Figure 3.4: Illustration of a BQ flocking collective, constructed of a single sensor element (circled in red) and 14 non sensor elements, sensing the addition of a magnetic field. See **Video S3.5** (ESI). ……**85**

Figure 3.5: Snapshots of a BQ flocking collective, constructed from 15 non-sensor elements. The flocking structure was incapable of sensing the addition of a magnetic field due to the absence of the sensing BQ-iron oxide element. See **Video S3.6** (ESI). ……...**86**

Figure 3.6: Snapshots of 1 sensor BQ-iron oxide 3 mm disk (circled in red) and 14 self-moving 3 mm BQ circular non-sensor disk elements at the interface, which were incapable of flock formation and sensing the addition of a magnetic field. See **Video S3.7** (ESI). ……..**87**

Figure 3.7: Trajectory traces of the irregularly shaped BQ fragments at the air-water interface for particle series A) four, B) six, C) eight, D) ten, E) twelve, and F) fifteen. ……**89**

Figure 3.8: Surface tension measurements at different concentrations of aqueous 100 mM solutions of BQ……..**91**

Figure 3.9: Comparison of both particle number and shape when $\ln(C_o\text{-}C)$ versus time was plotted and tabulated from time variation UV measurement studies. ……**100**

Figure 3.10: Plot of rate constant, extracted from the slopes in **Figure 3.9**, versus the number of BQ particles in the petri dish during time variation UV absorption studies. ……..…**101**

Figure 4.1: Schematic illustration of microfluidic in-house machined devices. A) The online capture chamber device for which the target protein becomes captured by heavily labeled bioconjugates to form the protein-antigen bioconjugates. B) The detection chamber device that houses the Ab_1 modified working electrode array, counter wire electrode, and reference wire electrode.……..**112**

Figure 4.2: Schematic illustration of the online-capture microfluidic assay. A) Strategy for modified ELISA was performed on B) a modular semi-automatic setup, where MB-Ab_2-HRP conjugate was incubated with antigen in an online capture chamber and then flowed to the detection chamber for incubation with surface-bound primary antibodies. C) 1 mM HQ and 0.1 mM H_2O_2 was injected for quantitative amperometric detection……**113**

Figure 4.3: Optimization results for CD62L sandwich immunoarray performance upon employing standard concentrations of 0, 1 and 10 ng mL^{-1}. A) Optimization of Biotin-HRP using consistent Ab_1 and Ab_2 concentrations. Optimal concentration of biotin-HRP was determined to be 0.5 mg mL^{-1}. B) Optimized result for secondary antibody (Ab_2) using consistent Ab_1 and biotin-HRP label concentrations. Optimal concentration of Ab_2 was determined to be 10 μg mL^{-1} and C) Optimized outcome for primary antibody (Ab_1) using consistent Ab_2 and biotin-HRP label concentrations. Optimal concentration of Ab_1 was determined to be 100 μg mL^{-1}.....**118**

Figure 4.4: Calibration for protein CD62L standard was performed in 5-fold diluted calf serum and current signals were acquired by injecting a mixture of 1 mM HQ and 0.1 mM H_2O_2 at -0.2 V vs. Ag/AgCl. A) Reduced HRP acquired calibration plot and B) amperometric current signals with a dynamic range from 0.25 ng mL^{-1} to 100 ng mL^{-1}. C) Unreduced HRP attained calibration plot and D) amperometric current signals with dynamic range from 4.88 pg mL^{-1} to 625 pg mL^{-1}.....**120**

Figure 4.5: Amperometric signals to demonstrate assay reliability and stability. A) Current signals from four independent days for 0, 1, and 10 ng mL^{-1} CD62L. B) Comparison of current signals indicating stability of surface bound Ab_1 on the LBL sensor array over duration of one week for 0, 1, and 10 ng mL^{-1} CD62L.....**121**

Figure 4.6: A comparison of our immunoarray results versus ELISA with known spiked levels (75, 250, 350, 550, 700, 1500, 3000 and 5500 ng $mL^{-}1$) of CD62L standards in calf serum. Recovery was observed to be within 83%–116% for our immunoarray and 37–97% for standard ELISA. B) Zoomed inset for spiking levels 75, 250, 350, and 550 ng mL^{-1}. **122**

Figure 4.7: Dot box plot analysis for 41 patient samples for four different subsets tumors (healthy, low-grade, high-grade non-metastatic, and high-grade metastatic). A) ELISA B) Electrochemical Immunoarray, for which red dots represent individual recovered patient sample concentrations. Box plot height represents the mean and error bars were plotted at 1 standard deviation of the mean.……..**125**

Figure 4.8: Receiver operating characteristic (ROC) curves comparing A) healthy vs. all cancer patient samples, B) healthy vs. low-grade C) healthy vs. high-grade non-metastatic, D) healthy vs. high grade metastatic, E) low-grade vs. high-grade non-metastatic, F) low grade vs. high-grade metastatic, and G) high-grade non-metastatic vs. high-grade metastatic. ……**126**

Figure 4.9: Linear correlation plots for both our immunoarray detection method and standard ELISA for protein CD62L. A) Plot of immunoarray results against ELISA for detection of CD62L in human serum samples from patient samples. B) Relationship between spiked sample recoveries for our immunoarray system against ELISA. C) Comparison result of known spiked level versus detected ELISA. D) Correlation outcome between spiked known CD62L level and detected level for the immunoarray…….**128**

List of Schemes

Scheme 1.1: The first generation offline capture microfluidic electrochemical immunoassay system with A) syringe pump that flows solutions through B) sample injector that allows protein conjugates to be injected and incubated in C) detection chamber that houses 8-electrode modified array that is then connected to D) multipotentiostat to apply a set potential with time for which a readout of current will be acquired by E) computer…….**32**

Scheme 1.2: Schematic representation of the second generation electrochemical microfluidic immunoassay system. Online capture and detection system features A) syringe pump to push solution through B) the sample injector C) and switching valves allowing the direction of flow to be altered to either D) reaction chamber which captures proteins on magnetic bioconjugates or E) detection camber where the 8-electrode is housed for completion of sandwiched assay that will be detected by F) the multipotentiostat and an electrochemical response will be recorded by G) computer……**34**

List of Tables

Table 1.1: Contrasting the notions of designed structures and dissipative structures……...**11**

Table 1.2: Urinary bladder cancer assays that are FDA-approved……...**28**

Table 4.1: ROC analysis parameters for combination of four patient sample subsets……..

Table 4.2: Statistical results for Linear Regression T-Test was performed for correlation plot slopes at 95% CI.……

Table 4.3: Statistical results for One Sample Mean T-test and Two Sample Mean T-Test performed at 95% CI for spiked samples (n = 3 for Immunoarray, n = 2 for ELISA)……

Table 4.4: Two Sample Mean T-Test at 95% CI to demonstrate differential CD62L protein level in patient sample subsets.……

Table 4.5: Statistical results from Paired T-test for each bladder cancer tumor subset across all intra-subset samples at 95% CI.……

Chapter One:

Introduction

1.1 Part One: Introduction for Co-operative Collective Motion of Benzoquinone Particles at the Air-Water Interface

1.1.1. Background and Significance of Motion

Aristotle, more than 2000 years ago, separated everything in the natural world into two categories, non-living objects and living organisms. More specifically, a distinction between the two categories was founded on motion, as only living organisms have locomotion without external driving forces. Presently, living organisms have been acknowledged to have a more complex internal architecture, covering a wide range of scales.[1, 2, 3] These ranks of structural hierarchy are each dynamically active and demonstrate complex movements on different time scales. [1, 2, 3]

Since life is dependent upon function to maintain order, function relies on consumption of energy. In particular, living organisms dissipate chemical energy into mechanical energy, enabling mechanical activity of the organism. [4, 5, 6] Molecular motors and motile cells are both examples of an organism, which directly converts chemical energy of a chemical substance, such at adenosine triphosphate (ATP), into mechanical work without thermal transfer required.[7] Details of the aforementioned spontaneous motion in living systems have been actively researched; however, our comprehension of the underlying mechanism remains at the primitive stage.[8, 9, 10] Lack of understanding arises as the study of actual living organisms can be complex due to a huge variety of involved elements and determination of which element plays a crucial

role for generation of locomotion. Therefore, we believe there must be scientific value to studying non-living systems to gain enhanced insight on the underlying thermodynamic mechanisms for spontaneous motion.

1.1.2. Active Systems

A distinguishing feature for living systems is the phenomenon called locomotion. This ability to be active under conditions, in which the influx and dissipation of free energy exist constantly, diverges from an equilibrium state. Systems comprising of energy fluxes and motion is achieved spontaneously by generating kinetic energy from itself is "far from equilibrium" and termed "active matter".[11, 12, 13] Active matter is an entity constructed of self-driven units (or active particles), which independently self-propel by converting potential energy or stored free energy into systematic movement.[11, 12, 13] These are highly nonequilibrium systems that display novel behaviors compared to systems in equilibrium. According to the description, it thereby means a single self-driven unit is indicatively active matter; furthermore, the size of the active particle can vary per system.[13] Although the individual active particles can be different, the active matter system overall shares collective behaviors.[13]

The emergence of active matter is observed from biological living systems to inanimate materials. The internal mechanism of motion can involve chemical reactions on the interface to complicated processes within a particle; however, in each scenario, kinetic energy is generated, and due to this, active matter exhibits dynamical motion.[14, 15] There are a number of dynamical types of active motion such as, spontaneous translation motion, spontaneous rotational motion (or cycling), and spontaneous deformation.[14, 15, 16] Additionally, a distinctive dynamical phenomenon observed is particle self-motion in conjugation with cooperative association

interactions for the emergence of a large scale coherent dissipative structure.[13] Self-organization among active particles is a prominent feature of active systems far-from-equilibrium.

1.1.3. Basic Illustrations of Self-Organized Active Matter

Active systems, as described above, provide an opportunity to place artificial systems on the same stage as biological systems. Overall, the goal is to bridge the gap between artificial active particle systems and biological organisms, which self-organize, to acquire an enhanced understanding of the underlying thermodynamic principles that drive their collective motion. Once the fundamental principles are established, these principles can be implemented alongside other emergent properties to develop artificial systems that have perception-action and task-driven cooperative capabilities. Active matter includes common everyday biological systems and countless effort has currently been imparted to understanding thermodynamic principles, to accomplish, various types of artificial active matter systems have been developed to lower the complexity and begin to understand fundamentals.

Biological processes and living systems are composed of myriad active matter examples from small subcellular processes to large-scale coordinated behaviors in humans, as illustrated in **Figure 1.1**.[14] Small motor protein elements and biofilaments within the body polymerize and depolymerize in conjugation with adenosine triphosphate to produce treadmilling motion.[17] These processes are the driving motive mechanism in living cells that enable the cell to exhibit dynamical motions spontaneously.[18, 19] Alternative small level component self-organization examples include suspensions of swimming bacterial colonies, cell suspensions of motile microorganisms and aggregation of slime mold.[20, 21, 22] The spectrum of biological systems is not limited to the subcellular level there are group motions widely exhibited at the global level such

as migrating locusts, schools of fish, flocks of birds and groups of mammals (including people).[23, 24] Furthermore, the dynamically changes in the climate on the earth, such as whirling storms and galaxies, are each examples in which energy is continually supplied to the systems many interacting constituents.[25] For each, self-organization, or pattern formation, develops and provides the overall structure with dynamical behaviors. While these far-from-equilibrium living system processes span an immense range of time and dimension scales these are all dissipative structures.

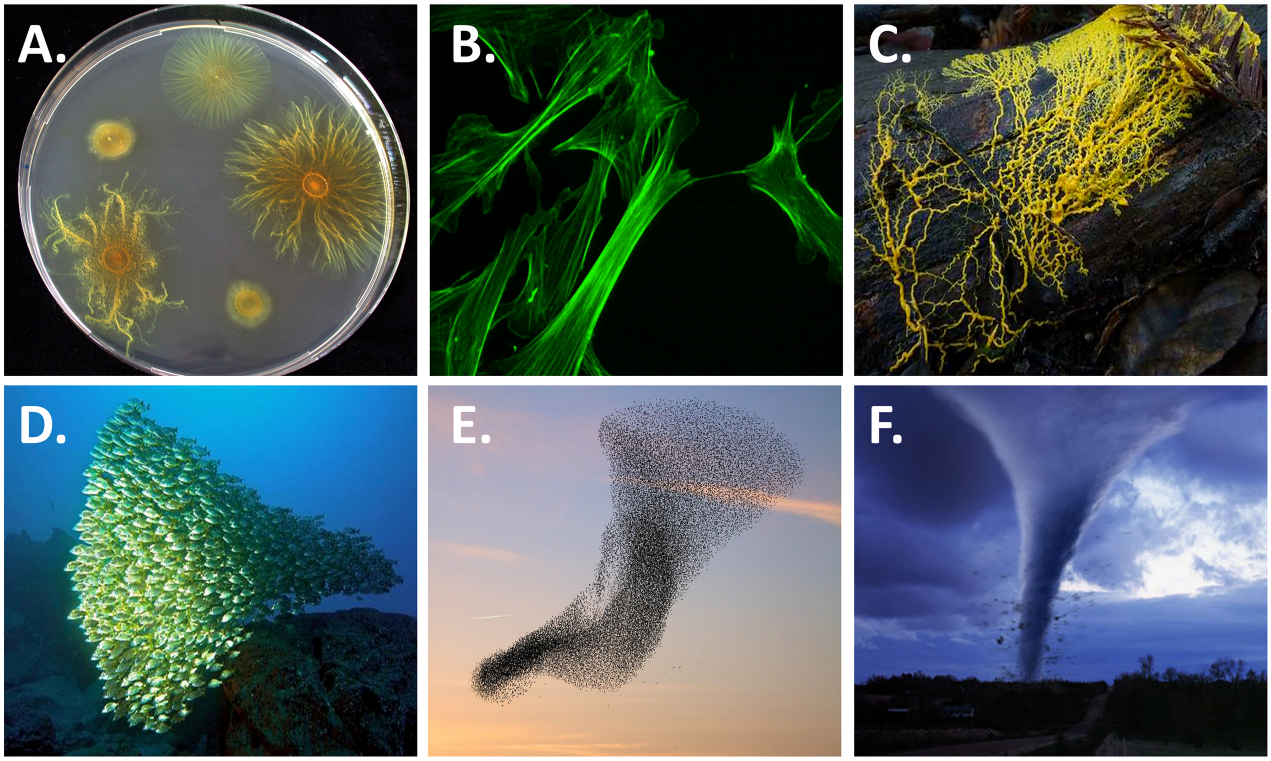

Figure 1.1: Examples of self-organized dissipative collective motion in biological systems. A) Bacterial colony swimming from a central colony and leaving trace of bacteria behind. B) Collections of cytoskeletal filament within living cells. C) Slime mold aggregating or forming fruiting bodies when deficient and in search of food. D) A school of thousands of fish E) A flock of thousands of starling birds. F) Swirling tornado.

1.1.4. Thermodynamic Equilibrium and Nonequilibrium Systems

Thermodynamic descriptions are understood by dividing the world into a "system" and the corresponding "surrounding", or rest of the world.[26] However, the definition of these systems depends on the "boundaries" that separate the system from its surrounding and the corresponding interactions. To comprehend thermodynamic behavior, the approaches in which energy and matter are exchanged with the surrounding are essential. Consequently, three thermodynamic systems have been defined and illustrated in **Figure 1.2**, isolated, closed, and open, and the classifications were based upon the way they interact with the exterior.[26]

Isolated systems, **Figure 1.2A**, experience no change or exchange with energy or matter from the surrounding. Such systems, no unbalanced potentials (or driving forces) within the system are in a state of equilibrium. [26] The word equilibrium implies a state of balance; therefore, there are no net flows of mass or energy. Such systems are generally considered for educational reasons, because truly isolated system do not exist in nature, except for the universe as a whole.

Closed systems, such as Earth or closed flask, exchange energy with the surrounding but there is no interchange of matter as illustrated in **Figure 1.2B**.[26] More specifically, over time Earth only absorbs radiation from the sun and then this is emitted back into space, during which there is negligible exchange in the amount of matter to the exterior. All living and ecological systems on Earth, however, are open systems. Open systems can exchange both energy and mass (**Figure 1.2C**) with the surroundings. Both closed and open systems are in a state of non-equilibrium. [26]

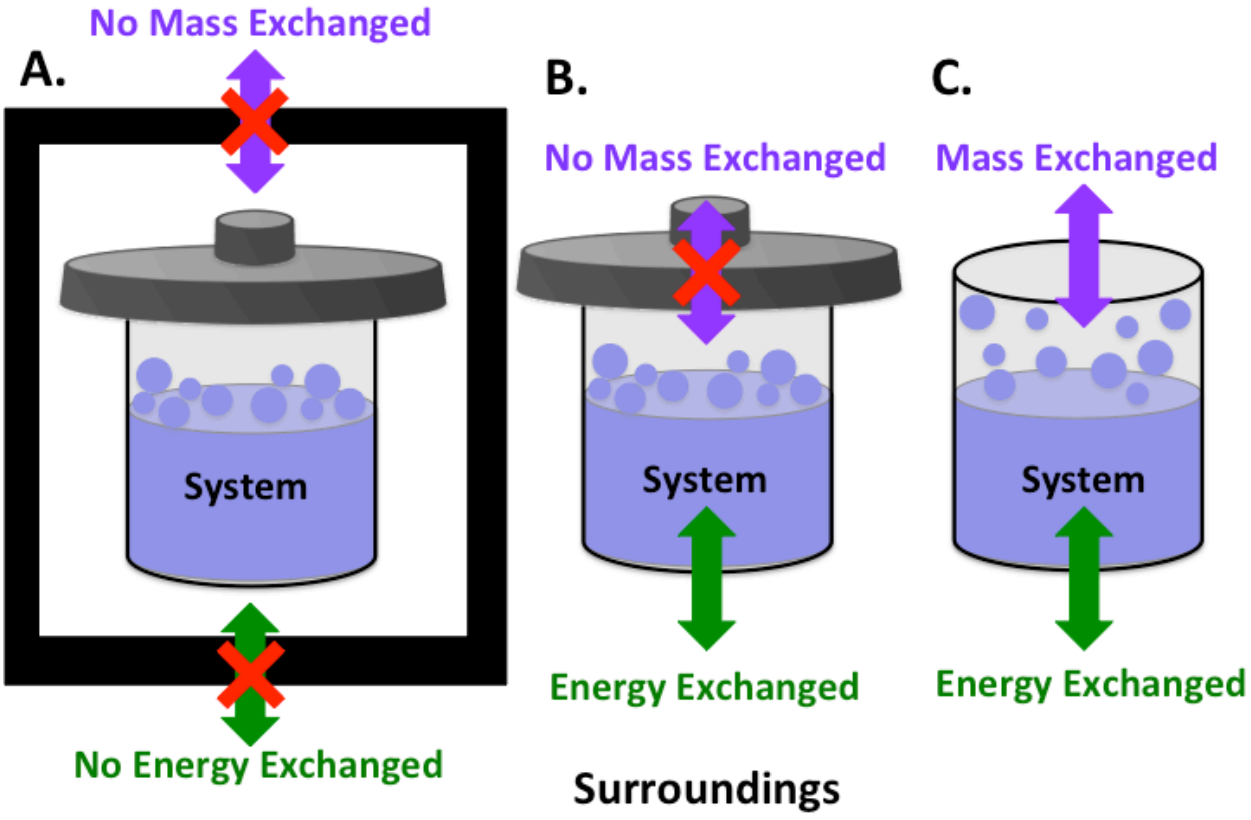

Figure 1.2: Three classified thermodynamic systems. A) An isolated system exchanges neither energy nor mass, B) A closed system that exchanges energy but not matter with the surroundings. C) Open system that interchanges both energy and mass with the surroundings.

While isolated systems progress toward equilibrium, much richness of the world arises from conditions away from equilibrium. When energy is continually supplied to system with interacting active particles, the outcome differs strikingly from the state of equilibrium. [26, 27] Nonequilibrium systems can be generally categorized as near equilibrium, in which a linear relation between force and flow exist, and far-from-equilibrium, in which there is a nonlinear relation between force and flow.[26, 27] A multitude of phenomena, from molecular processes on the nanoscale to dynamically changes in the climate on the planet, owe their existence to being

far-from-equilibrium. Processes that occur far-from-equilibrium are involved in intricate structure formation and dynamic behaviors, from snowflakes to highly organized structures of life.

1.1.5. Thermodynamics of Self-Organization in Far-From Equilibrium Systems

The Second Law of Thermodynamics involves two core and distinctive parameters between reversible and irreversible processes.[26, 27] A reversible process is defined as a process that can be reversed without leaving trace on the surroundings, meanwhile, an irreversible process is a process that cannot reverse itself and restore the system to its initial state.[26, 27] These two concepts ultimately lead to the introduction of entropy (S) and the formulation of the Second Law of Thermodynamics. In the 1850s, Clausius introduced the concept of entropy as a measure of the irreversibility of the thermodynamic system. In particular, the Clausius theorem (**Equation 1.1**) states

$$dS = \frac{dQ}{T} \qquad \textbf{Equation (1.1)}$$

where S is entropy, Q is heat and T is temperature. For example, between humans, when heat (dQ) is transferred from a body with temperature T_1 to a body with temperature T_2, the entropy raises by

$$dS = \frac{dQ}{T_1} - \frac{dQ}{T_2} \qquad \textbf{Equation (1.2)}$$

Therefore, from **Equation 1.2**, if heat is transferred from a hotter body to a cooler body ($T_1 > T_2$), the entropy grows greater than zero ($dS > 0$). This demonstrates the basis of the Second Law of Thermodynamics, for which entropy is constant for a reversible process whereas entropy grows for an irreversible process.

Boltzmann, in 1875, suggested another definition of entropy, in relation, to microstates using statistical mechanics as seen by **Equation (1.3)**

$$S = k_b \ln \Omega \qquad \textbf{Equation (1.3)}$$

where S is entropy, k_b is Boltzmann's constant (1.380×10^{-23} J K^{-1}), and Ω is the number of microstates consistent with a given macrostate. Microstates are referred to the number of "states", which are distinguishable at the atomic or molecular level. Overall, if a system tends to progress into a disordered macrostate, more random with greater microstates, the entropy increases, according to the theorem.

From the above-theorized definitions, entropy depends on the energy of the system. Therefore, irreversible processes not only have increased entropy but there is a change of energy within the system.[28] Entropy increases monotonically until it reaches the maximum value of thermodynamic equilibrium; in return, this is accompanied by reduction or dissipation of energy. Due to the aforementioned, the change in entropy can be distinguished as two parts, as shown in **Figure 1.3**.[29] First, a transfer of entropy, d_eS, across the boundaries caused by interaction with the environment. Second, entropy produced, d_iS, due to processes within the system (entropy production).

$$dS = d_eS + d_iS \qquad \textbf{Equation (1.4)}$$

The entropy production is assumed to always be $d_iS \geq 0$ and is the general definition of irreversibility.

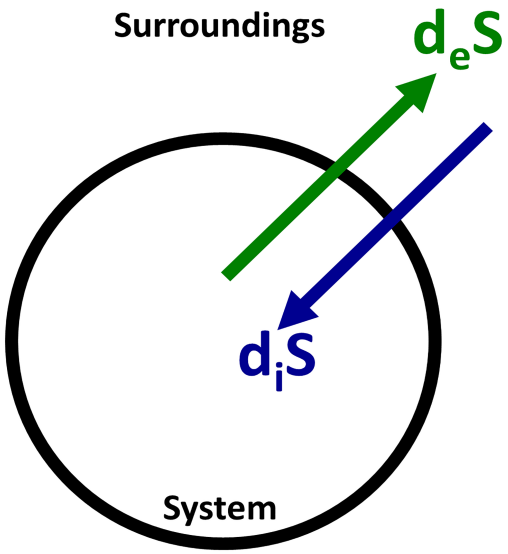

Figure 1.3: The exchange of entropy between the system and surrounding.

While increased entropy has generally been correlated to increased disorder, in many occurrences this is true; however, everyday life would be considered a violation of the Second Law. In particular, it is not always true that irreversible processes always destroy structure, become disordered and have increased entropy.[26, 30] Under certain nonequilibrium conditions, systems have been shown to spontaneously undergo transitions to an organized state, which, are generally states with low entropy.[26, 30] Spontaneous transition into an organized structure, or dissipative structure, were concepts introduced and termed self-organization by Ilya Prigogine. [31, 32]

Prigogine defined self-organization, in an open far-from-equilibrium system, means the system arose spontaneously and entirely via an irreversible process, more precisely, an external source was not imposed to initiate dissipative structure formation. Irreversible processes only contribute to entropy production.[31, 32, 33] He noted that the rate of entropy production per unit volume can be written as

$$\sigma\,(x,t) = \sum_k F_k J_k \geq 0 \qquad \textbf{Equation (1.5)}$$

where is σ rate of entropy production, F_k is thermodynamic forces, and J_k is thermodynamic flows. Furthermore, the total rate of entropy production in the entire system can be transcribed as

$$\frac{dS}{dt} = \int \sigma\,(x,t)dV \qquad \textbf{Equation (1.6)}$$

The expression for entropy production was examined and the entropy production has been demonstrated to be dependent on the state or condition of equilibrium.[31, 32, 33]

As aforementioned, there is a linear and nonlinear relationship in nonequilibrium thermodynamic systems. If a system is maintained slightly away from equilibrium, in the linear regime, the system cannot reach a state in which the entropy production is zero; however, it will minimize the entropy production.[33] This is called principle of minimum entropy production established by Prigogine.[32] Nevertheless, if a system is forced far away from equilibrium, to a regime where thermodynamic forces and flows are nonlinear, the rate of entropy production behaves extremely differently. More specifically, the transition to an organized dissipative state is characterized by an increased rate of entropy production, also called the maximum entropy production principle founded by Martyusheve and Seleznev.[34] The rate of entropy production value was created to provide a measure of complexity in thermodynamically organized systems.[33] When force and flow couple in complex ways to give rise to a highly self-organized structure, a higher rate of entropy production value will be computed.[33] Entropy production provides a fundamental understanding of higher order dynamics; however, it has also been shown to play an essential role in understand perception-action in biological intelligence.

1.1.6. End-Directed Evolution

Designed structures (or machines) are notably and fundamentally different from dissipative systems.[32] First, designed structures are based on reversible mechanics and do include

irreversible processes. In complete contrast, dissipative structures depend on dissipative or irreversible thermodynamic processes.[32] Secondly, designed machines are deliberately designed with a specific set of functions, which originate from processes external to the system, whereas, dissipative structures self-generate to a self-organized structure to carry out a function. Lastly, and most importantly different, dissipative structures have thermodynamic stability and can be restored if perturbed or "damaged", while this self-healing phenomena does not occurred with designed structures. These differences are given in **Table 1.1**.

Table 1.1: Contrasting the notions of designed structures and dissipative structures.

Designed Structures (Machines or Computers)	**Dissipative Structures (Nonequilibrium Systems & Organisms)**
• Based on the reversible laws of mechanics • Structure designed and assembled through process external to the system • Dissipative processes limit the efficiency of the system • Structure designed to perform a certain function • Generally not self-healing	• Based on the irreversible laws of mechanics • Structure arises spontaneously through entropy generating dissipative processes • Dissipative processes are essential to the system; without them the structure ceases to exist • Context dependent function arises because of structure • Self-healing

The remarkable ideology concerning a machine is, the machine can be disassembled, analyzed and understood completely and a new machine can be built give the proper technology; however, as noted by Robert Rosen, this idea is not so with organisms.[35] In addition to the aforementioned differences, organisms are complex and they have both structure and function resulting in self-organized behavior directed toward a particular end. Organisms seek items, interact with their environment, and respond to avoid adverse conditions, for which each responds in a way that permits them to reach the end goal. These are examples of end-directed evolution.[35] More specifically, the system may take different paths, but each reaches the same

final state.[35] Therefore, end-directed evolution is a potential property of far-from equilibrium dissipative structures although this has not been extensively investigated.

End-directed evolution has two distinctive aspects to consider the state to which it will evolve and the stability.[32] As previously mentioned, far-from-equilibrium systems will reach a state in which the rate of entropy production is maximized, which is exemplified in nature.[7, 33] In terms of stability, this means, if the system was perturbed, a dissipative system would restore back to the end state. These end-directed behaviors alongside collective behavior or active matter demonstrates the functional differentiation between a machine and a dissipative structure. Therefore, to fully comprehend the origin of behavior we see in organisms, end-directed dissipative self-organized systems need to be studied.

1.1.7. Electrically Driven Nonequilibrium System – Analogous to Chemical System

Features that will be discussed and observed herein this thesis mimic results acquired from an electronic self-organized end-directed system previously developed by Kondepudi et al.[36] While the construction is not the same, the overall thermodynamic behaviors achieved were analogous. In particular, the system is constructed with a high-voltage power supply whose output is sprayed across an air-oil interface of a petri dish that contains a ground electrode. Ions are sprayed from the power source onto the interface, which contains conductive elements (or beads) that can freely move around within the confines of the ground electrode, as illustrated in **Figure 1.4**.[36] During the experiment, multiple variables are recorded such as actual voltage (V), current through circuit (A), temperature within the dish (in K), and motion of the bead elements. These parameters alongside number, shape, composition, and homogeneity of the elements are key components to be known as they modulate the system's behavior.[36]

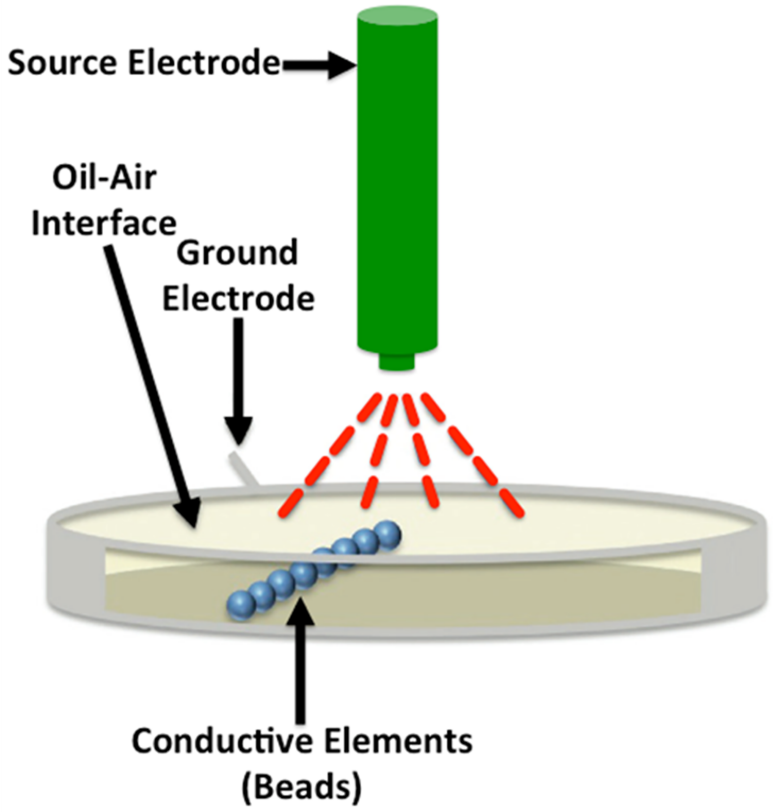

Figure 1.4: Schematic illustration of the basic experimental setup for the voltage-driven self-organized system Adapted and reprinted with permission from Reference 36.

In this electrically driven simple system, there were N numbers of spherical 4 mm chromium beads immersed in 60 mL of viscous oil within a 15 cm petri dish. The system was then subjected to a high voltage in the 15-30 kV range, located about 4 cm above the surface of the air-oil interface. The applied voltage induces an electric dipole moment on the beads and drives complex convection currents in the oil.[36] The dipole moment on the beads creates dipole-dipole interactions and drives their motion within the viscous oil and aggregates form.[36] Eventually, once above a current threshold voltage, one string of beads will make contact with the ground electrode, within minutes, and a discrete branching dissipative structure forms. At this

point, an organism-like dynamic filamentous structure is established and if voltage remains, the structure sways, as shown in the snapshot in **Figure 1.5**.[36]

Figure 1.5: Extracted example from video analysis of the organism-like dynamic filamentous dissipative structure that is formed during the electrically-driven system.

The most remarkable is a connection between dissipative structure formation and entropy production of the system is acquired.[36] In particular, while there are widely varying paths to tree formation and different tree structures, the system reaches the same final rate of entropy production.[36] The total rate of entropy production is expressed mathematically in terms of thermodynamic forces and flows,

$$\Sigma = \frac{d_i S}{dt} = \frac{V\ I\ (\boldsymbol{X}_i, \nu(\boldsymbol{r}))}{T} \qquad \textbf{Equation 1.7}$$

where V is the voltage, I (**X**i, ν(**r**)) is the current dependent on the position **X**i and velocity field ν(**r**) of the viscous fluid, and T is temperature. While the voltage is applied, the tree structure forms, this dissipative structure formation immediately is observed by a sharp jump in Σ, as shown by time series snapshots in **Figure 1.6**.[36] This jump in Σ is dependent on the number of

beads; however, between trials, regardless of variations in tree structure, Σ is virtually the same value. If the voltage is turned off, the tree will collapse, leading to a decreased Σ value. Consequently, it is the rate of entropy production that defines the end directedness.

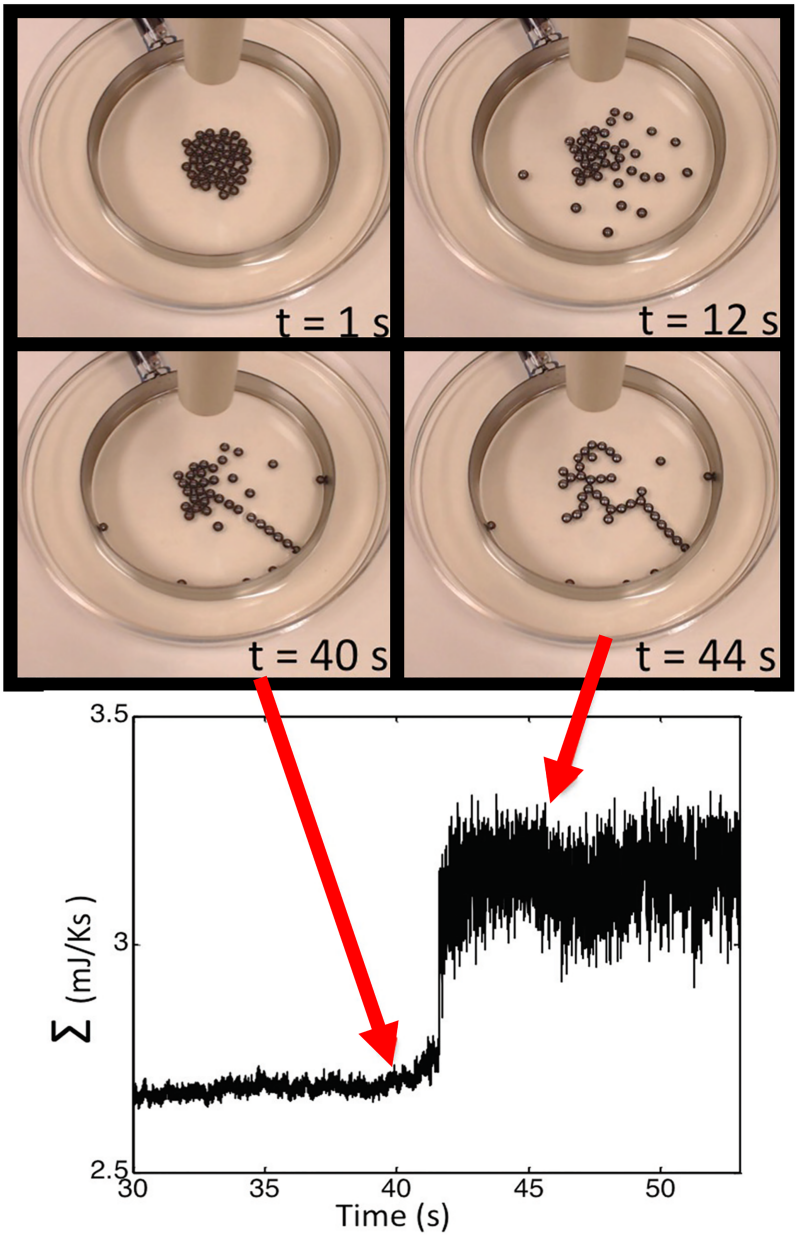

Figure 1.6: Evolution of the tree structure formation at four different time snapshots and the corresponding rate of entropy production output during the formation of the tree structure. Once

the dissipative tree structure forms and makes contact with the ground electrode, there is a distinctive sharp increase in Σ. Adapted and reprinted with permission from Reference 36.

This system has energy seeking behavior and was demonstrated by the fact that the stable tree structures were moving and indications seemed to provide the motion was toward increased currents and higher Σ.[36] Kondepudi et al confirmed the energy seeking behavior with two minor experiments. First, they gated a tree in a region of lower Σ, when the gate was opened, the tree moved freely and traveled to a location of higher Σ.[36] Secondly, the tree was allowed to move to the preferred location, but then it was forced to a different location by a tilt; however, the tree moved back to the higher Σ location it began in.[36] Overall, these basic experiments demonstrated energy-seeking behavior from a self-organized tree can be acquired and the thermodynamic emergent behavior could be investigated and calculated.

1.1.8. Self-motion in Chemical Systems

To chemically mimic the electronically driven end-directed behavior mentioned previously, a chemically driven nonequilibrium system needed to be developed. Self-motion in physical-chemical systems has been known for two decades.[37] In particular, to achieve independent self-motion for an active particle with in a given active matter system, each entity must generate its own motive force. Furthermore, each active natural particle must convert chemical energy into mechanical output; such self-driven unit is in essence a chemical locomotor.[5, 37] The driving locomotive force relies on either chemical or physical processes or both.

Synthetic nano- and micromotors that are powered by self-generated gradients have grown in interest. These motors move autonomously by numerous methods such as bubble

propulsions, diffusiophoresis, interfacial tension gradients, self-electrophoresis, and cyclic adsorption/desorption.[4, 5] Being able to move autonomously provides a system, in which, the foundations of collective behavior, such as swarming and flocking seen in biological systems, can be studied and further information can be elucidated from the inter-motor communications. Furthermore, if these autonomous systems can carry out independent functions such as sensing and reporting, even more thermodynamic information on biological systems could be potentially understood.

While there are several propulsion mechanisms, herein, we will discuss only the locomotion that is driven by the alteration in the interfacial tension gradients. Focus on this particular mechanism is due to the fact that meticulously designed and engineered particles were not necessary, and simplicity was desired herein. Consequently, a famous example, also involving the physical dissolution, is the motion of camphor molecules at the water interface.[38, 39, 40, 41] In particular, dissolution and spreading of the camphor on the water interface causes interfacial instability. This dissolution process, results in a decreased interfacial tension around the camphor molecule. Fluctuations in the system, cause interfacial tension gradients to vary around the camphor molecules and as a result continuous motions are generated. Furthermore, dissolution creates shape change of the particle, which creates increasingly complex motion.[38, 41] Therefore, shape change in conjunction with multiple camphor molecules lead to a collective self-organized structure, which is currently employed in multiple analyses to study fundamental thermodynamic properties as well as perception-action phenomena.[42, 43, 44, 45]

Benzoquinone (BQ) and derivatives locomotion is also driven by changes in the interfacial tension gradient and physical dissolution of the compound.[46, 47] Simple, single particle studies were previously reported and will be briefly described.[46, 48, 49] However, benzoquinone is

implemented herein due to the simplest of the system and lack of required engineering even though there are alternative propulsion mechanisms, these require carefully engineered particles. In our case, remarkable behavior is observed spontaneously under minimal conditions like observed in biological systems. In particular, a small disk of benzoquinone at the air-water interface exhibited continuous, intermittent and velocity-decay motion.[46, 48, 49] Locomotion of the single disk was driven by changes in interfacial tension at the interface.[46, 48, 49] BQ disk movement at the air-water interface produced a heterogeneous concentration gradient within the surrounding medium.[46, 48, 49] Generating heterogeneous interfacial tension gradients around the particle forced disk motion that was also influenced by chemical reactions, or light. [46, 48, 49]

Multiple benzoquinone particle systems were not studied; therefore, we investigate multiple particles and yearn to develop perception-action if dissipative structures are formed. Thus, part one of this thesis focuses on the collective behavior of particles in self-motion. With multiple benzoquinone disks, there is possibility that the collective surface tension fields will interact and give rise to collective behavior and emergent thermodynamic properties. This theory is validated due to the aforementioned evidence of such behavior in the camphor system. Overall, the surface tension system will share several key features as observed by the electrically-driven system, and additionally the Gibbs energy or entropy production is supplied by the particles themselves to create cooperative self-organization.

1.2 Part Two: Introduction for Assessment of CD62L as a Protein Biomarker for Metastatic Bladder Cancer

1.2.1. Background and Significance

A combat on cancer was propelled by the United States Congress and then declared by President Nixon in 1971.[50] The solitary purpose was to provide distinctive awareness on the devastation the disease produces; furthermore, it was presented as a treacherous enemy and serious threat to the human race.[50, 51, 52] Since the declaration, cancer was revealed to manifest in hundreds of types and subtypes, affecting all organ and tissues.[52, 53] The manifestation of cancer types transpires due to cancer cell complexity and their origination from mutations and rearrangements of the human genome.[52, 53, 54, 55] Extensive cancer growth occurred due to significant transformations within the cell, specifically genetic and epigenetic reprogramming of regulatory circuits corrupting normal cells; therefore, promoting proliferation of cancer cells.[52, 53, 54, 55] Although significant progress has been achieved in comprehending the nature of cancer, this subject remains a highlighted focus in research.[54, 55]

The "war on cancer" evidently continues to be fought, as cancer remains the leading cause of death in the United States and throughout the world.[56] The National Center for Health Statistics predicted, in 2016, there would be ~1.7 million patients diagnosed with cancer, and ~600,000 deaths among Americans, which corresponds to 1,645 deaths per day.[56] Cancer has surpassed heart disease as the number one cause of death in the United States and even other countries in the world. It is unmistakable that if cancer diagnosis is prolonged, the survival rate drastically diminishes for patients with advanced cancers (3 – 27%) versus localized controlled cancers (50 – 90%).[56] Therefore, statistical data alone demonstrates diagnosis at an early stage, before metastasis, plays a crucial role on cancer survival.

In this thesis, we focus on the detection of bladder cancer. Bladder cancer distresses the cells that line the inner portion of the bladder; depending on how the cells look, a class/type of bladder cancer is determined.[57] Detection and diagnosis of bladder caner is extremely essential as this solid tumor is the fourth most common in men and eighth in women. Furthermore, according to the American Cancer Society, ~74,000 newly diagnosed cases (about 75% in men and 25% in women) and ~16,000 deaths are estimated to occur in 2016.[57] The disease has a five times higher prevalence among men than women, and the median diagnosis age is 65 years. Stage of diagnosis is pertinent and a critical determinant in patient therapy outcome. Currently, the five-year survival rates are dependent upon whether the cancer is localized in the inner layer, advanced regional, or deeper within the layers of the bladder (distant), these rates are 88%, 35% and 6%, respectively (**Figure 1.7**).[58, 59] In addition, the foremost problem with bladder cancer is, more than 70% of patients will have recurrence within 2 years of treatment; therefore, extensive long-term surveillance and repeated interventions are required to ensure avoidance of lethal invasive bladder cancer.[60] Overall, bladder cancer is a flawless example of why early diagnosis and disease progression monitoring is crucial for cancer survival.

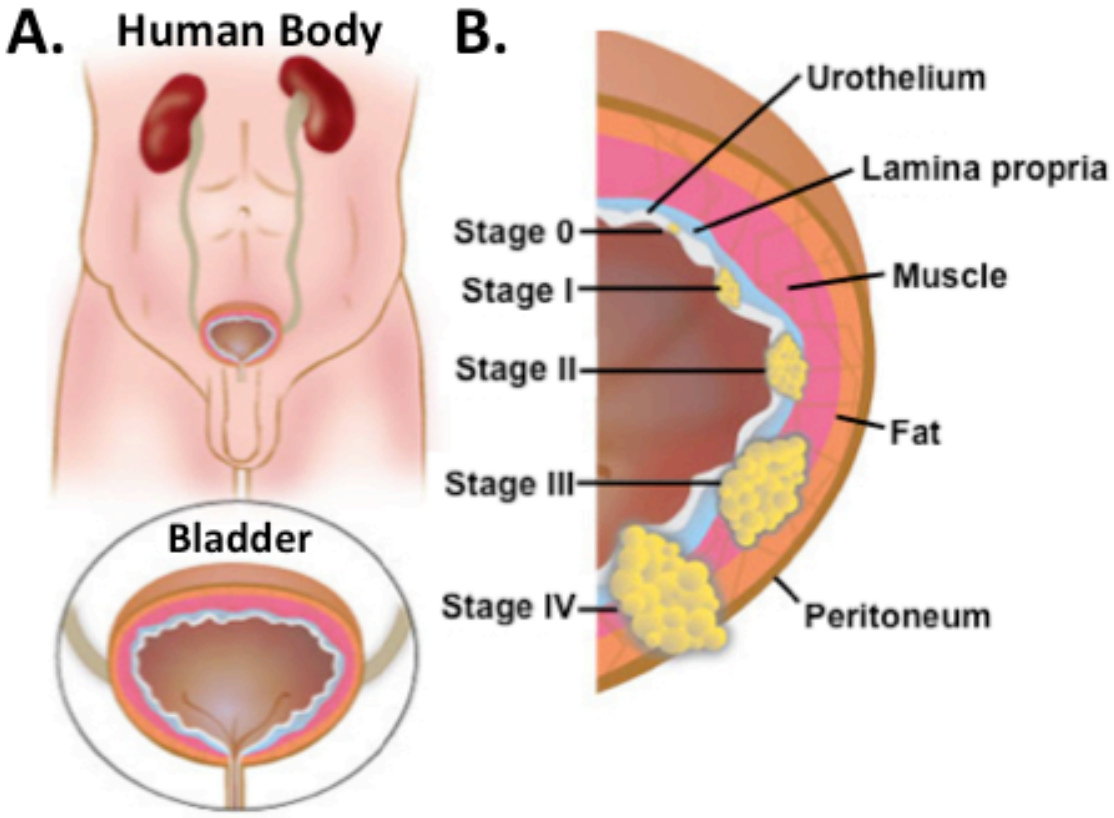

Figure 1.7: Illustration of the bladder demonstrating depth of cancer invasion into bladder wall for the five different stages of bladder cancer.

During development of cancer many secreted proteins become over-expressed in the blood at very early stages, even prior to the onset of physical symptoms. The level of secreted proteins can either indicate the presence or absence of the disease; furthermore, in certain cases, like we propose herein, these levels could potentially indicate the stage of cancer as well as provide continued guidance on therapy. Therefore, the goal of part two in this dissertation was the pursuit of a rapid, reproducible, and cost effective diagnostic device for ultrasensitive measurement of serum protein CD62L for bladder cancer, using different aspects of nanotechnology and labeling techniques in conjugation with electrochemical detection. The

ideology was to first validate the experimental setup with both standard CD62L protein samples and spiked CD62L samples, followed by detection of human serum from patients with various bladder cancer stages. The clinical data acquired will be compared to the gold-standard detection methodology, with the expectation that our low cost single diagnostic system holds excellent promise over standard methodologies for diagnosis, prognosis, and continued surveillance for bladder cancer.

1.2.2. Current Cancer Detection Methodologies

Present cancer detection strategies are typically founded on imaging technology, such as, computed tomography (CT), magnetic resonance imaging (MRI), and positron emission tomography (PET), which each employ contrast chemicals (also called dyes) that discriminate between distinctive anatomical features.[61, 62, 63, 64] Though each imaging technique is advantageous, quantification of cancer is not provided, additionally, information is limited on the aggressiveness of the disease. Moreover, these expensive diagnostic imaging tools are unavailable in resource limited areas.[61, 62, 63, 64] In addition, invasive biopsies can be acquired and cancerous cells within tissue samples can be examined based on cell morphology using microscopy.[65, 66] Diagnosis dependent upon biopsies has the potential to provide inconclusive information, as oversight in early onset of the disease can occur.[65, 66] Increasingly popular methodologies involves a non-invasive cancer screening route, which is completed by assaying bodily fluids to assess cancer protein biomarker levels.[67, 68, 69] However, the number biomarkers utilized is substantially low due to inefficient biomarker discovery and development. Therefore, a long and arduous journey still remains for the ideal cancer detection methodology.

Initial clinical diagnosis of bladder cancer is achieved by the gold standard cystoscopic examination coupled with voided urine cytology (VUC).[60] Cytological studies examines cellular material existing in the urine visually, which is extremely invasive, uncomfortable procedure for the patient and may require biopsies on suspicious lesions. In addition, this particular technique can become costly, as anesthesia is typically required.[60] Meanwhile, VUC relies on microscopic analysis of cancer cells that were shed into the voided urine.[60] While non-invasive, diagnosis is only detected with high-grade and high-stage tumors, as low-grade tumors shed fewer cancer cells into the urine; thus sensitivity is problematic.[60] After initial treatment, patients are involved in continued surveillance with examinations every 3 months for 2 years, and then every 6 months for 2 years. Consequently, the development of non-invasive assays would provide a tremendous advantage in diagnosis and continued disease monitoring.

1.2.3. Cancer Biomarkers

The National Institute of Health (NIH) slates a biomarker as "molecules that can be measured and evaluated as indicators of normal or disease processes and response to therapeutic treatments."[70, 71, 72] According to this description, biomarkers include biomolecule such as nucleic acids, proteins, and small molecules in secreted fluid and physical or chemical alternations to these biological parameters indicate disease state. Therefore, biomarkers can be utilized or implemented for targeted therapies, prediction of risk, forecaster of response to treatment, monitor disease progression, but most importantly, aid in early disease screening methodologies.[70, 71, 72]

A tumor marker is a biomolecule produced by a tumor or by host receptor in response to development of cancer cells. [70, 71, 72, 73] These markers can be quantitatively measured as an

indicator of a cancerous process. More specifically, tumor markers are categorized into a multitude of types including proteins, glycoproteins, antigens, receptors, genetic markers, and ribonucleic acid (RNA) molecules. Like most biomarkers, tumor biomarkers, are designed to comprehend the pathobiology of the disease.[74, 75] In the case of cancer, once normal cells have progressed to cancer cells they become tumorigenic and eventually malignant.[74, 75] It is evident that the genetic alterations and rearrangements lie at the protein level.[76, 77] Overall, by definition, protein tumor biomarker candidates are a promising strategy to be implemented for the early diagnosis of cancers and ultimately would serve as markers for disease state. Therefore, extensive effort has been dedicated to developing protein biomarkers and panels of protein biomarkers for early diagnostics and disease monitoring. [74, 75, 76, 77]

Accessibility to proteins in bodily fluids is a major advantage for biomarker development. Bladder cancer, studied herein, has this convenience, due to urine. More specifically, urine can be obtained in copious amounts, in a non-invasive manner, for repeat sample analysis. A number of commercial molecular tests have been FDA-approved for precise circumstances and will be described in the latter section.[60, 78] While soluble bladder tumor proteins have been studied and implemented for diagnosis, extensive effort still remains. Specifically, tumor biomarkers are not clinically employed for the determination of all conditions such as, progression, prognosis or treatment. Furthermore, there are no set forecasters of metastatic potential, which is required to overcome the substantial issues surrounding the survival rate in metastatic bladder cancer cases. [79, 80, 81] Therefore, it is crucial that a sensitive diagnostic tool is developed to predict and further monitor different stages of bladder cancer.

1.2.4. Point-of-Care Detection Systems

To preserve the quality of life for cancer patients, in-house measurement of protein biomarker levels in cell tissues or extracts and biological fluid is a long-standing goal to still be achieved. [82] Analysis of cancer specimens by protein biomarker detection is currently only fulfilled by clinical laboratories using large, automated methodologies, which exception to devices mentioned in detail in this section.[82, 83, 84] Clinical diagnostics requires sample transport and skilled technicians, thereby increasing diagnosis timeline as well as costs. Therefore, development of a point-of-care (POC) devices will provide rapid and reliable quantitative results no matter the location. [82, 83, 84] To transition to POC devices, current clinical testing systems need to drastically reduce in size, specifically to a handheld device. Furthermore, maintain the capability of multiple analyte analysis, sustain high-throughput, as well as be a specific and sensitive assay.

Various assay systems exist for measurement of protein biomarkers; however, for nearly 40 years, enzyme-linked immunosorbent assays (ELISA) have served as the mainstay for protein detection.[85] Presently, ELISA is the most widely implemented clinical protein test, and deemed the gold standard for single-protein detection in disease states. The ELISA assay system employs a sandwich immunoassay protocol as illustrated in **Figure 1.8**.[75, 82, 85, 86] In particular, a capture antibody (Ab_1) is attached to the bottom of individual 96-wells within a plate, and Ab_1 is specific for a target antigen (Ag) protein. Once the antigen and capture antibody bind, an enzyme-labeled secondary antibody (Ab_2) selective interacts and attaches to complete the sandwich. The labeled detection antibody provides the ability of both detection and amplification of signal. Once the sandwich is complete, substrate chemical is added to the system and the interaction causes the enzyme label to be converted, thus a change in solution color transpires and a chromogenic

reporter can read this visible signal. This color change provides a quantitative estimate of the cancer disease state. While commercially available ELISA kits have low detection limits and highly specific antibodies for targeted approaches, this is an extensive process with large volumes of sample required and expensive non-portable instrumentation.[75, 82, 85, 86] Therefore, advancement of more portable, high throughput but timely POCs is still crucial for in-home cancer diagnostics and surveillance.

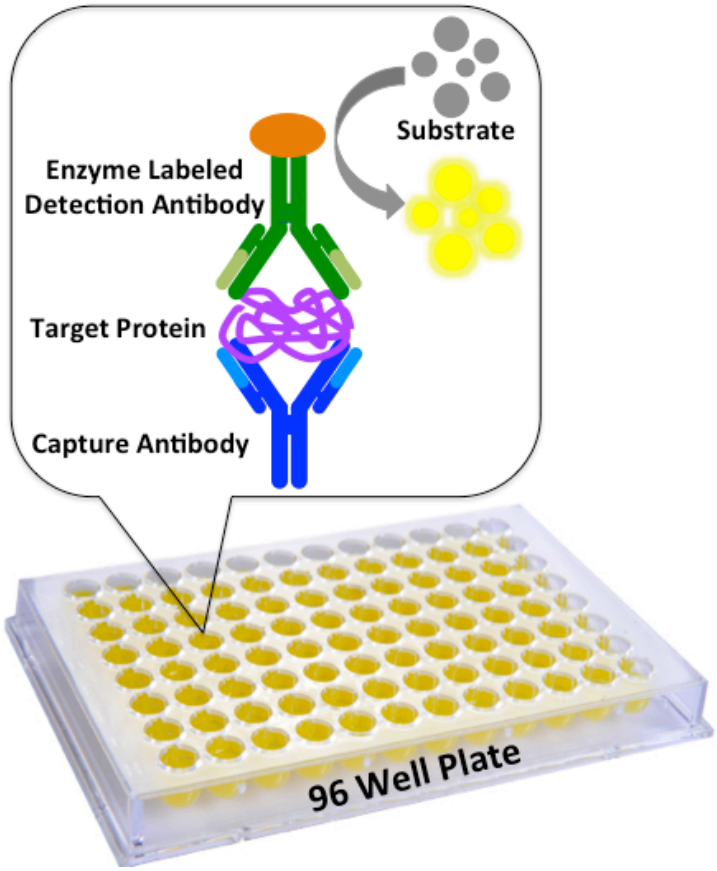

Figure 1.8: The gold standard ELISA based assays with individual wells coated with the capture primary antibody, which is specific and selective to the target protein. A conjugate solution with labeled detection antibody incubates on the surface and selectively binds; therefore, when substrate is added a color change occurs and is proportional to target protein concentrations.

As aforementioned, there are numerous bladder cancer POC devices on the market, which are FDA approved as shown in **Table 1.2**.[60] These test include the measurement of soluble proteins such as bladder tumor associated antigen (BTA), nuclear matrix protein 22 (NMP22), and proteins detected on fixed urothelial cells (ImmunoCyt).[60, 87] The BTA stat test employs an immunoassay protocol with two different monoclonal antibodies specific for the presence of BTA antigen in urine. A line will form, like in a pregnancy test, and indicate the antigen-conjugate complex formed, thus bladder cancer is suspected in the urine specimen. While this test has diagnostic POC capabilities; the sensitivities range from 29 to 91% and specificities range from 56 to 86%.[88] These percent ranges demonstrate that false information can be imparted by other non-cancerous conditions and further progression in the test should be implemented. BladderChek test is an immunochromographic quantitative ELISA test that screens urinary NMP22 protein, which is a nuclear mitotic protein responsible for distribution of chromatin to daughter cells.[89, 90] Cohort studies have been completed and demonstrated promising results but sensitivity and specificity are 49% and 87% respectively.[91] The results can be impacted as NMP22 marker has been found to also be elevated in other various disease states.[89, 92] These two above-mentioned POC devices alone demonstrate inaccuracies in sensitivity and specificity; however, these test systems are low-cost, portable and overall informative of the disease state.[60, 87] Therefore, a protein biomarker with better specificity and selectivity of metastatic potential should be discovered and then combined with the aforementioned markers to provide a multiplexed molecular assay that will ensure diagnosis and disease monitoring can be achieved.

Table 1.2: Urinary bladder cancer assays that are FDA-approved.

Assay	Protein Marker	FDA Approval Purpose	Assay Style
BTA stat	BTA[1]	Diagnosis, monitoring	Colorimetric
BTA TRAK	BTA	Diagnosis, monitoring	Sandwich Assay
NMP22	NUMA 1[2]	Diagnosis, monitoring	Colorimetric
ImmunoCyt	CEA and MUCIN antigens	Monitoring	Sandwich Assay
UroVysion	Chromosomes 3,7,17*	Diagnosis, monitoring	FISH[3]

[1]Bladder tumor associated antigen (BTA)
[2]Nuclear mitotic apparatus protein 1 (NUMA)
[3]Fluorescence in situ hybridization
*Detection of aneuploidy for these chromosomes

1.2.5. Electrochemical-Based Protein Detection

Current POC devices for bladder cancer detection have accuracy rates that reach near the sensitivities of the gold standard cystoscopy and cytology; however, further progression is essential for diagnosis, progression, surveillance and metastatic staging. Thus, an ultrasensitive methodology should be implemented to enhance both specificity and sensitivity in the established FDA approved techniques. Therefore, current research has evolved based upon the enormous captivator of the biosensor POC market (over 85%) that enables in-home medical diagnosis, the glucose meter.[83] In particular, it employs an electrochemical based detection process and this strategy offers robust and quantitative measurements with simple, low-cost, sensitive instrumentation.[75, 82] Overall, the established glucose meter demonstrates that an electrochemical-based protein biomarker immunoassay system would provide a portable device for in-home usage and can be tailored for multiple disease states.

The ideology of an electrochemical-based protein detection mechanism is catching wave in the biotechnology and diagnosis industry. Protein analyte levels in electrochemical biosensors are detected by changes in either potential, current, conductance or impedance due to explicit biorecognition reactions.[84, 93, 94] Numerous electrochemical biosensor techniques can be and have

been implemented, but amperometric sensors, applying a constant potential and monitoring change in current, offer high sensitivity, which brands them as candidates for clinical POC protein detection devices.[84, 93, 94]

Electrochemical protein detection platforms based on the gold standard ELISA procedural process has been pioneered; specifically, rather than implementing a color-changing enzyme-label, the enzyme-label are involved in the generation an electroactive product that can be detected electrochemically, as demonstrated in **Figure 1.9**.[95, 96, 97] Since time has progressed, self-contained single analyte enzyme electrochemical immunosensors have been developed.[98, 99] In particular, these immunosensors feature an electrode surface bound capture antibody, which in the presence of a target, the protein will be captured and then an enzyme-labeled detection antibody will complete the sandwich assay on the same surface. Enzyme-labels that have been employed are horseradish peroxidase (HRP), alkaline phosphatase, gluocose oxidase, conductive polymers, electroactive metal ion complexes and liposomes loaded with electroactive species.[100, 101, 102]

Among the aforementioned, HRP is the most widely utilized label for both standard ELISA and electrochemical immunosensors and will be implemented in our studies and play a paramount role.[75,103] HRP is a member of the ferroprotoporphyrin group of peroxidase and contains a central heme group that is capable of catalytic oxidation/reduction in the presence of hydrogen peroxide.[103] The catalytic oxidation-reduction cycle for HRP is shown in **Figure 1.9**. More specifically, once the heme center is activated by hydrogen peroxide, it converts to the oxidized form (Fe^{IV}=O), which can be reduced on the electrode surfaces at low potentials.[103] If multiple electroactive species are implemented or bound on the sensor surface signal amplification will transpire due to generation of multiple electroactive species, which provides

an advantage affecting the sensitivity. Therefore, sandwich immunoassay electrochemical platforms will provide selectivity such as ELISA, but provide additional sensitivity for protein biomarker detection compared to current POCs implemented for bladder cancer. This ideology is an objective for a portion of this thesis.

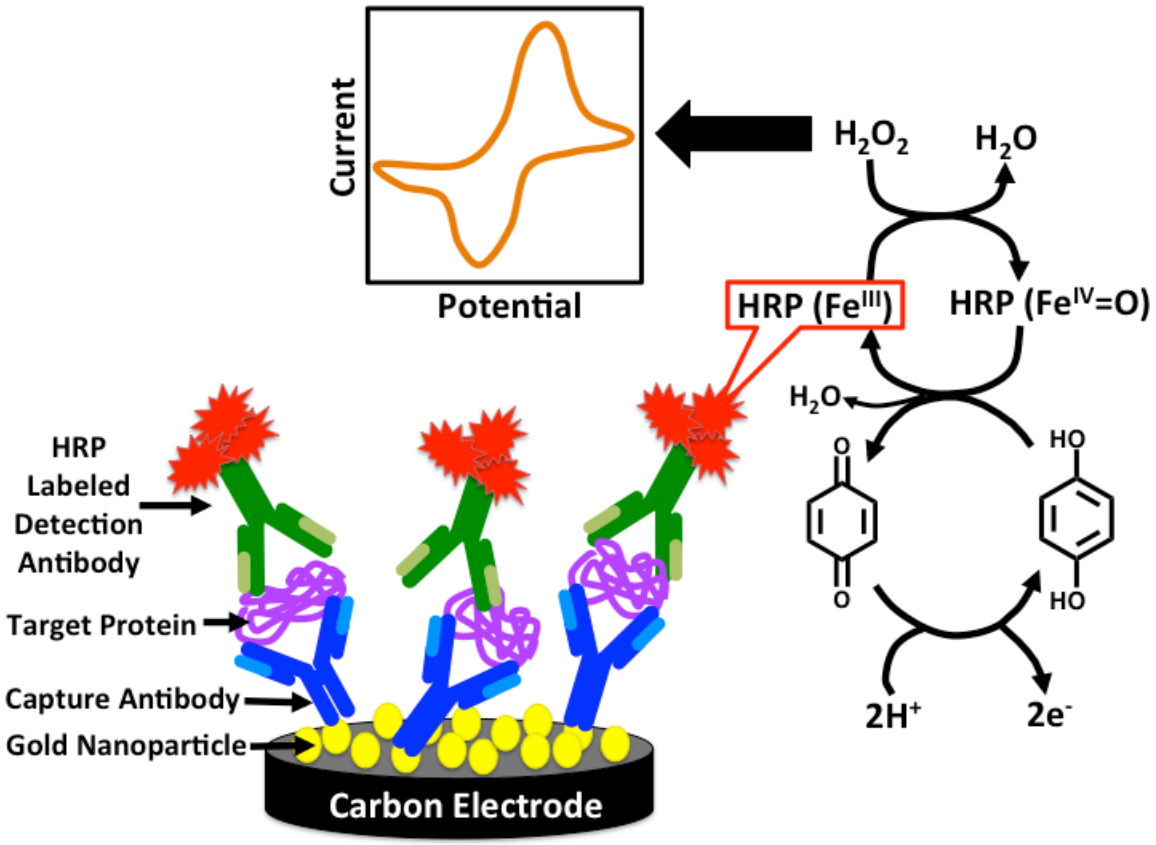

Figure 1.9: A single carbon electrode with a sandwiched immunoassay coated on the surface. Secondary detection antibody is labeled with an electroactive enzyme, where a cyclic voltammogram is acquired upon generation of electrons at the electrode surface via a catalytic reduction-oxidation cycle with horseradish peroxidase (HRP).

1.2.6. Microfluidic Electrochemical Immunoassay Detection

Microfluidic electrochemical immunoarray sensors are comprised of many remarkable characteristics for POC detection such as minimal sample volumes, high sensitivity, low-cost materials, and user friendly with a degree of automation.[104, 105] Moreover, implementation of microfluidics enables integration of microanalytical functions such as, mixers, reagent reservoirs, and detection chambers, to enhance the portability and future capability to act as an in-home handheld diagnostic tool.[104, 105] Heinemann group pioneered the electrochemical immunosensing, nevertheless were the first to integrate microfluidics with electrochemical detection.[106] Specifically, they employed a magnetic bead based system with glass microfluidic device and achieved detection limits at the low ng mL^{-1} range.[106] Heinemann et al inspired multiple groups to fabricate devices capable of microfluidic electrochemical immunoassay detection and research continues to implement this ideology to achieve an ideal diagnostic POC device for diverse disease states.[107]

Our research group has been involved in the development and progression of the microfluidic electrochemical immunoassay device division of research. The first generation system (**Schematic 1.1**), incorporates a low-cost in-house microfluidic system fabricated using a machine molded poly(dimethylsiloxane) (PDMS) channel (~60 μL) that was sandwiched between two poly(dimethylmethacrylate) (PMMA) plates, known as the detection chamber.[108] This detection chamber houses our 8-electrode sensor array, additionally, the top PMMA plate is equipped with a silver/silver chloride (Ag/AgCl) reference electrode and platinum (Pt) counter electrode, which is then connected by PEEK tubing to a syringe pump and sample injector.[108] In this case, protein analytes were captured offline onto magnetic beads carrying enzyme labels and then injected into the microfluidic detection system.[108] Employing this microfluidic detection

chamber alongside offline capture of protein analytes Chikkaveeraiah et al were able to achieve detection limits in sub pg mL range in 1 hr for both interleukin-6 (IL-6) and prostate specific antigen (PSA).[108] This technique was further extended to multiplexed detection of four protein biomarkers for clinical diagnosis of oral cancer.[109]

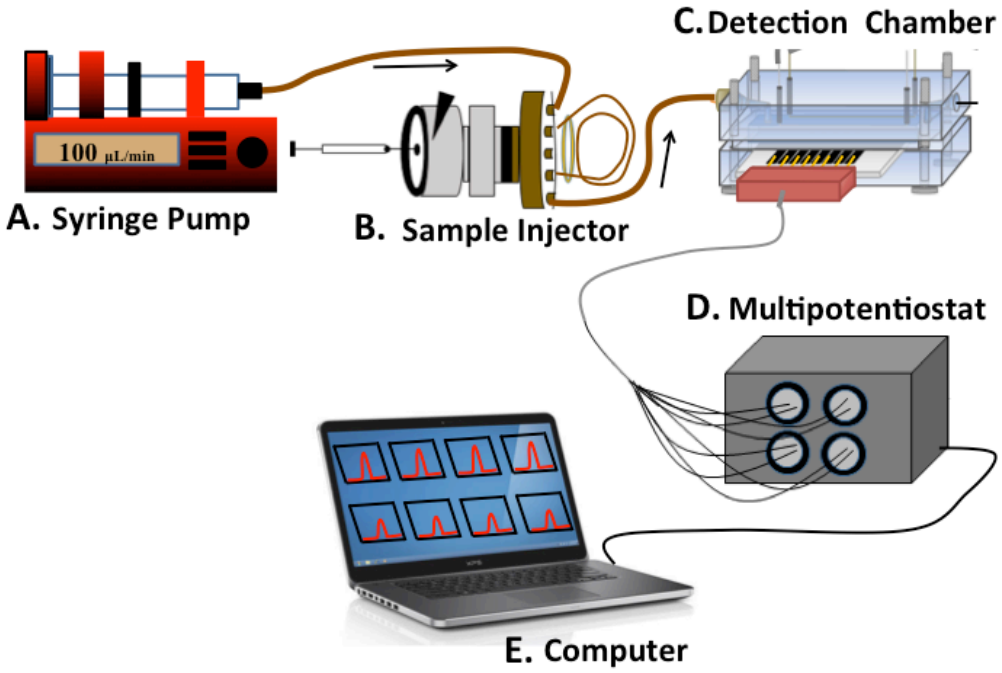

Scheme 1.1: The first generation offline capture microfluidic electrochemical immunoassay system with A) syringe pump that flows solutions through B) sample injector that allows protein conjugates to be injected and incubated in C) detection chamber that houses 8-electrode modified array that is then connected to D) multipotentiostat to apply a set potential with time for which a readout of current will be acquired by E) computer.

The current ever evolving microfluidic electrochemical immunoarray involves a degree of automation as the microfluidic design has expanded to include a ~100 µL capture chamber upstream from the detection chamber (**Schematic 1.2**).[110] This new generation design permits a

majority of the immunoassays to be completed within the microfluidic system, in particular, reagents, samples and wash solutions are loaded by the operator but flow transports them to designated destinations.[110] More specifically, in this setup, a capture chamber is constructed with two flat PMMA plates and a flexible PDMS channel, when assembled forms an oval channel featuring an area for a magnetic stir bar.[110] The capture chamber is upstream and connected by PEEK tubing and switching valves to the detection chamber housing our 8-electrode modified immunosensor.[110] Thus, a syringe pump drives the flow of buffer or reagents to two switching valves via a sample injector. These switching valves direct the directionality of the flow to either the reaction chamber, reaction to detection chamber, or detection chamber only.[110] Once the reagents have flowed to the designated areas and the sandwiched assay is completed, detection at the immunoarray surface via electrochemical detection by a multipotentiostat transpires. The electrochemical signal as previously described is directly related to protein analyte concentration.

The common feature between both system generations was the implementation of magnetic beads. Magnetic beads are widely used due to their purification and separation capability of proteins in complex biological media.[107, 111] In addition, magnet beads can easily be loaded with capture agents, such as antibodies or proteins and further purified with the assistance of an inexpensive magnet.[107, 111] These are superparamagnetic in nature, which means in the absence of a magnet there is no magnetic effect, and there is not retainment after repeated exposure to a magnetic field.[107, 111] In this work, magnetic beads are employed to capture protein from serum samples and serve as a signal-amplifying agent. These magnetic beads will be coupled with both HRP enzyme label molecules and secondary detection antibodies to capture marker proteins. Therefore, we employ the aforementioned semi-automated microfluidic

immunoarray system, but modifications to the magnetic beads will be completed to enhance our desired functionality in our detection strategy.

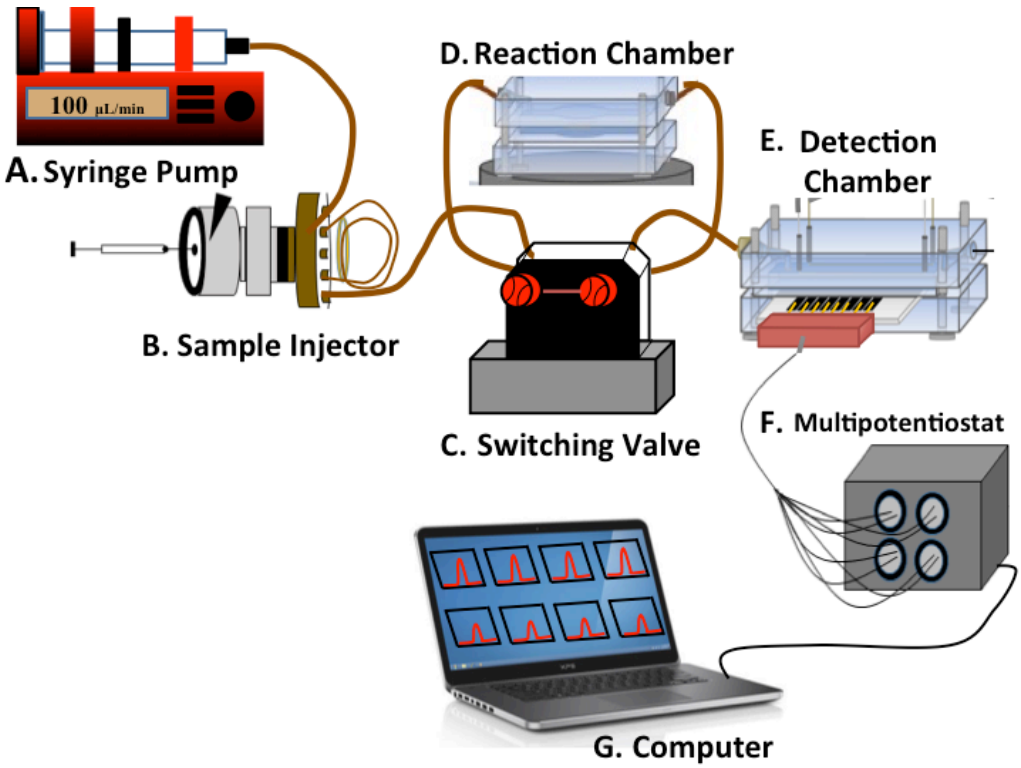

Scheme 1.2: Schematic representation of the second generation electrochemical microfluidic immunoassay system. Online capture and detection system features A) syringe pump to push solution through B) the sample injector C) and switching valves allowing the direction of flow to be altered to either D) reaction chamber which captures proteins on magnetic bioconjugates or E) detection camber where the 8-electrode is housed for completion of sandwiched assay that will be detected by F) the multipotentiostat and an electrochemical response will be recorded by G) computer.

1.3 Overview of Dissertation

The goal of this thesis was to develop a dissipative structure in a chemical setting to mimic living systems as well as assess the capability of protein CD62L to accurately provide diagnostic predictions for metastatic bladder cancer. To achieve these two separate aforementioned goals, the first objective was to construct a co-operative dissipative chemical system and then demonstrate the collective had the capability of perception-action. Then secondly, adapt an existing electrochemical immunoarray methodology to sensitively evaluate CD62L as a non-invasive biomarker for predicting risk of metastatic bladder cancer. Both set goals were achieved and are explained in detail herein.

Chapter 1 focuses on the contextual and significance of the work completed. The chapter delivers a detailed description and account of the information needed to properly comprehend the basic approaches implemented for both self-motion of particles at the air-water interface and assessment of CD62L as a potential protein biomarker. More specifically, highlighted importance and concrete foundations are set to accurately rationalize the work demonstrated herein.

Chapter 2 concentrates on characterizing self-organization emerging spontaneously between collections of solid macroscopic BQ disks at the air-water interface without intervention of chemical reactions. A non-engineered system exhibited spontaneous, continuous locomotion between multiple BQ particles as observed by dramatic co-operative effects including paired travel and extended cycling of dissolving disks. More interestingly, more extensive flocking-like group motion for collections of irregularly shaped particles was shown. The chapter concluded by explaining this novel flocking-like grouping within the framework of non-equilibrium thermodynamics under a driving force development of localized surface free energy fields.

Chapter 3 addresses thermodynamic emergent properties for a self-organizing physical-chemical system that gives rise to collective proto-sensor behavior. More specifically, the co-operative flocking system established in Chapter 2 was further implemented for the development of a physical self-serving system. The BQ flock-like group demonstrated the capability of being a self-serving proto-sensor system; which was responsive to secondary fields and proficient in perceiving new sources of energy. More precisely, non-sensor and sensor elements were embedded that were both responsive to the heterogeneous interfacial tension fields (primary field), but only one is responsive to a secondary field. Consequently, this work demonstrated the first reported chemical self-organized proto-sensor in which a secondary field affected the behavior of the non-sensor element and thus the overall co-operative flock. These fundamental self-motion studies provide the foundation to understanding emergent thermodynamic properties of inanimate systems in comparison to animate systems.

Chapter 4 explains the integration and adaptation of an established semi-automated microfluidic electrochemical immunoarray system for low sample volume detection of L-selectin within 30 min for bladder cancer. The electrochemical immunoarray system was employed over conventional protein assays to provide an ultrasensitive, rapid detection protocol for distinguishing metastatic potential in bladder cancer patients. In particular, a semi-automated in-house system was implemented and modifications to the established protocol were completed to provide sensitive detection of CD62L and maintain a low patient sample dilution factor. The results obtained indicate our nanostructured immunosensor was capable of detecting CD62L with high accuracy for the predictive ability of metastatic bladder cancer in comparison to the gold standard ELISA.

1.4 References

1. Leake, M. C. The physics of life: one molecule at a time. *Philosophical Transactions of the Royal Society B: Biological Sciences***2013***, 368*, 20120248.
2. Lipowsky, R.; Klumpp, S. 'Life is motion': multiscale motility of molecular motors. *Physica A: Statistical Mechanics and its Applications* **2005***, 352*, 53-112.
3. Bray,D.; *Cell Movements: From Molecules to Motility*, 2nd ed.; Garland Publishing: New York, 2001.
4. Wang, W.; Duan, W.; Ahmed, S.; Mallouk, T. E.; Sen, A. Small power: Autonomous nano- and micromotors propelled by self-generated gradients. *Nano Today* **2013***, 8*, 531-554.
5. Paxton, W. F.; Sundararajan, S.; Mallouk, T. E.; Sen, A. Chemical Locomotion. *Angewandte Chemie International Edition* **2006***, 45*, 5420-5429.
6. Hong, Y.; Velegol, D.; Chaturvedi, N.; Sen, A. Biomimetic behavior of synthetic particles: from microscopic randomness to macroscopic control. *Phys. Chem. Chem. Phys.* **2010***, 12*, 1423-1435.
7. Nicolis, G.; Prigogine, I.; *Self-Organization in Non-Equilibrium Systems.* Wiley, 1977.
8. Finer, J. T.; Simmons, R. M.; Spudich, J. A. Single myosin molecule mechanics: piconewton forces and nanometre steps. *Nature* **1994***, 368*, 113-119
9. Burgess, S. A.; Walker, M. L.; Sakakibara, H.; Knight, P. J.; Oiwa, K. Dynein structure and power stroke. *Nature***2003***, 421*, 715-718.
10. Shima, T.; Kon, T.; Imamula, K.; Ohkura, R.; Sutoh, K. Two modes of microtubule sliding driven by cytoplasmic dynein. *Proceedings of the National Academy of Sciences* **2006***, 103*, 17736-17740.
11. Marchetti, M. C.; Joanny, J. F.; Ramaswamy, S.; Liverpool, T. B.; Prost, J.; Rao, M.; Simha, R. A. Hydrodynamics of soft active matter. *Rev. Mod. Phys.* **2013***, 85*, 1143-1189.
12. Ramaswamy, S. The Mechanics and Statistics of Active Matter. *Annu. Rev. Condens. Matter Phys.* **2010***, 1*, 323-345.
13. Schweitzer, Frank. *Brownian Agents and Active Particles : Collective Dynamics in the Natural and Social Sciences*. Springer Series in Synergetics. Berlin ; New York: Springer, 2003
14. Sanchez, T.; Chen, D. T. N.; DeCamp, S. J.; Heymann, M.; Dogic, Z. Spontaneous motion in hierarchically assembled active matter. *Nature* **2012***, 491*, 431-434.
15. Vicsek, T.; Zafeiris, A. Collective motion. *Physics Reports* **2012***, 517*, 71-140.
16. Takatori, S. C.; Brady, J. F. Swim stress, motion, and deformation of active matter: effect of an external field. *Soft Matter* **2014***, 10*, 9433-9445.
17. Doubrovinski, K.; Kruse, K. Self-Organization of Treadmilling Filaments. *Phys. Rev. Lett.* **2007***, 99*, 228104.
18. Mitchison, T. J.; Cramer, L. P. Actin-Based Cell Motility and Cell Locomotion. *Cell* **1996***, 84*, 371-379.
19. Verkhovsky, A. B.; Svitkina, T. M.; Borisy, G. G. Self-polarization and directional motility of cytoplasm. *Current Biology* **1999***, 9*, 11-S1.
20. Budrene, E. O.; Berg, H. C. Complex patterns formed by motile cells of Escherichia coli. *Nature* **1991***, 349*, 630-633.
21. Lushi, E.; Wioland, H.; Goldstein, R. E. Fluid flows created by swimming bacteria drive self-organization in confined suspensions. *Proc. Natl. Acad. Sci. U. S. A.* **2014***, 111*, 9733-9738.

22. Matsumoto, K.; Takagi, S.; Nakagaki, T. Locomotive mechanism of Physarum plasmodia based on spatiotemporal analysis of protoplasmic streaming. *Biophys. J.* **2008***, 94*, 2492-2504.
23. Sumpter, D. J. T. *Collective Animal Behavior;* Princeton University Press: Princeton, N.J., 2010.
24. Giardina, I. Collective behavior in animal groups: theoretical models and empirical studies. *HFSP Journal* **2008***, 2*, 205-219.
25. Mossman, Kenneth L. *The Complexity Paradox : The More Answers We Find, the More Questions We Have*. 2014.
26. Kondepudi, D. *Introduction to Modern Thermodynamics*; Wiley: New York, 2008.
27. Groot, S. R. De, and P. Mazur. *Non-equilibrium Thermodynamics*. Amsterdam, New York: North-Holland Pub.; Interscience Publishers, 1962.
28. Prigogine, I.; Rysselberghe, P. V. Introduction to Thermodynamics of Irreversible Processes. *J. Electrochem. Soc.* **1963***, 110*, 97C
29. Kleidon, A., Lorenz, R.D. *Non-equilibrium Thermodynamics and the Production of Entropy: Life, Earth, and beyond*. Understanding Complex Systems. Berlin; London: Springer, 2005.
30. Prigogine, I., Stengers, and Pagels. "Order out of Chaos." *Physics Today* 38, no. 1 (1985): 97-99.
31. Nicolis, G.; Prigogine, I. *Self-organization in nonequilibrium systems: From dissipative structures to order through fluctuations*. New York: Wiley,1977.
32. Kondepudi, D., Prigogine, I. *Modern Thermodynamics, From Heat Engine to Dissipative Structures*, 2nd ed; John Wiley: New York, 2015.
33. Kondepudi, D. Self-Organization, Entropy Production, and Physical Intelligence. *Ecological Psychology* **2012***, 24*, 33-45.
34. Martyushev, L. M.; Seleznev, V. D. Maximum entropy production principle in physics, chemistry and biology. *Physics Reports* **2006***, 426*, 1-45.
35. Rosen, Robert. *Essays on Life Itself*. Complexity in Ecological Systems Series. New York: Columbia University Press, 2000.
36. Kondepudi, D.; Kay, B.; Dixon, J. End-directed evolution and the emergence of energy-seeking behavior in a complex system. *Phys Rev E.* **2015***, 91*, 050902.
37. Mikhailov, A.; Meinkohn, D. In *Self-motion in physico-chemical systems far from thermal equilibrium;* Stochastic Dynamics; Springer Berlin Heidelberg: Berlin, Heidelberg, 1997; pp 334-345.
38. Nakata, S.; Iguchi, Y.; Ose, S.; Kuboyama, M.; Ishii, T.; Yoshikawa, K. Self-Rotation of a Camphor Scraping on Water: New Insight into the Old Problem. *Langmuir* **1997***, 13*, 4454-4458.
39. de Gennes, P. G. The dynamics of reactive wetting on solid surfaces. *Physica A (Amsterdam)* **1998***, 249*, 196-205.
40. [1]. Sekimoto, K. Langevin equation and thermodynamics. *Prog. Theor. Phys. Suppl.* **1998***, 130*, 17-27.
41. Nakata, S.; Hayashima, Y. Spontaneous dancing of a camphor scraping. *J. Chem. Soc., Faraday Trans.* **1998***, 94*, 3655-3658.
42. Kohira, M. I.; Hayashima, Y.; Nagayama, M.; Nakata, S. Synchronized self-motion of two camphor boats. *Langmuir* **2001***, 17*, 7124-7129.

43. Suematsu, N. J.; Ikura, Y.; Nagayama, M.; Kitahata, H.; Kawagishi, N.; Murakami, M.; Nakata, S. Mode-Switching of the Self-Motion of a Camphor Boat Depending on the Diffusion Distance of Camphor Molecules. *J. Phys. Chem. C* **2010***, 114*, 9876-9882.
44. Soh, S.; Bishop, K. J. M.; Grzybowski, B. A. Dynamic Self-Assembly in Ensembles of Camphor Boats. *J Phys Chem B* **2008***, 112*, 10848-10853.
45. Soh, S.; Branicki, M.; Grzybowski, B. A. Swarming in Shallow Waters. *J. Phys. Chem. Lett.* **2011***, 2*, 770-774.
46. Suematsu, N. J.; Miyahara, Y.; Matsuda, Y.; Nakata, S. Self-Motion of a Benzoquinone Disk Coupled with a Redox Reaction. *J. Phys. Chem. C* **2010***, 114*, 13340-13343
47. Nakata, S.; Arima, Y. Self-motion of a phenanthroline disk on divalent metal ion aqueous solutions coupled with complex formation. *Colloids Surf., A* **2008***, 324*, 222-227.
48. Matsuda, Y.; Suematsu, N. J.; Nakata, S. Photo-sensitive self-motion of a BQ disk. *Phys. Chem. Chem. Phys.* **2012***, 14*, 5988-5991.
49. Nakata, S.; Matsuda, Y.; Ikura, Y. S.; Takeda, A.; Izumi, S. Mode Change in the Self-Motion of a Benzoquinone Disk Coupled with a NADPH System. *Chem. Phys. Chem.* **2012***, 13*, 520-524.
50. Tisevich, D. A. Legislative history of the National Cancer Institute and the National Cancer Program. *Cancer* **1996***, 78*, 2620-2621.
51. Haines, I. The war on cancer: time for a new terminology. *The Lancet,* **2014** *383*, 1883.
52. Hanahan, D. Rethinking the war on cancer. *The Lancet* **2014***, 383*, 558-563.
53. Chin, L.; Andersen, J. N.; Futreal, P. A. Cancer genomics: from discovery science to personalized medicine. *Nat. Med.* **2011***, 17*, 297-303.
54. Hanahan, D.; Weinberg, R. A. The Hallmarks of Cancer. *Cell.,***2000,** *100*, 57-70.
55. Hanahan, D.; Weinberg, R. Hallmarks of Cancer: The Next Generation. *Cell* **2011***, 144*, 646-674.
56. Siegel, R. L.; Miller, K. D.; Jemal, A. Cancer statistics, 2016. *CA: A Cancer Journal for Clinicians* **2016***, 66*, 7-30.
57. American Cancer Society. Cancer facts and figures. Atlanta: American Cancer Society; 2015.
58. Herr HW, Donat SM. Outcome of Patients with Grossly Node Positive Bladder Cancer After Pelvic Lymph Node Dissection and Radical Cystectomy *J. UROL.* **2001***, 165*, 62-64.
59. Ries LAG, Krapcho M, Stinchcomb DG, Howlader N, Horner MJ, Mariotto A, et al. editors. *SEER Cancer Statistics Review,* 1975– 2005. National Cancer Institute. Bethesda, MD, Available at: http:// seer.cancer.gov/csr/1975_2005/ 2008; based on November 2007 SEER data submission, posted to the SEER web site.
60. Goodison, S.; Rosser, C. J.; Urquidi, V. Bladder Cancer Detection and Monitoring: Assessment of Urine- and Blood-Based Marker Tests. *Molecular Diagnosis & Therapy* **2013***, 17*, 71-84.
61. Weissleder, R. Molecular Imaging in Cancer. *Science* **2006***, 312*, 1168-1171.
62. Hussain, T.; Nguyen, Q. T. Molecular imaging for cancer diagnosis and surgery. *Adv. Drug Deliv. Rev.* **2014***, 66*, 90-100.
63. Choyke, P.; Kurdziel, K. A.; Mena, E.; Lindenberg, M. L. Meeting the challenges of PET-based molecular imaging in cancer. *Expert Review of Molecular Diagnostics* **2013***, 13*, 671-680.
64. Gatenby, R. A.; Grove, O.; Gillies, R. J. Quantitative Imaging in Cancer Evolution and Ecology. *Radiology* **2013***, 269*, 8-14.

65. Faus, C.; Roda, D.; Frasson, M.; RosellÃ³, S.; GarcÃa-Granero, E.; Flor-Lorente, B.; Navarro, S. The role of the pathologist in rectal cancer diagnosis and staging and surgical quality assessment. *Clinical and Translational Oncology* **2010***, 12*, 339-345.
66. Kumar, R.; Srivastava, R.; Srivastava, S. Detection and Classification of Cancer from Microscopic Biopsy Images Using Clinically Significant and Biologically Interpretable Features. *Journal of Medical Engineering***2015***, 2015*, 14.
67. Hanash, S. M.; Pitteri, S. J.; Faca, V. M. Mining the plasma proteome for cancer biomarkers. *Nature* **2008***, 452*, 571-579.
68. Kulasingam, V.; Diamandis, E. P. Strategies for discovering novel cancer biomarkers through utilization of emerging technologies. *Nat Clin Prac Oncol* **2008***, 5*, 588-599.
69. Pavlou, M. P.; Diamandis, E. P.; Blasutig, I. M. The Long Journey of Cancer Biomarkers from the Bench to the Clinic. *Clin. Chem.* **2013***, 59*, 147.
70. Strimbu, K.; Tavel, J. A. What are Biomarkers? *Current opinion in HIV and AIDS* **2010***, 5*, 463-466.
71. Atkinson, A. J.; Colburn, W. A.; DeGruttola, V. G.; Biomarkers Definitions Working Group Biomarkers and surrogate endpoints: Preferred definitions and conceptual framework. *Clinical Pharmacology & Therapeutics* **2001***, 69*, 89-95.
72. Karley, D.; Gupta, D.; Tiwari, A. Biomarker for Cancer: A great Promise for Future. *World J. Oncol*., **2011**, *2*, 151-157.
73. Vaidyanathan, K.; Vasudevan, D. M. Organ Specific Tumor Markers: What's New? *Indian Journal of Clinical Biochemistry* **2011***, 27*, 110-120.
74. Ebert, M. P. A.; Korc, M.; Malfertheiner, P.; Rocken, C. Advances, Challenges, and Limitations in Serum-Proteome-Based Cancer Diagnosis. *J. Proteome Res.* **2006***, 5*, 19-25.
75. Rusling, J. F.; Kumar, C. V.; Gutkind, J. S.; Patel, V. Measurement of biomarker proteins for point-of-care early detection and monitoring of cancer. *Analyst* **2010***, 135*, 2496-2511.
76. Rai, A. J.; Chan, D. W. Cancer Proteomics: Serum Diagnostics for Tumor Marker Discovery. *Ann. N. Y. Acad. Sci.* **2004***, 1022*, 286-294.
77. Sadikovic, B.; Al-Romaih, K.; Squire, J. A.; Zielenska, M. Cause and Consequences of Genetic and Epigenetic Alterations in Human Cancer. *Curr. Genomics* **2008***, 9*, 394-408.
78. Shariat, S. F.; Karam, J. A.; Lotan, Y.; Karakiewizc, P. I. Critical Evaluation of Urinary Markers for Bladder Cancer Detection and Monitoring. *Reviews in Urology* **2008***, 10*, 120-135.
79. Watts, K. L.; Ristau, B. T.; Yamase, H. T.; Taylor III, J. A. Prognostic implications of lymph node involvement in bladder cancer: are we understaging using current methods?*BJU Int.* **2011***, 108*, 484-492.
80. Shariat, S. F.; Karakiewicz, P. I.; Palapattu, G. S.; Lotan, Y.; Rogers, C. G.; Amiel, G. E.; Vazina, A.; Gupta, A.; Bastian, P. J.; Sagalowsky, A. I.; Schoenberg, M. P.; Lerner, S. P. Outcomes of Radical Cystectomy for Transitional Cell Carcinoma of the Bladder: A Contemporary Series From the Bladder Cancer Research Consortium. *J. Urol.* **2006***, 176*, 2414-2422.
81. Stein, J. P.; Lieskovsky, G.; Cote, R.; Groshen, S.; Feng, A.; Boyd, S.; Skinner, E.; Bochner, B.; Thangathurai, D.; Mikhail, M.; Raghavan, D.; Skinner, D. G. Radical Cystectomy in the Treatment of Invasive Bladder Cancer: Long-Term Results in 1,054 Patients. *Journal of Clinical Oncology* **2001***, 19*, 666-675.
82. Kingsmore, S. F. Multiplexed protein measurement: technologies and applications of protein and antibody arrays. *Nature reviews.Drug discovery* **2006***, 5*, 310-320.

83. Gubala, V.; Harris, L. F.; Ricco, A. J.; Tan, M. X.; Williams, D. E. Point of Care Diagnostics: Status and Future. *Anal. Chem.* **2012***, 84*, 487-515.
84. Soper, S. A.; Brown, K.; Ellington, A.; Frazier, B.; Garcia-Manero, G.; Gau, V.; Gutman, S. I.; Hayes, D. F.; Korte, B.; Landers, J. L.; Larson, D.; Ligler, F.; Majumdar, A.; Mascini, M.; Nolte, D.; Rosenzweig, Z.; Wang, J.; Wilson, D. Point-of-care biosensor systems for cancer diagnostics/prognostics. *Biosensors and Bioelectronics* **2006***, 21*, 1932-1942.
85. Voller, A.; Bartlett, A.; Bidwell, D. E. Enzyme immunoassays with special reference to ELISA techniques. *Journal of Clinical Pathology* **1978***, 31*, 507-520.
86. Crowther, J.R. *The ELISA Guidebook*, 2nd ed.; SciTech Book News, 2009.
87. Xylinas, E.; Kluth, L. A.; Rieken, M.; Karakiewicz, P. I.; Lotan, Y.; Shariat, S. F. Urine markers for detection and surveillance of bladder cancer. *Urologic Oncology: Seminars and Original Investigations* **2014***, 32*, 222-229.
88. Thomas, L.; Leyh, H.; Marberger, M.; Bombardieri, E.; Bassi, P.; Pagano, F.; Pansadoro, V.; Sternberg, C. N.; Boccon-Gibod, L.; Ravery, V.; Le Guludec, D.; Meulemans, A.; Conort, P.; Ishak, L. Multicenter Trial of the Quantitative BTA TRAK Assay in the Detection of Bladder Cancer. *Clin. Chem.* **1999***, 45*, 472.
89. Ponsky, L. E.; Sharma, S.; Pandrangi, L.; Kedia, S.; Nelson, D.; Agarwal, A.; Zippe, C. D. Screening And Monitoring For Bladder Cancer: Refining The Use Of Nmp22. *J. Urol.* **2001***, 166*, 75-78.
90. Chang, Y.; Wu, C.; Lee, Y.; Huang, P.; Kao, Y.; Shiau, M. Evaluation of nuclear matrix protein-22 as a clinical diagnostic marker for bladder cancer. *Urology* **2004***, 64*, 687-692.
91. Grossman H, Soloway M, Messing E,et al SUrveillance for recurrent bladder cancer using a point-of-care proteomic assay. *JAMA* **2006***, 295*, 299-305.
92. Sharma, S.; Zippe, C. D.; Pandrangi, L.; Nelson, D.; Agarwal, A. Exclusion Criteria Enhance The Specificity And Positive Predictive Value Of Nmp22* And Bta Stat [Dagger]. *J. Urol.* **1999***, 162*, 53-57.
93. Wang, J. Electrochemical biosensors: Towards point-of-care cancer diagnostics. *Biosensors and Bioelectronics* **2006***, 21*, 1887-1892
94. Grieshaber, D.; MacKenzie, R.; Voros, J.; Reimhult, E. Electrochemical Biosensors - Sensor Principles and Architectures. *Sensors (Basel, Switzerland)* **2008***, 8*, 1400-1458.
95. Heineman, W. R.; Halsall, H. B. Strategies for Electrochemical Immunoassay. *Anal. Chem.* **1985***, 57*, 1321A-1331A.
96. Ronkainen-Matsuno, N.J., Thomas, J.H., Halsall, H.B., Heineman, W.R.; Electrochemical immunoassay moving into the fast lane. *TrAC, Trends Anal. Chem.* **2002,** *21*, 213-225.
97. Ronkainen, N. J.; Halsall, H. B.; Heineman, W. R. Electrochemical biosensors. *Chem. Soc. Rev.* **2010***, 39*, 1747-1763.
98. Warsinke, A.; Benkert, A.; Scheller, F.W. Electrochemical Immunoassays, Fresenius. J. Anal. Chem. **2000**, *366*, 622-634.
99. Yakovleva, J.; Emnéus, J. In *Electrochemical Immunoassays;* Bioelectrochemistry; John Wiley & Sons, Ltd: 2008; 2008; pp 377-410.
100. Wang, J. Electrochemical Glucose Biosensors. *Chem. Rev.* **2008***, 108*, 814-825.
101. Wang, J. Nanoparticle-Based Electrochemical Bioassays of Proteins. *Electroanalysis* **2007***, 19*, 769-776.
102. Bartlett, P. N.; Toh, C. S.; Calvo, E. J.; Flexer, V. In *Modelling Biosensor Responses;* Bioelectrochemistry; John Wiley & Sons, Ltd: 2008; 2008; pp 267-325.

103. Veitch, N. C. Horseradish peroxidase: a modern view of a classic enzyme. *Phytochemistry* **2004***, 65*, 249-259.
104. Bange, A.; Halsall, H. B.; Heineman, W. R. Microfluidic immunosensor systems. *Biosensors and Bioelectronics* **2005***, 20*, 2488-2503.
105. Henares, T. G.; Mizutani, F.; Hisamoto, H. Current development in microfluidic immunosensing chip. *Anal. Chim. Acta* **2008***, 611*, 17-30.
106. Choi, J.; Oh, K. W.; Thomas, J. H.; Heineman, W. R.; Halsall, H. B.; Nevin, J. H.; Helmicki, A. J.; Henderson, H. T.; Ahn, C. H. An integrated microfluidic biochemical detection system for protein analysis with magnetic bead-based sampling capabilities. *Lab Chip* **2002***, 2*, 27-30.
107. Lim, C. T.; Zhang, Y. Bead-based microfluidic immunoassays: The next generation. *Biosensors and Bioelectronics* **2007***, 22*, 1197-1204.
108. Chikkaveeraiah, B. V.; Mani, V.; Patel, V.; Gutkind, J. S.; Rusling, J. F. Microfluidic Electrochemical Immunoarray for Ultrasensitive Detection of Two Cancer Biomarker Proteins in Serum. *Biosens. Bioelectron.* **2011***, 26*, 4477-4483.
109. Malhotra, R.; Patel, V.; Chikkaveeraiah, B. V.; Munge, B. S.; Cheong, S. C.; Zain, R. B.; Abraham, M. T.; Dey, D. K.; Gutkind, J. S.; Rusling, J. F. Ultrasensitive Detection of Cancer Biomarkers in the Clinic by Use of a Nanostructured Microfluidic Array. *Anal. Chem.* **2012***, 84*, 6249-6255.
110. Otieno, B. A.; Krause, C. E.; Latus, A.; Chikkaveeraiah, B. V.; Faria, R. C.; Rusling, J. F. On-line Protein Capture on Magnetic Beads for Ultrasensitive Microfluidic Immunoassays of Cancer Biomarkers. *Biosens. Bioelectron.* **2013***, 53*, 10.1016/j.bios.2013.09.054.
111. Otieno, B. A.; Krause, C. E.; Rusling, J. F. Chapter Seven - Bioconjugation of Antibodies and Enzyme Labels onto Magnetic Beads. *Meth. Enzymol.* **2016***, 571*, 135-150.

Chapter Two:

Co-operative Self-Motion of Multiple Benzoquinone Disks at the Air-Water Interface

2.1 Abstract

Self-motion of physical-chemical systems is a promising avenue for studying and developing mechanical functions with inanimate systems. In this paper, we investigate spontaneous motion of collections of solid macroscopic benzoquinone (BQ) disks at the air-water interface without intervention of chemical reactions. The BQ particles slowly dissolve and create heterogeneous interfacial tension fields on the water surface that drive the motion. Spontaneous, continuous locomotion was observed between multiple BQ particles, along with coupling, collisions, cycling and collective foraging for interfacial free energy. Analysis of the motion suggests co-operative behavior depends strongly on particle shape.

2.2 Introduction

Motion is a fundamental property of living and non-living systems. Molecular diffusion in response to chemical potential gradients represents a simple thermodynamically controlled example, in which free energy differences translate to molecular movement.[1-5] Biomotors and organisms can dissipate chemical energy into mechanical energy, enabling mechanical activity of the organism.[2,5-8] Human locomotion results from the ability of muscle cells to hydrolyze adenosine triphosphate (ATP) to adenosine diphosphate (ADP).[9,10] Enzymes, such as myosin, a linear motor, work along an actin filament substrate within the muscle, to provide the power and assistance needed to liberate the phosphate group.[10] ATP hydrolysis instantaneously releases

energy for mechanical work by which motions needed to sustain human life occur.[9,11] A related example is flagella motors of bacteria that change direction and velocity by sensing the local environment.[12,13] Forces such as, proton flux, pH gradients, and sodium ion potentials drive these organelles depending on the type of bacterial flagella motor.[12,13] Swarming bacterial motors form collective phases of colonies and the co-directional cluster motion is induced by chemiosmotic potential.[14] Another multicellular colony of differentiated cells is represented by slime mold *Physarum polycephalum*, a unicellular, multinucleate organism that assembles and moves due to forces generated by oscillatory contractions within the cell matrix.[15,16] The protoplasmic motive flux constructs a complex, functional material that is proficient in foraging, decision-making and problem solving.[15-18]

Movement in both living and non-living systems are often related to complex phenomenon and understanding their driving forces are important for biomedical advances as well as for designing dynamic systems for future applications of many types. For example, autonomous motors can potentially recognize complex tasks as in biological systems.[5,6] Studies of self-motion of macro- to nanoscale objects are important simplified models for understanding and mimicking both living and inanimate systems. A wide range of inanimate motion mechanisms controlled by chemical or physical processes have been investigated experimentally and theoretically.[6,19-26] In these systems, differences in surface free energy on the itinerant object and surrounding media can produce self-motion by taking advantage of free energy gradients.[1-3] A well-studied example involves camphor disks or boats at the air-water interface that move due to asymmetrical dissolution and sublimation of camphor molecules.[21,22,27-29] These events create an interfacial tension gradient around the particle decreased due to the surface activity of camphor. The interfacial tension fields at the solid-liquid interfaces are the main driving motive

force that induces motion.[30] Shape also contributes to the directional trajectories.[27,31] Camphor fragments have demonstrated translational and orbital motion, attributed to the original shape and gradual change throughout dissolution.[27,31] Further investigations into the nature of camphor's self-motion demonstrated mode-switching, synchronized motion and collective motion capabilities.[27,29,30,32]

Single 1,4-benzoquinone (BQ) and 1,10-phenanthroline (phen) particles were recently investigated as potential, novel autonomous motor systems.[24-26,33,34] A small disk of BQ at the air-water interface exhibited continuous, intermittent and velocity-decay motion. Mode-switching was influenced and modulated due to factors such as redox reactions, UV light and biochemical reactions.[24-26] In each case, locomotion of the single disk was driven by changes in interfacial tension at the interface. BQ disk movement at the air-water interface produced a heterogeneous concentration gradient within the surrounding medium. [24-26] Generating heterogeneous interfacial tension gradients around the particle forced disk motion that was influenced by chemical reactions, or light.[24-26] Multiple particle systems were not studied.

Herein, we report co-operative motion of multiple BQ disks at the air-water interface that slowly dissolve to lower interfacial tension and create surface free energy fields that direct co-operative particle motion. Collective behavior driven by interacting interfacial tension fields has been reported using carefully engineered camphor systems.[32,37-39] Here, we demonstrate and characterize self-organization emerging spontaneously under ambient conditions with multiple, non-engineered BQ particles. To that end, we sought to establish the minimal conditions under which self-organization emerged. Videos of multiple particle motion at the air-water interface demonstrate co-operative motion without intervention of chemical reactions or light, suggesting that locally heterogeneous interfacial tension fields generate disk locomotion. Dramatic co-

operative effects include paired travel, extended cycling of dissolving disks and group motion of more irregularly shaped particles. Co-operative behaviors can be explained within the framework of non-equilibrium thermodynamics under a driving force development of localized surface free energy fields.

2.3 Experimental

2.3.1 Chemicals and Materials

1, 4-Benzoquinone (BQ), sodium chloride (NaCl), and Tween-20 were from Sigma Aldrich. Nanopure water (18 MΩ·cm) was obtained from house-distilled water purified by a Hydro Service and Supplies Picosystem (model no. ET-11218).

2.3.2 Methods

2.3.2.1 Benzoquinone Disk Preparation

BQ powder was finely ground in a mortar and then molded into a pellet (3 mm diameter, 1 mm thick) using a die set and hand press (PIKE Technology, model no. 161-1100). Each disk weighed 4.2±0.2 mg. Aqueous 0.10 M NaCl was poured into a glass petri dish (90 mm diameter, 25 mL volume) then a pellet/s of BQ were added to the air-water interface. Irregularly shaped and sized BQ particles were prepared by breaking 3 mm BQ disks into pieces. These irregular fragments were then lightly dusted with lycopodium powder, which is highly hydrophobic, to extend observation time of self-motion.

2.3.2.2 Concentration Evaluation Protocol

UV/Vis spectroscopy (HP/Agilent 8453) was utilized to measure dissolved BQ. Solution was acquired from the same position within the petri dish and absorbance was monitored at

various elapsed times throughout BQ particle locomotion. Absorbance was measured over a 20 min period, in which, BQ disks were dissolved, had been dissolved or sank. Concentrations of BQ were estimated using standard calibration curves.

2.3.2.3 Monitoring Process of Benzoquinone Self-Motion

Motion of the BQ particles was monitored with a digital camera (JVC-HD GZ-E200BU, maximum frame rate: 30 fps). Observation were made until the disks dissolved normally over 15-20 min. Video analysis was completed on a personal computer using image-analysis software "ImageJ 1.41" (National Institute of Health, USA), in addition to, "iDTracker" (Cajal Institute de Polavieja lab, Madrid). Reproducibility was examined over 10 replicate experiments.

2.4 Results

Multiple BQ disks were carefully dropped onto the aqueous phase and immediate locomotion of each disk transpired at the air-water interface. The primary data were illustrated by supplementary videos cited at specific points in the text below; however, ESI video files were not submitted with dissertation. Continuous and intermittent motions were the two main characteristic types of self-motion observed in each series featuring 1, 2, 4, 6, 8 or 10 BQ disks in a single petri dish. Continuous motion dominated. These various resultant motions were seen until the disks sank or dissolved, which typically took at least 15-20 min.

2.4.1 Continuous Motion of Benzoquinone Disks

Continuous motion and symmetrical disk shapes were upheld differently for 1 and 2 disk/s versus 4, 6, 8, and 10 BQ disks. For disk series 1 and 2, symmetric circular disk shape was maintained for ~ 8 to 10 min, while for disk series 4, 6, 8 and 10 circular symmetrical shapes

were only sustained for ~ 4 to 6 min. While the symmetry of the disk is upheld, both circular orbital and linear translational motions were observed. Circular orbital motion of BQ disks transpired throughout the complete self-motion of the particles, as shown by extracted [x,y] trajectories in **Figure 2.1**. However, the [x,y] diameter of circular motion is affected by the symmetry or asymmetry of the particles shape. As observed in **Figure 2.1**, symmetrical disks typically have a greater circular diameter in comparison to asymmetrical disk described below. In addition to the circular motion, rotation around the particles centroid was observed to occur at times. Circular rotational motion observed was dominantly clockwise; however, the direction of rotation would suddenly reverse in the counterclockwise direction. These circular motions were seen in both circular and square petri dishes.

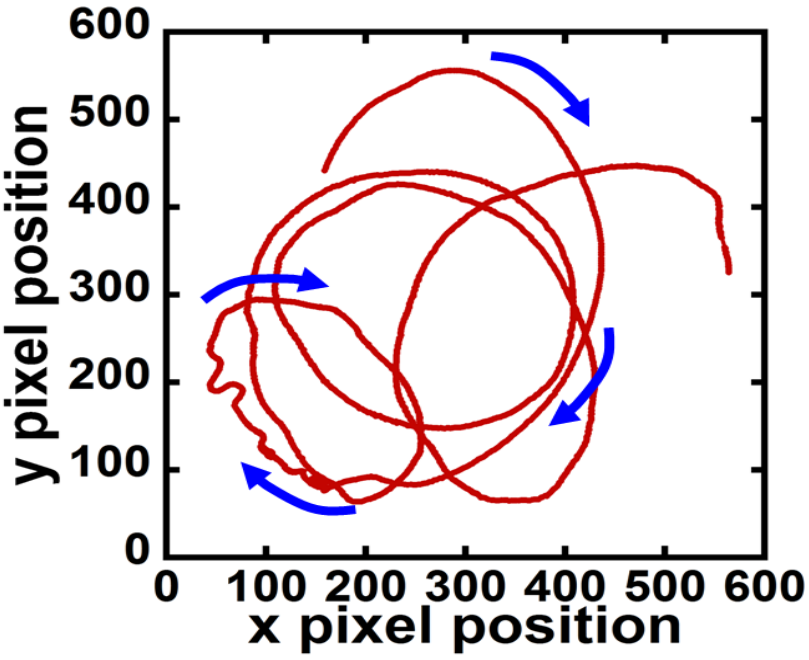

Figure 2.1: Extracted [x,y] trajectories for a single BQ disk from a 4 BQ disk experiment over a 12 min time frame. The [x,y] pixel trajectories demonstrates the clockwise circular motion observed during symmetrical disk shape.

2.4.2 Cooperative Collisions of Multiple Benzoquinone Disks

In addition to circular motion, BQ particle locomotion in a straight, translational directionality was significantly prevalent for the first 8.5 min but was observed throughout the entire self-motion time frame. In the presence of multiple BQ disks, collisions with either another particle or the glass wall occurred (**Supplementary Video 2.1**). These collisions can result in tandem disk locomotion. Superimposed still shots shown in **Figure 2.2A** exhibit an example of particle collision. More specifically, two 3 mm BQ disks from different directions (**Figure 2.2A** Step 1) collide (**Figure 2.2A** Step 2) and then deflect (**Figure 2.2A** Step 3). These collisions sometimes occur with more than two disks. **Figure 2.2B** demonstrates that as the number of BQ particles within a single dish increased, a linear increase in particle collisions was observed. Collisions predicted by the quadratic increase in **Figure 2.2B** (**Equation 2.1**) were plotted along with experimental collisions acquired from the 2 BQ disk series data, followed by calculating k, from

$$N_{collisions}^{BQ} = k(n)(n-1) \qquad \textbf{Equation (2.1)}$$

where N is the number of collisions, k is a constant and n is the number of BQ disks contained within the single glass petri dish. We assumed the collisions acquired from the 2 BQ disk series were random and kept k constant to acquire the k (n)(n-1) line (**Figure 2.2B** Blue line). However, this random collision model does not fit experimental data that shows fewer than the random collisions. Thus, we conclude that collisions between BQ disks are not random but follow a linear proportionality to n, which is further addressed in the discussion section.

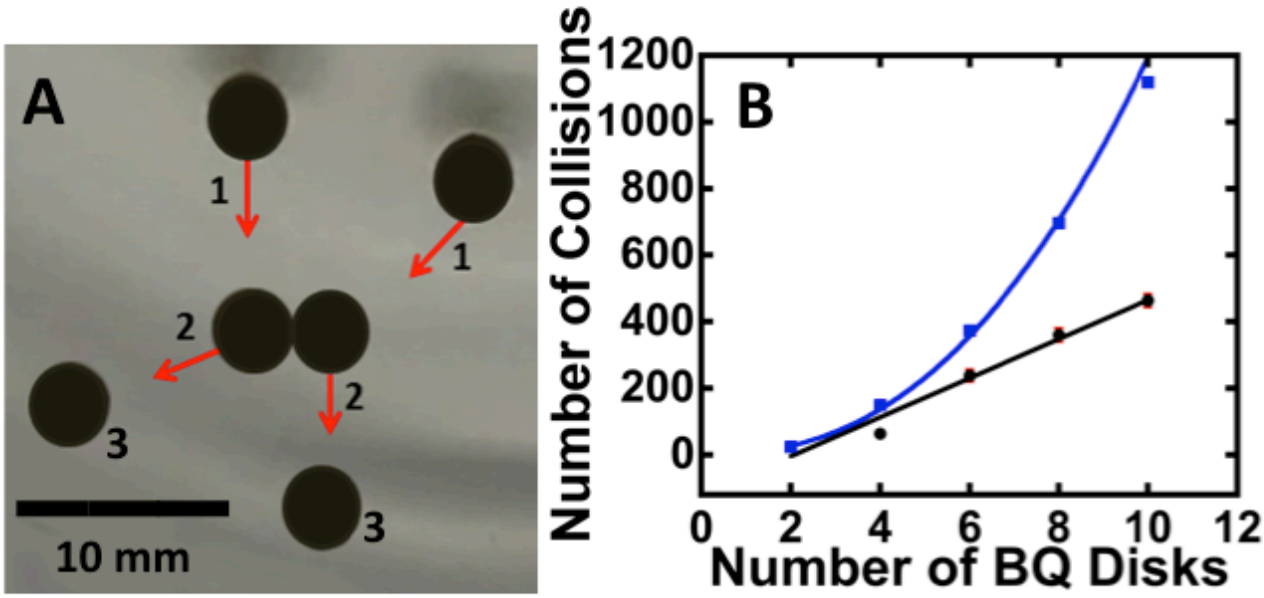

Figure 2.2: Illustration of BQ particle collisions. A) Superimposed snapshots at 1 s time intervals demonstrating the progression of BQ particle collision. Two different 3 mm BQ disk voyage from different directions [1] collide with one another [2] then deflect in different trajectories [3]. B) A linear increase in the number of collisions was observed during a 20 min time frame as the number of BQ disks contained in a single dish increased (black line). Blue line from theory of random collisions, calculated by the empirical formula (**Equation 2.1**).

2.4.3 Cooperative Coupling of Multiple Benzoquinone Disks

Collisions seen during self-motion and coupling resulted sporadically between multiple BQ disks. Co-operative coupling, i.e. two or more particles moving in tandem for a period of time, was an important characteristic feature as illustrated by **Supplementary Video 2.2**. Coupled disks subsequently voyaged with one another for seconds to several minutes. **Figure 2.3A** shows superimposed snapshots for coupled locomotion of two 3 mm BQ particles with a 1

s time interval. Linear increased coupling was observed when the number of BQ disks contained within a single dish increased, as shown in **Figure 2.3B**. More specifically, this co-operative behavior was infrequently observed during the first 5 min; however, significant coupling was observed after ~8 min.

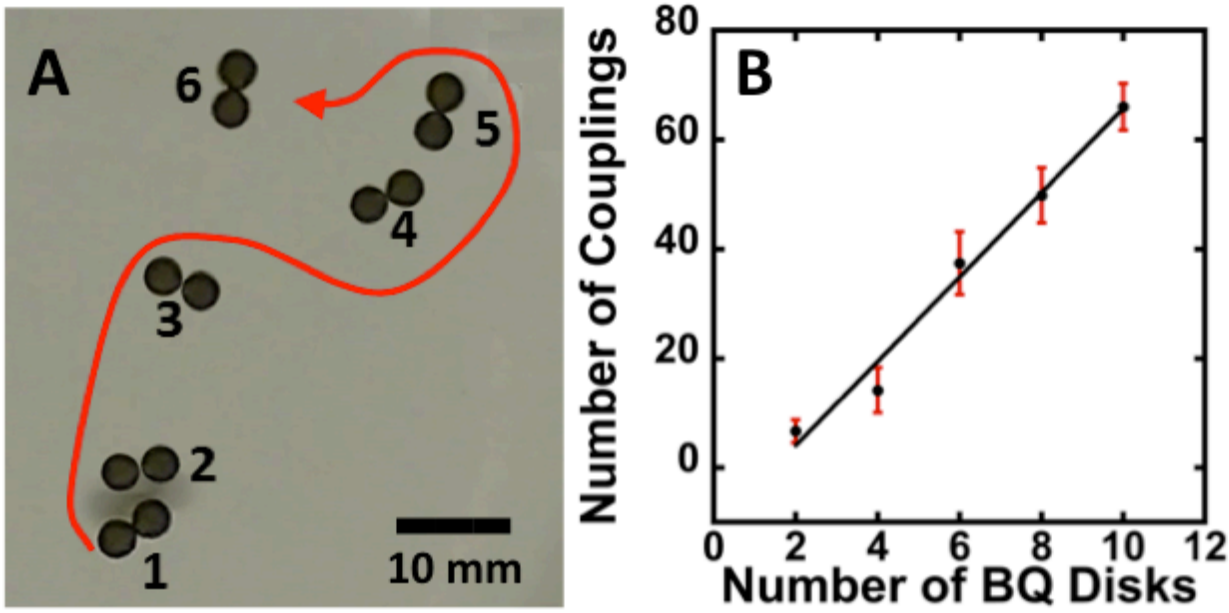

Figure 2.3: Illustration of two BQ particles voyaging in tandem. A) Superimposed snapshots at 1 s time intervals demonstrating the progression of BQ particle coupling. B) A linear increase in the number of couplings was acquired during a 20 min time frame as the number of BQ disks contained in a single dish increased.

Furthermore, multiple couples emerged for the 4, 6, 8 and 10 particle series, an example is shown in **Supplementary Video 2.3**. For example, 10 BQ disks displayed multiple co-operative couplings as demonstrated in 1 s time interval snapshots shown in **Figure 2.4A-F**. **Figure 2.4A** reveals locomotion of 3 two-particle couples, which formed when independently moving disks collided. These 3 two-particle couples continued in tandem locomotion (**Figure**

2.3B). After an additional second, further co-operative events transpired, observed by a two-particle couple collision with single BQ disk (**Figure 2.3C**). This triplet BQ collective then collided with the neighboring two-particle couple to form a five-particle collective (**Figure 2.3D** and **E**), which after 1 s broke into a two-particle and four-particle collective, which voyaged on. These multiple collectives maintain self-motion for seconds to several minutes as well as had both circular orbital and linear translational motion. Consequently, the frequency of multiple co-operative coupling events increased with increased BQ particles.

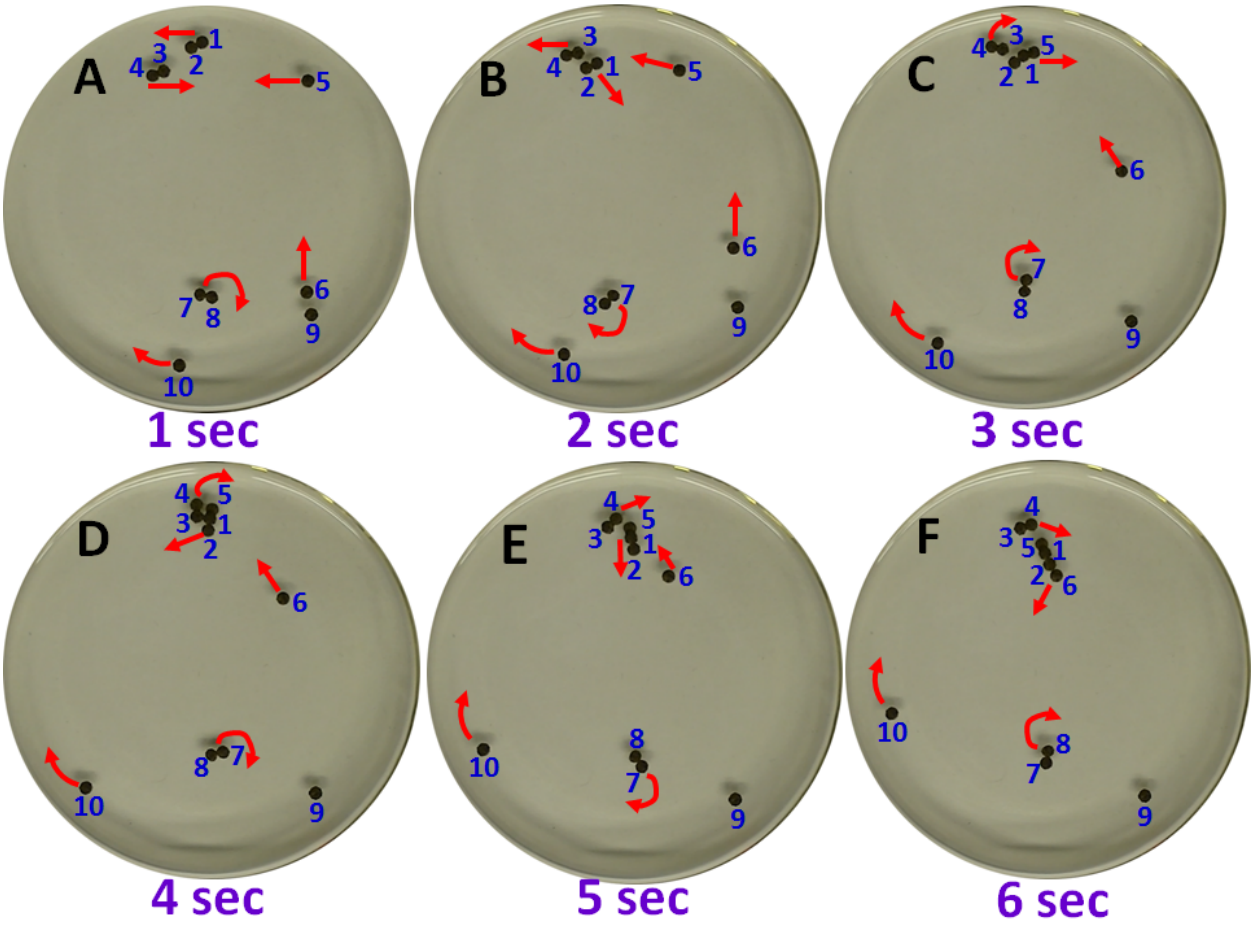

Figure 2.4: Snapshots at 1 sec time intervals for 10 BQ disks, individual numbered, contained in a single petri dish. Each frame demonstrates multiple co-operative coupling events can occur and through self-motion the co-operative couplings may acquire other BQ disks.

2.4.4 Evaluation of Concentration Gradient Formation

Continuous self-motion at the air-water interface is accompanied by BQ dissolution into the aqueous phase as discerned by the change in color of both the solution and particles, as well as, developing asymmetry in the disk shapes. Locomotion caused the solution to become yellow after several trajectories; therefore, time variation UV measurements were acquired to evaluate the BQ concentration. The absorbance was measured at 245, 270 and 300 nm. An absorption peak for hydroquinone (HQ), the reduction product of BQ, was not detected suggesting that redox reaction is not a major factor in self-motion. **Figure 2.5** demonstrates that as self-motion progresses, to either complete termination of motion (disks sank) or complete dissolution of BQ into the aqueous phase, an inhomogeneous concentration gradient is obtained. More specifically, the non-linear increase in concentration signifies heterogeneous dissolution. Therefore, it is very likely that non-uniform interfacial tension gradients are formed around multiple BQ particles to drive the self-motion.

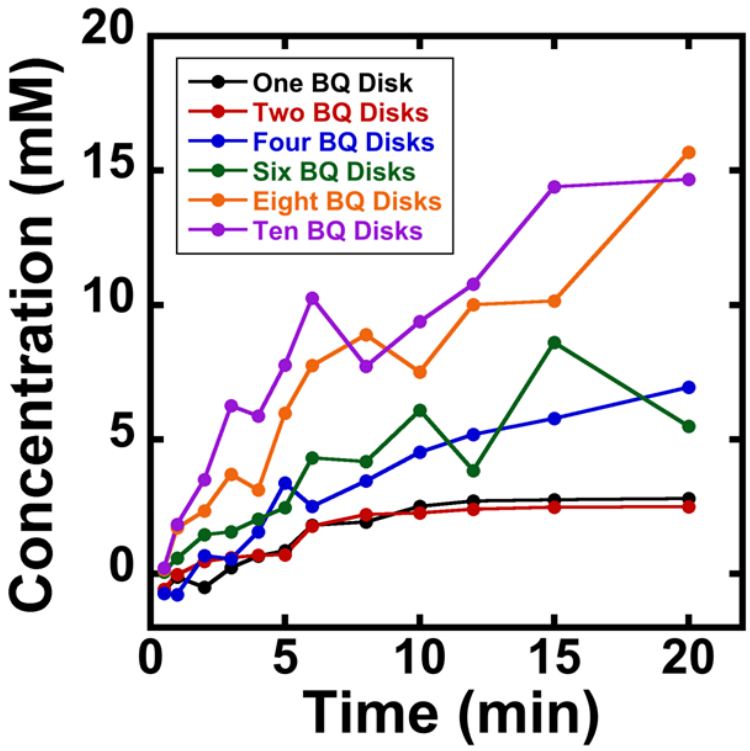

Figure 2.5: Concentration of BQ for each particle series acquired at different time variations to demonstrate heterogeneous BQ dissolution during self-motion progression. Change in concentration was estimated using a standard BQ calibration curve.

2.4.4 High Frequency Cycling of Asymmetric Benzoquinone Disks

Irregular dissolution generated asymmetrical BQ disks. More specifically, 3 mm circular green disks transitioned to irregularly shaped dark green particles. For each BQ disk series, the progression from symmetrical to asymmetrical disk shape varied and was sensitive to the characteristic motions of the particles. However, once irregularly shaped BQ particles were formed, both coupling and circular orbital motion (**Figure 2.6A**) events increased after ~ 8 to 12 min. These small asymmetrical BQ pieces, shown in **Figure 2.6B**, predominantly maintained circular motion with minor translational motion (**Supplementary Video 2.4**). This predominate circular motion was observed to occur at a much higher frequency and with a much smaller

circular diameter shown in **Figure 2.6A**. More precisely, extracted coordinates in **Figure 2.6C**, show the [x,y] diameters are much smaller compared to the symmetrical BQ particles [x,y] diameters in **Figure 2.1**. We term this circular orbital motion of these asymmetrical BQ particles, as cycling. These cycling events occur in both clockwise and counterclockwise directions.

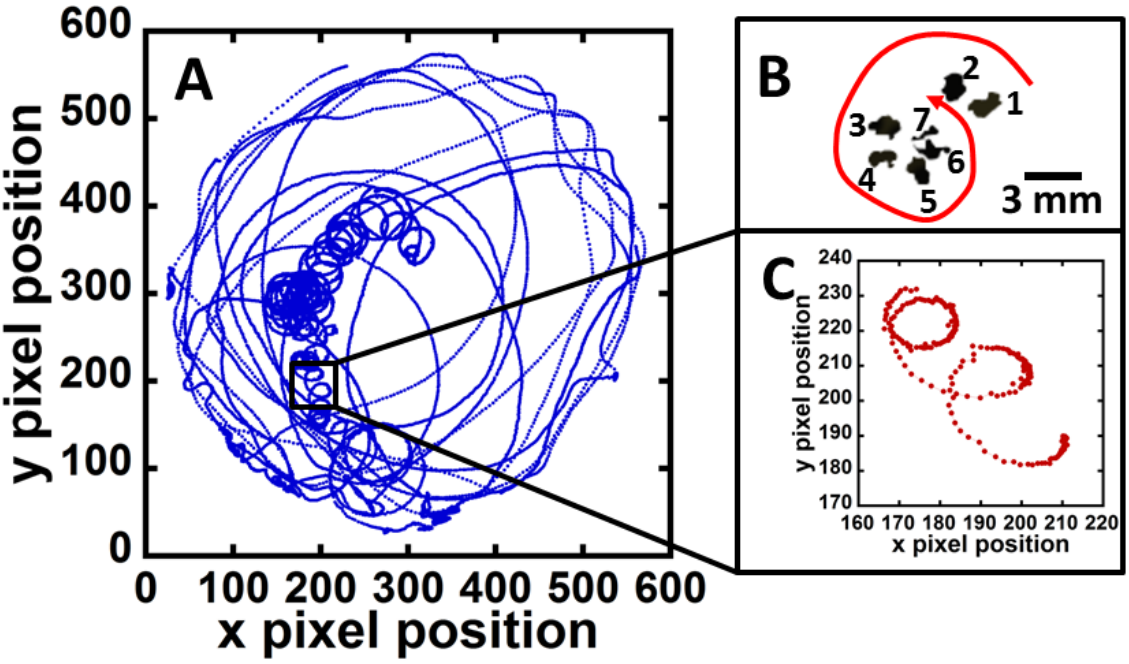

Figure 2.6: Trajectories demonstrating high frequency cycling were observed once the BQ particle becomes irregularly shaped. (A) Full [x,y] trajectories for 1 BQ disk from a 4 BQ disk series. B) Superimposed snapshots at 0.5 s time intervals to illustrate the irregular BQ particle shape. C) Extracted [x,y] trajectories after 12 min of self-motion to represent high frequency cycling.

2.4.6 Evaluation of Driving Motive Force of Self-Motion

To determine whether the driving motive force was reliant on interfacial tension gradients, a strongly surface-active Tween-20 was employed before and during particle disk

locomotion. First, preceding BQ particle motion at the interface, one drop of diluted Tween-20 (0.05% v/v) was placed in the center of the glass petri dish containing 100 mM aqueous NaCl. Once the solution stabilized, BQ particles were then dropped onto the air-water interface but no motion was observed. When diluted Tween-20 (0.05% v/v) was added during a BQ particle locomotion experiment, instantaneous termination of spontaneous motion occurred (**Supplementary 2.5**). These experiments suggest that the highly surface active Tween-20 forms a surface active molecular monolayer on the air-water interface to lower interfacial tensions to a common value that completely overwhelms the less surface active BQ driven interfacial tension gradients, thus removing the driving force for particle motion.

2.4.7 Collective Cooperative Motion of Irregularly Shaped Benzoquinone

Due to the above observations concerning irregularly shaped particles, we did a study starting with irregularly shaped BQ pieces at the air-water interface. Small collections of BQ pieces were prepared as mentioned prior. These pieces interacted and co-operative flocking (i.e. moving in groups) was observed. A fraction, ~6-10 out of 20, of the irregularly shaped particles moved collectively for different time periods, as illustrated in **Supplementary Video 2.6**. During this 62 sec video clip, particle flocking was observed and superimposed snapshots in **Figure 2.7** demonstrate an example of flocking events that emerged. The BQ pieces represented in green were the earliest time interval and two major flocks are observed one group of 6 BQ pieces and one group of 4 BQ pieces developed. Then after 4 s translational motion one collective of 7 BQ pieces developed, represented by the yellow collective, after an additional 4 s the collective moved to positions represented by the pink pieces and an 8 BQ flock formed. The co-operative flocks in **Figure 2.7** mentioned are highlighted in **Figure 2.8**. Locomotion of these small

collectives was fluent and while the collectives moved, each individual BQ piece demonstrated its own characteristic particle motions as described above.

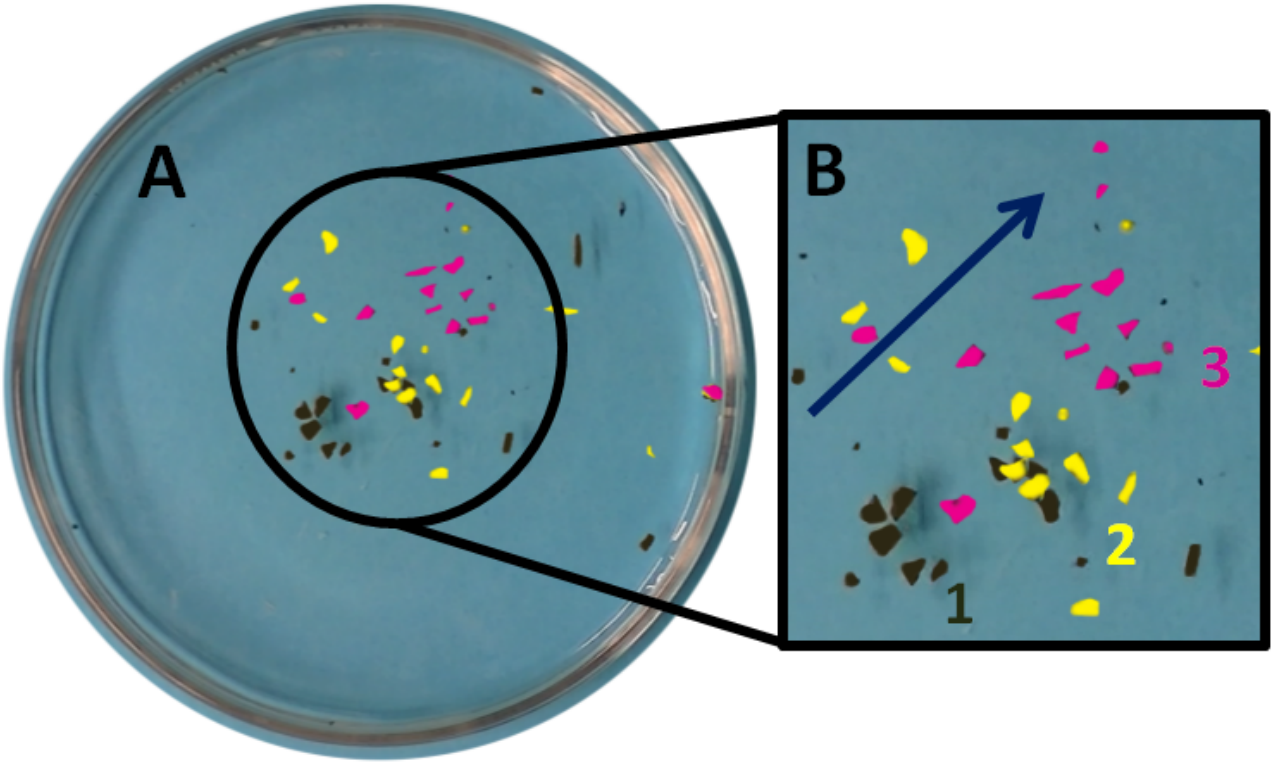

Figure 2.7 Superimposed snapshots at 4 s time intervals demonstrating the collective motion of multiple irregularly shaped BQ particles. The initial position of particles is shown in green [1] after 4 s of translational motion collectively they travelled to position [2] and after an additional 4 s of translational motion the collectives groups were at position [3]. Individual particles maintained their own characteristic motion.

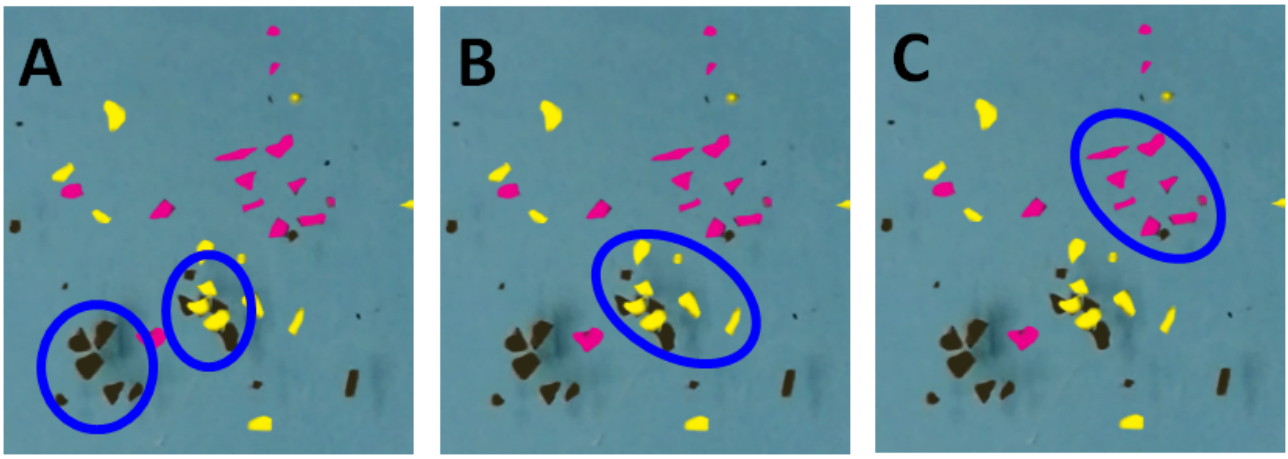

Figure 2.8 Extracted the superimposed snapshots at 4 s time intervals of Figure 7B to highlight the flocks described in the Results section. A) Blue circle around green BQ pieces highlights two co-operative flocks formed during self-motion. B) Blue circle around yellow BQ pieces highlights one co-operative flock that formed after an additional 4 s translational motion. C) Blue circle around pink pieces highlights the new co-operative flock that transpired after an additional 4 s translational motion.

2.4.8 Effect of Salt Concentration on Self-Motion

Different salt concentrations revealed small differences in locomotion of BQ particles. Concentrations from 0 to 500 mM NaCl were used in the aqueous phase and irregularly shaped BQ pieces were deposited on the air-water interface. A weak salt dependence resulted in self-motion similar to that at 100 mM (**Supplementary Video 2.7**), but flocking events at <100 mM NaCl appear to transpire for longer periods of time. However, at 500 mM NaCl (**Supplementary Video 2.8**), self-motion resolved to intermittent or no motion after 1-2 min.

2.5 Discussion

Multiple BQ particles at the air-water interface demonstrated predominately spontaneous continuous motion, along with collisions, cycling, co-operative coupling and collective motion. The motion patterns were highly dependent on particle shape and size. Experimental results and fundamental understanding from related studies provides a basis for interpreting the influences that cause the observed motions.[23-26] The driving motive force originates from inhomogeneous interfacial tension gradient fields (reflecting interfacial free energy fields) and the consequent hydrodynamic flows that develop around the BQ particles due to slow dissolution.

2.5.1 Explanation for Emergence of Spontaneous Continuous Self-Motion

Instantaneous locomotion of BQ particles at the air-water interface occurs and continuous, uniform motion ensues. This motion results in BQ dissolution in the aqueous phase as well as successive introduction of BQ molecules at the air-water interface; this occurs for each individual disk.[23-26] More specifically, a monolayer of BQ spreads over the surface as it dissolves and the spreading BQ layer decreases the interfacial tension of the interface.[24] If the formation and spreading of the layer is non-uniform, then the resulting interfacial tension gradient exerts a force on the BQ disk in the direction of higher interfacial tension, since by traveling in that direction further dissolution will decrease interfacial tension and interfacial free energy in that new area of a pellet, the sum of the interfacial tensions at the liquid-air, solid-air and solid-liquid tensions. That is,

$$\gamma = \gamma_{AW} + \gamma_{SA} + \gamma_{SW} \qquad \textbf{Equation (2.2)}$$

in which subscripts AW, SA and SW are the interfacial tensions at the air-water, solid-air and solid-water interfaces (see **Figure 2.9A**). Then the net interfacial-tension force F on a BQ pellet can now be written as an integral:

$$\boldsymbol{F(t) = \oint \gamma(x, y, t)\,dl} \qquad \textbf{Equation (2.3)}$$

in which the integration is over the entire edge of the pellet. In this integral, we have indicated the time dependence of $\boldsymbol{\gamma}$ explicitly. If $\boldsymbol{\gamma}$ is uniform, the net force F would be zero. Non-uniformity of $\boldsymbol{\gamma}$ along the edge of the pellet results in a net force that moves the disk. The change in Gibbs energy may be expressed as

$$dG = \mathbf{F} \bullet d\mathbf{r} \qquad \textbf{Equation (2.4)}$$

in which d**r** = (dx, dy) is the displacement (see **Figure 2.9B**). In the presence of multiple particles, the inhomogeneous interfacial tension gradients are overlapped and amplified. **Figure 2.5** is the result of heterogeneous BQ dissolution due to the scattered, non-linear increase in the concentration of BQ with time. Non-uniformity within interfacial tension gradients produces a driving force great enough to accelerate the multiple disks at once.

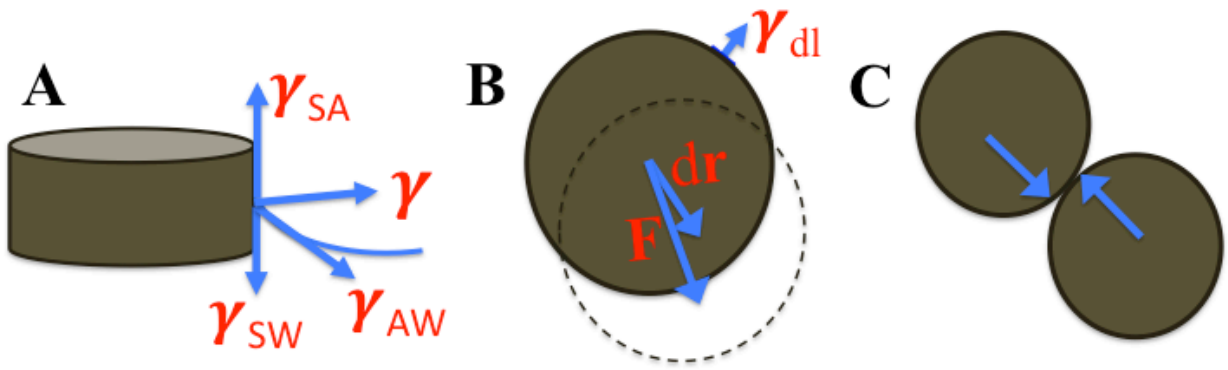

Figure 2.9: Schematic representation of mechanism for BQ self-motion on water surface. A) Surface tension (γ) fields are shown for $\boldsymbol{\gamma}_{SW}$ (solid-water), $\boldsymbol{\gamma}_{AW}$ (air-water), and $\boldsymbol{\gamma}_{SA}$ (solid-air)

B) Illustration of net interfacial tension force (F) C) Diagram of attractive interactions between BQ disks.

2.5.2 Explanation for Emergence of Disk Collisions

Once BQ particles have the driving force to accelerate, then particle shape and flow currents determine directional trajectories. BQ particles remain symmetrical and are upheld at the air-water interface for 5-10 min and prevalent particle collisions (**Figure 2.2A**) are observed, as seen by the linear increase in **Figure 2.2B**. A scenario to explain these particle collisions is as follows. While locomotion of the BQ particles occurs, individual particles have specific surface free energy gradients. Thus, neighboring particles begin to be influenced by these alternate interfacial tension gradients. A given particle's interfacial tension gradients and velocity fields stimulate surrounding particles. This influence generates movement toward the favoring field resulting in either collisions or collisions followed by coupling.

The number of collisions that occurred between BQ disks was proportional to n (**Figure 2.2B**) rather than n(n-1) as predicted by the random collisions (**Equation 2.1**). The collision frequency depends on the average speed of the disk as well as long-range interactions of the disks through the heterogeneous interfacial tension fields that govern the motion of the disks. Velocities of the BQ disks are influenced by the local interfacial tension gradients, not its absolute value. It is possible that the gradients decrease with increasing number of disks. Let us assume that the disks "collide" when the distance between their centers is d. If v is the average relative velocity, then the number of collisions per unit time for an uncorrelated random motion is:

$$\boldsymbol{Z = \pi d^2 v\, n(n-1)} \qquad \textbf{Equation (2.5)}$$

If we now assume that the decrease in average speed is proportional to the inverse of the number of particles, then, by setting $\boldsymbol{v = b/n}$ we find that

$$\boldsymbol{Z = \pi d^2 b(n-1)} \qquad \textbf{Equation (2.6)}$$

which gives a linear relationship between the collision frequency Z and n. However, this assumption means that the average relative velocity with 8 BQ disks will be half that of 4 BQ disks, which was clearly not observed in our system. If we assume $\boldsymbol{v = v_0 - (b/n)}$, that still leaves a quadratic relation between Z and n. Hence, while $\boldsymbol{v}$ might decrease with increasing n, as Soh et al. [37] reported for the case of camphor-filled gel disks, additional factors are needed to explain the linear dependence of Z on n. One possibility is the effective long-range interactions between the BQ particles through the interfacial tension fields. In general, this leads to repulsive forces. This in turn reduces the effective area in which a disk moves and thus the number of collisions. Indeed, in the case of camphor-filled gel disks, when a sufficient number of disks are in the system, the repulsive forces lead to a lattice structure in which the disks do not "collide" at all.[37] Thus, the linear dependence of "collisions" on n is at least partially a result of the disks interaction through the interfacial tension field, not merely the decrease in average speed with increasing number of disks. While further theoretical and experimental investigations are necessary to fully understand the reasons for the linear dependence of collision frequency on the number of disks, the result underscores the difference between self-moving particles and thermal motion.

Unlike force fields of molecules that are functions of distance from the molecule, the interfacial tension field surrounding a disk is not a time-invariant function of distance from the disk. As a consequence, the force on the disk at any time is not a function of the positions of all other disks, but a result of previous motion. This leads to complexity and co-operativity that is

entirely different from random motion of molecules. Our result is only a preliminary indication that this complex co-operativity may be reflected in the dependence of the number of collisions on the number of disks.

2.5.3 Explanation for Cooperative Disk Coupling

An attractive force between BQ particles induces particle collisions or collisions resultant in tandem to give multiple particle coupling events. A possible scenario to explain these attractive interactions is as follows. Disk locomotion at the interface occurs in the direction in which the rate of dissolution of BQ onto the water surface is lower than that in alternate directions; locomotion is in the direction of the net force as expressed in **Equation 2.3** and illustrated in **Figure 2.9B**. As BQ disks approach one another, the net force on the disks can align but when opposite in direction their surfaces collide with one another. This occurrence further reduces the rate of dissolution at the disk contact point while the non-contacted edges continue to dissolve and reduce the surrounding interfacial tension fields. Consequently, these net forces become concentrated toward the contact point. When the net forces are not perfectly aligned (**Figure 2.9C**), there is a net torque on the coupled particles that results in disk rotation. Time variations of the net forces are a result of a complex interplay between disk locomotion and heterogeneous interfacial tension fields around the particles.

2.5.4 Rationalization for Asymmetrical Disk Locomotion

BQ dissolution eventually induces asymmetry of the BQ particle disks. Once asymmetry occurs, representing even a slight variation from the 3 mm disks shape, high frequency cycling (**Figure 2.6**) is observed. We propose that irregular dissolution of BQ lowers the interfacial tension near points or edges of the disk (i.e., at locations where it is most rapidly dissolving)

compared to other regions on the particle influencing the characteristic motions observed.[35,36] More specifically, interfacial regions near BQ particle points and edges are likely to have a lower γ than other regions. Theses interfacial tension differences at specific points on the asymmetric disk produce an irregular driving force around the BQ particles; therefore, acceleration of the particle is asymmetric. Thus, motion switches from translational motion to high frequency, small diameter circular motion, as observed in [x,y] trajectories in **Figure 2.6A** and **C**.

2.5.5 Interpretation of Driving Motive Force of Self-Motion

To further clarify the driving motive force was dependent upon interfacial tension gradients, addition of a strong surface-active chemical, Tween-20, was added to the system. Addition of this more surface-active compound compared to BQ results in instantaneous termination of motion. A detergent monolayer is formed at air-water interface and solid-water interface, which consequently stabilizes γ_{AW} and $\gamma_{SW;}$ therefore, destroying any interfacial driving force for motion. This supports the view that localized interfacial tension is the key driving force, since the strong surfactant lowers the air-water interfacial tension by a large amount over the entire water surface and destroys any gradients from the less surface active BQ molecules around the particles.

2.5.6 Collective Cooperative Motion of Irregularly Shaped Benzoquinone Particles

Of most interest is that multiple irregularly shaped BQ disks, which were widely different in both size and shape per experiment, exhibited co-operative coupling (similar to **Figure 2.3** and **2.4**) and collective motion that could be called "flocking" (**Figure 2.7**) for different time periods. The dynamic flock moves like a flock of birds, with pieces of BQ particles associating and disassociating with the flock. As seen in **Figure 2.7**, transient self-organized flocking among a

fraction of particles emerges while being coexistent with other particles in random motion. It is remarkable that out of irregularly shaped pieces of BQ particles such co-operative flocking motion emerges.

There have been a number of motion studies of camphor particles on water. BQ on 0.1 M NaCl features different types of interfaces compared to camphor on water. The BQ system presents a particle with a high-energy surface that is easily wetted and likely to recruit adsorbed ions, while camphor on water represents a hydrophobic, low energy surface with no ionic adsorption. Despite these differences, the driving forces for both motions most likely involve varying interfacial free energy fields. A somewhat similar behavior termed "swarming" has been previously reported in collection of camphor-filled gel particles by Soh et al..[37, 38] In these studies, the particles shapes and sizes were carefully engineered. Soh et al. conducted a very detailed analysis of the hydrodynamic flows that result from surface tension gradients and reported that a collection of one arrow-shaped particle and five or six rod shaped particles exhibited collective motion. Interestingly, the direction of motion changed when the depth of the fluid was changed. In this study, the shapes of the disks determined the geometry of the swarm: e.g. the arrow-shaped particle with a "tail" of bar-shaped particles.

While the self-motion systems studied by Soh et al. [37, 38] have bare basic similarities to our system, but there are important differences. Our system consists of co-operative motion in BQ particles while the above-mentioned systems are gel-filled camphor particles. The sublimation rate of camphor, an important factor in driving motion of camphor particles, is very large compared with that of BQ. The motion we observed seems to be driven mostly through spreading of BQ on the surface and subsequent dissolution.

Soh et al. fabricated camphor-gel particles that repelled each other at liquid depths larger than 1.8 mm; in addition, different solution depths provided either random motion (depths larger than 1.8 mm) or lattice formation (1.4 – 1.8 mm).[37,38] In our case, both attractive and repulsive forces contribute to the particles co-operative flocking motion, which occurred at a depths as large as 3.9 mm. Our system demonstrated continuous, transient flocking with minimal manipulation of the chemical material. The most significant difference in behavior we report is that the disks need not be carefully engineered to have particular shapes; it can emerge from arbitrary shapes and sizes that result when a circular disk is broken into several pieces. Furthermore, the particles trapped within the flock maintain some degree of free motion and the flock does not have a fixed formation as in the systems Soh et al. reported. [37, 38]

Suematsu et al also reported that collections of camphor particles exhibited collective intermittent motion.[39] Due to mutual repulsion, the particles remain apart and stationary for a time and, due to fluctuations, this metastable configuration is disturbed and the collection of particles quickly moves to another metastable configuration. This co-operative motion is distinct from the flocking behavior we report here or the swarming behavior that Soh et al.[38] have reported.

Not unexpectedly, BQ flocks also exhibited a form of taxis, toward a region of higher temperature. Since the hotter region of the surface dissolves and evaporates solute faster, the concentration, and hence the interfacial tension, on the surface is lower in warmer region. This causes the particles to move to the warmer region. Similar taxis towards warmer locations was also observe for the camphor-filled gel particles by Soh et al.[38]

We would also like to note a more general thermodynamic aspect of interfacial tension drive motion of collections of particles. The motion of these particles increases the rate of

chemical conversion of the initial compound to the final product. This happens because the particles move towards locations of lower concentration and thus increase the rate of conversion. In thermodynamic terms, it means the rate of entropy production or Gibbs-energy dissipation is increased due to particle motion. In this case, the entropy production

$$\frac{d_i S}{dt} = \frac{A}{T}\left(\frac{d\xi}{dt}\right) \qquad \textbf{Equation (2.7)}$$

in this expression, A is the affinity of chemical reaction, which equals the difference in chemical potentials of the reactants and the products, and $(d\xi/dt)$ is the rate of conversion to the product. Other non-equilibrium systems also exhibit similar increase in the rate of entropy production.[40] In particular, it was reported that a system driven by electrical voltage form worm-like structures, which move so as to increase the rate of entropy production.[40] When subjected to non-equilibrium thermodynamic forces, these systems respond so as to increase the rate of entropy production. It would be interesting to see if this tendency will result in some interesting behavior of the BQ flocks similar to taxis towards warmer temperatures.

2.6 Conclusion

Results described above illustrate a novel multiple particle self-motion system. Spontaneous, continuous and intermittent motions of multiple BQ disks transpired and characteristic motion such as collisions, cycling, co-operative coupling and collective motion was observed. These characteristic motions can be explained by interactions between inhomogeneous interfacial tension gradients formed as the particles slowly dissolve. This present system is primitive and the first step at describing collective self-motion of multiple objects. Further studies of the underlying thermodynamic principles involving the effects of particle shape are underway in attempts to control the collective motion.

2.7 Acknowledgments

This work was supported financially by National Science Foundation's INSPIRE Track 1 Program, Grant No. BCS-1344725. We thank Professors Michael Turvey and Claudia Carello (University of Connecticut) for helpful discussion.

2.8 References

1. Colberg, P. H.; Reigh, S. Y.; Robertson, B.; Kapral, R. Chemistry in Motion: Tiny Synthetic Motors. *Acc. Chem. Res.* **2014**, *47*, 3504-3511.
2. Wang, W.; Duan, W.; Ahmed, S.; Mallouk, T. E.; Sen, A. Small power: Autonomous nano- and micromotors propelled by self-generated gradients. *Nano Today* **2013**, *8*, 531-554.
3. Brady, J. F. Particle motion driven by solute gradients with application to autonomous motion: continuum and colloidal perspectives. *J. Fluid Mech.* **2011**, *667*, 216-259.
4. Paxton, W. F.; Baker, P. T.; Kline, T. R.; Wang, Y.; Mallouk, T. E.; Sen, A. Catalytically Induced Electrokinetics for Motors and Micropumps. *J. Am. Chem. Soc.* **2006**, *128*, 14881-14888.
5. Ikezoe, Y.; Washino, G.; Uemura, T.; Kitagawa, S.; Matsui, H. Autonomous motors of a metal-organic framework powered by reorganization of self-assembled peptides at interfaces. *Nat. Mater.* **2012**, *11*, 1081-1085.
6. Paxton, W. F.; Sundararajan, S.; Mallouk, T. E.; Sen, A. Chemical locomotion. *Angew. Chem. Int. Ed.* **2006**, *45*, 5420-5429.
7. Ismagilov, R. F.; Schwartz, A.; Bowden, N.; Whitesides, G. M. Autonomous movement and self-assembly. *Angew. Chem. Int. Ed.* **2002**, *41*, 652-654.
8. Hong, Y.; Velegol, D.; Chaturvedi, N.; Sen, A. Biomimetic behavior of synthetic particles: from microscopic randomness to macroscopic control. *Phys. Chem. Chem. Phys.* **2010**, *12*, 1423-1435.
9. Huxley, H. E. Mechanism of muscular contraction. *Science.* **1969**, *164*, 1356-1366.
10. Wegmann, R. Our Molecular Nature. The Body's Motors, Machines and Messages by D. S. Goodsell. *Cell. Mol. Biol. (Paris)* **1997**, *43*, 254.
11. Rayment, I.; Holden, H. M.; Whittaker, M.; Yohn, C. B.; Lorenz, M.; Holmese, K. C.; Milligan, R. A. Structure of the actin-myosin complex and its implications for muscle contraction. *Science (Washington, D. C., 1883-)* **1993**, *261*, 58-65.
12. Berg, H. C. The rotary motor of bacterial flagella. *Annu. Rev. Biochem.* **2003**, *72*, 19-54.
13. Zhao, X.; Norris, S. J.; Liu, J. Molecular architecture of the bacterial flagellar motor in cells. *Biochemistry* **2014**, *53*, 4323-4333.
14. Lodish, H. *Molecular Cell Biology, 6th Edition;* W. H. Freeman: New York, 2008.
15. Kishimoto, U. Rhythmicity in the protoplasmic streaming of a slime mold, Physarum polycephalum. II. Theoretical treatment of the electric potential rhythm. *J. Gen. Physiol.* **1958**, *41*, 1223-1244.
16. Matsumoto, K.; Takagi, S.; Nakagaki, T. Locomotive mechanism of Physarum plasmodia based on spatiotemporal analysis of protoplasmic streaming. *Biophys. J.* **2008**, *94*, 2492-2504.
17. Nakagaki, T.; Yamada, H.; Toth, A. Intelligence: Maze-solving by an amoeboid organism. *Nature (London)* **2000**, *407*, 470.
18. Latty, T.; Beekman, M. Speed-accuracy trade-offs during foraging decisions in the acellular slime mould Physarum polycephalum. *Proc Biol Sci* **2011**, *278*, 539-545.
19. Bain, C. D.; Burnett-Hall, G.; Montgomerie, R. R. Rapid motion of liquid drops. *Nature (London)* **1994**, *372*, 414-415.
20. de Gennes, P. G. The dynamics of reactive wetting on solid surfaces. *Physica A (Amsterdam)* **1998**, *249*, 196-205.

21. Sekimoto, K. Langevin equation and thermodynamics. *Prog. Theor. Phys. Suppl.* **1998**, *130*, 17-27.
22. Nakata, S.; Doi, Y.; Hayashima, Y. Intermittent Motion of a Camphene Disk at the Center of a Cell. *J. Phys. Chem. B* **2002**, *106*, 11681-11684.
23. Suematsu, N. J.; Ikura, Y.; Nagayama, M.; Kitahata, H.; Kawagishi, N.; Murakami, M.; Nakata, S. Mode-Switching of the Self-Motion of a Camphor Boat Depending on the Diffusion Distance of Camphor Molecules. *J. Phys. Chem. C* **2010**, *114*, 9876-9882.
24. Suematsu, N. J.; Miyahara, Y.; Matsuda, Y.; Nakata, S. Self-Motion of a Benzoquinone Disk Coupled with a Redox Reaction. *J. Phys. Chem. C* **2010**, *114*, 13340-13343.
25. Nakata, S.; Matsuda, Y.; Ikura, Y. S.; Takeda, A.; Izumi, S. Mode Change in the Self-Motion of a Benzoquinone Disk Coupled with a NADPH System. *Chem. Phys. Chem.* **2012**, *13*, 520-524.
26. Matsuda, Y.; Suematsu, N. J.; Nakata, S. Photo-sensitive self-motion of a BQ disk. *Phys. Chem. Chem. Phys.* **2012**, *14*, 5988-5991.
27. Nakata, S.; Iguchi, Y.; Ose, S.; Kuboyama, M.; Ishii, T.; Yoshikawa, K. Self-Rotation of a Camphor Scraping on Water: New Insight into the Old Problem. *Langmuir* **1997**, *13*, 4454-4458.
28. Kohira, M. I.; Hayashima, Y.; Nagayama, M.; Nakata, S. Synchronized self-motion of two camphor boats. *Langmuir* **2001**, *17*, 7124-7129.
29. Nakata, S.; Murakami, M. Self-Motion of a Camphor Disk on an Aqueous Phase Depending on the Alkyl Chain Length of Sulfate Surfactants. *Langmuir* **2010**, *26*, 2414-2417.
30. Nakata, S.; Matsuo, K. Characteristic Self-Motion of a Camphor Boat Sensitive to Ester Vapor. *Langmuir* **2005**, *21*, 982-984.
31. Kitahata, H.; Iida, K.; Nagayama, M. Spontaneous motion of an elliptic camphor particle. *Phys. Rev. E: Stat., Nonlinear, Soft Matter Phys.* **2013**, *87*, 010901/1-010901/4.
32. Suematsu, N. J.; Nakata, S.; Awazu, A.; Nishimori, H. Collective behavior of inanimate boats. *Phys. Rev. E: Stat., Nonlinear, Soft Matter Phys.* **2010**, *81*, 056210/1-056210/5.
33. Nakata, S.; Arima, Y. Self-motion of a phenanthroline disk on divalent metal ion aqueous solutions coupled with complex formation. *Colloids Surf. , A* **2008**, *324*, 222-227.
34. Iida, K.; Suematsu, N. J.; Miyahara, Y.; Kitahata, H.; Nagayama, M.; Nakata, S. Experimental and theoretical studies on the self-motion of a phenanthroline disk coupled with complex formation. *Phys. Chem. Chem. Phys.* **2010**, *12*, 1557-1563.
35. Mosharraf, M.; Nystroem, C. The effect of particle size and shape on the surface specific dissolution rate of microsized practically insoluble drugs. *Int. J. Pharm.* **1995**, *122*, 35-47.
36. Jia, X.; Williams, R. A. From microstructures of tablets and granules to their dissolution behaviour. *Dissolution Technol.* **2006**, *13*, 11-19.
37. Soh, S.; Bishop, K. J. M.; Grzybowski, B. A. Dynamic Self-Assembly in Ensembles of Camphor Boats. *J Phys Chem B* **2008**, *112*, 10848-10853.
38. Soh, S.; Branicki, M.; Grzybowski, B. A. Swarming in Shallow Waters. *J. Phys. Chem. Lett.* **2011**, *2*, 770-774.
39. Suematsu, N. J.; Tateno, K.; Nakata, S.; Nishimori, H. Synchronized Intermittent Motion Induced by the Interaction between Camphor Disks. *J. Phys. Soc. Jpn.* **2015**, *84*, 034802/1 – 034802/6.
40. Kondepudi, D.; Kay, B.; Dixon, J. End-directed evolution and the emergence of energy-seeking behavior in a complex system. *Phys Rev E.* **2015**, *91*, 050902/1 -050902/5.

Chapter Three:

Flocking, Thermo-taxis, and Magneto-taxis in Collective Active Matter Benzoquinone Particles at the Air-Water Interface

3.1 Abstract

Collective self-motion of physical-chemical systems is a promising opportunity for studying and developing mechanical functions in inanimate systems. In this paper, we investigated further the spontaneous collective flocking motion of multiple solid macroscopic active matter benzoquinone (BQ) irregularly shaped fragments at the air-water interface. Self-propulsion transpired within the system without the intervention of chemical reactions, but rather due to complex Marangoni convection and foraging for inhomogeneous surface tension free energy. Interparticle hydrodynamic interactions at the points and edges of these irregularly shaped BQ particles lead to a cooperative behavior, termed *flocking*. Flocking behaviors were not clearly perceived in the high symmetric circular disk circumstance. This flock formation is an example of a non-equilibrium dissipative structure and we demonstrate our non-machined system has perception-action capabilities. In particular, collective locomotion of the flock was sensitive to warm and cool thermotaxis conditions observed by detection and corresponding response by these active BQ fragments. Furthermore, we developed a proto-sensor system, which was response to a secondary magnetic field, only when the primary field coupled with the flock structure composed of a sensor element (BQ-iron oxide particle) and multiple non-sensor elements (BQ particles). If the sensor element or the flock was absent in the system, magnetotaxis was not observed. Video analysis demonstrated the remarkable cooperative flocking behavior depended strongly on particle shape.

3.2 Introduction

Nonequilibrium self-organizing systems give us insight into the nature and origin of organisms.[1-6] Among these are systems that exhibit self-motion, systems that are broadly classified as *active matter*. Constituents (or active particles) of active matter are not in equilibrium with their environment and their self-motion is a consequence of the thermodynamic forces and flows that are driving them towards equilibrium.[7-10] Though thermodynamic forces, and the flows they drive, generate entropy that is usually associated with disorder, they can, in fact, drive the system to self-organize into a structure with lower entropy. Such a structure, called a *dissipative structure*, is maintained through continuous generation of entropy and dissipation of free energy.[2, 11]

Dissipative structures have been known for decades; simple examples include chemical clocks and chemical pattern formation.[1-6, 11, 12] These structures bear a strong similarity to the structures we see in biological organisms. Indeed, biological organisms are dissipative structures because their construction and function is founded on entropy generating processes.[13, 14] In this respect, non-living dissipative structures, which can be simple in their makeup but exhibit highly complex behavior, provide us with a means to study the underlying principles underlying in much more complex organisms. In other words a simple non-equilibrium system can show behavior such as foraging and seeking energy needed to sustain the structure and self-heal if the structure is damaged, behavior we see in biological systems.[15]

Prominent characteristics of dissipative structures are observed in many life forms and are a distinguishing property of living systems.[16, 17] Biological systems demonstrating this cooperative dynamic behavior is expansive. Examples include suspensions of swimming bacteria, gatherings of cell suspensions, collections of cytoskeletal filaments (actin fibers or

microtubules), and molecular motors (myosin or kinesin).[18, 19, 20, 21] Self-organized activity is connected to self-replication and self-motility in bacterial suspensions, while self-motion arises from treadmilling and motor-exerted non-thermal forces for both cytoskeletal filaments and molecular motors. [18, 19, 20, 21] Self-organized motions are not limited to the cellular level; cooperative dissipative structures are prevalent at diverse scales and levels of complexity. For example, this behavior also includes schools of fish, flocks of birds, insect swarms, and collections of mammals.[22, 23, 24, 25]

Dissipative structures in active matter are not limited to living systems, nonliving systems demonstrate self-organized structures, the mechanism of active motion may be diverse; however, the outcome of a dissipative structure is not different. Extensive research has been concentrated on developing nonequilibrium long-range order in nonliving systems to improve our understanding on the mechanisms propagating in living systems. In particular, literature establishes a wide range of mechanisms, chemical or physical, to explain the self-motion of nonliving systems, both experimentally and theoretically. A famous example is camphor crystals at an air-water interface. In these systems, an asymmetrical chemical reaction at the active particle surface and sublimation of camphor molecules creates differences in surface free energy and produces self-propulsion by taking advantage of free energy gradients.[26, 27, 28, 29] Further explorations have demonstrated camphor active particles have the capability of synchronized motion and collective swarming in multiple particles systems. [30, 31] Analogous to camphor, BQ and derivatives have been investigated.[32-36] Self-motion of the disk relied on heterogeneous interfacial tension gradients at the air-water interface. Previous single particle studies demonstrated distinctive motion, such as continuous, intermittent and velocity-decay, could be modulated by influences such as, redox reactions, UV light, and biochemical reactions.[32, 33, 34]

Single particle studies provided fundamental explanations on the driving motive forces; however, multiple particle systems are more important for comprehension of living active matter mechanisms.

Multiple particle component systems have been evaluated to ascertain interparticle interactions and provide insight on dissipative structure properties. For example, dynamic self-assemblies of meticulously engineered camphor-loaded gel particles have been studied extensively by others.[37, 38, 39, 40] Soh et al established that the arrangement of particle-particle repulsions and spatial restriction acting on particles lead to open-lattice structure assemblies.[41] A third mode, collective intermittent motion, emerged from Suematsu et al, in which these carefully designed camphor-filled particles remained apart and stationary due to mutual repulsion.[42] Then due to fluctuations, the metastable assembly was distressed and the collective relocated to an alternative metastable configuration.[42] Additionally, Soh et al engineered different geometries of these camphor-filled gel particles to control the collective behavior and drive the formation of a swarm.[43] Each of these aforementioned studies defined their dissipative structure to be behaving as a swarm, which is ubiquitous to biological systems. Swarming has become associated and defined in the literature as rhythmic synchronized motion and group leader collective motion in a concerted manner.[42, 43]

Our group described a similar behavior termed *flocking*; specifically we reported local heterogeneous surface free energy fields directed the cooperative flocking of multiple BQ particles.[44] More specifically, we demonstrated and characterized self-organization emerged spontaneously with multiple, non-engineered BQ fragments. We established the minimal conditions (different shaped and sized particles) under which self-organization emerged, such as paired travel and group motion, without the intervention of chemical reactions or light; but solely

by particle interactions between inhomogeneous interfacial tension gradients.[44] In our system, attractive and repulsive forces contributed to the particles continuous, transient cooperative flocking motion.[44] The most significant differences in the behavior reported are that engineered particles are not required and there is no group leader guiding the active particles toward a common pattern.

Our primitive observations previously reported lead to further detailed investigations to better understand and describe the dynamic features of the collective dissipative flock formed between multiple interacting active matter BQ particles. First, the effect of particle shape on the collective cooperative motion was evaluated. Herein, specifically, we demonstrate self-organization emerges spontaneously under ambient conditions for non-engineered irregularly shaped BQ fragments; whereas, this flock organization was not clearly observed in multiple highly, symmetric circular BQ disks. Furthermore, the transient self-propelled dissipative structure exhibited sensory response to two different thermotaxis conditions, in addition, the structure, as a complete entity became a magnetic field-sensing flock with the presence of a single sensor (BQ-iron oxide nanopowder) element. These dynamic behaviors emerged spontaneously and underlying thermodynamic principles have begun to be uncovered.

3.3 Experimental

3.3.1 Materials

1,4-Benzoquinone (BQ), iron (II, III) oxide nanopowder (Fe_3O_4, 50-100 nm particle size, 97% trace metal basis), lycopodium powder, and sodium chloride (NaCl) were purchased from Sigma Aldrich and used without further purification. Nanopure water (18 MΩ·cm) was obtained from house-distilled water purified by a Hydro Service and Supplies system.

3.3.2 Methods

3.3.2.1 Preparation of Benzoquinone Circular Disks and Irregularly Shaped Particles

BQ powder was finely ground in a mortar and then molded into a pellet (either 3 mm diameter, 1 mm thick or a 13 mm diameter, 1 mm thick) using a die set and either a hand press (Pike Technology, Model No. 161-1100) or a hydraulic press (Carver Inc., Model No. 4350L). Two distinctive particle classifications were implemented for this comparison study. In particular, circular 3 mm BQ disks or irregular shaped and sized BQ fragments. These irregular BQ particles were easily prepared by breaking 13 mm BQ disks into pieces. Specifically, the 13 mm disks were employed due to being highly compressed, as 21,500 PSI was exerted on the specimen from a high-pressure hydraulic press. While the 13 mm BQ disks are very compact, these irregular fragments now have exposed defects; therefore, these pieces were lightly dusted with lycopodium powder. This minor processing step was completed to simply extend the observation time of the self-motion.

3.3.2.2 Protocol and Evaluation Process for Self-Motion at the Air-Water Interface

Aqueous 100 mM NaCl was poured into a surfactant-free glass petri dish (90 mm diameter, 25 mL volume), as any residual surfactant content was proven to inhibit particle motion; thus, surfactants usage in glassware should be avoided. After ensuring system was surfactant-free, disks or irregular shaped BQ fragments were added gently to the air-water interface and locomotion commenced. Motion of BQ disks or fragments was monitored with a digital camera (JVC-HD GZ-E200BU, frame rate: 30 frames per second (fps)). Observations were made until the BQ disks or pieces dissolved or sank. Video analysis was completed on a personal computer using image analysis software (ImageJ 1.41, National Institute of Health,

USA). More specifically, individual [x,y] coordinates for each disk or irregular fragment was manually acquired in ImageJ using the MTrackJ plugin, which facilitates tracking of moving objects in stacked image sequences. The corresponding [x,y] coordinates were then statistically analyzed in R, which is a programming language and statistical computing software.

3.3.2.3 Experimental Procedure and Conditions for Thermotaxis

Primitive forms of taxis were demonstrated by the presences of a temperature probe. For high temperature gradients, a copper wire was attached to a soldering iron and once flocking locomotion was established, the end of the copper wire not directly attached to the soldering iron was positioned at the air-water interface opposite the flock structure. For cooler temperature gradients, a cold metal probe was submerged in ice for 10 minutes and then was arranged at the air-water interface as aforementioned. For each circumstance, particle movement was monitored with a digital camera as well as a thermal infrared (IR) imaging camera (FLIR Instruments, Model No. A655sc). The thermal IR FLIR camera and ResearchIR 4.0 software application permitted advanced thermal pattern analysis.

3.3.2.4 Investigational Process and Experimental Conditions for Magnetotaxis

Fundamental sensing studies were completed with both BQ irregular fragments (non-sensor element) and BQ-iron oxide nanopowder irregular fragments (sensor element). More specifically, the sensor elements were composed by finely grinding BQ (~0.150 g) and iron oxide nanopowder (~0.030 g) together in a mortar and then the combined material was molded into pellet and fragmented as mentioned previously. To perform the sensing experiment, first, a sensor element was added to the air-water interface and a magnetic bar was held atop, while the height was optimized until there was no effect on the sensor fragment. This threshold height was

dependent upon the specific irregular piece employed in the system; therefore, was optimized per experiment. Subsequently, the magnet was removed from atop and non-sensor elements were added to the air-water interface and allowed to interact with the sensor element. Once a transient flock was formed, the magnet was positioned atop and opposite the flock and locomotion was monitored.

3.3.2.5 Assessment Practice for Determining the Rate of Entropy Production

UV-Visible spectroscopy (HP/Aligent 8453) was employed to measure the rate of BQ dissolution for each particle series. More specifically, in order to compare particle shape for a specific particle number, the mass remained constant. Then solution was obtained from identical locations within the glass petri dish and absorbance was monitored every 10 s throughout BQ particle locomotion. Absorbance was measured over a 7 min period, in which, BQ fragments were dissolving, had been dissolved or sank. Concentrations of BQ were assessed using a standard calibration curve and the rate of dissolution was estimated by utilizing a known solubility value (10 g L^{-1}) for BQ at 25°C. Furthermore, similar concentration values tabulated were prepared, specifically, aqueous solutions of 0 to 100 mM BQ, and corresponding surface tension measurements were performed. Surface tension was measured by the standard Wilhelmy method using a surface tensiometer (EZ-Pi^{plus}, Kibron).

3.4 Results

3.4.1 Flock Structure Formation

Multiple irregularly shaped BQ, in which N = 4, 6, 8, 10, 12, or 15, fragments in a single petri, each being broadly different in both size and shape per experiment, were carefully added onto the aqueous phase and instant self-motion of each particle emerged at the air-water

interface. Detailed descriptions of the emergent dynamic behavior follow. Comparison studies were completed with circular 3 mm BQ disks. Supplementary videos clips, mentioned at specific points in the text below, were used to illustrate main data described herein. Additionally, resultant motions witnessed were observed until the particle/s sank or completely dissolved.

Following previously reported primitive *flocking* involving irregularly shaped particles, additional studies with these irregularly shaped BQ pieces were completed. Irregularly shaped BQ fragments were prepared as described above. Initially, these fragments were spread across the air-water interface; immediate locomotion freely around the interface transpired. However, over varying periods of time, multiple particle assembly emerged and transient flocking was observed, as illustrated by **Video S3.1** (please view ESI file to observe this phenomenon). More specifically, as shown by the example in **Figure 3.1**, the particles were first dispersed across the entire air-water interface (**Figure 3.1A**) and instantaneous self-motion, both translation and rotational, occurred for each individual particle. The BQ particles interacted over time with one another by formation of multiple small group collectives, as seen in **Figure 3.1A and B**. Ultimately, these small fluently voyaging cooperative groups interacted and organized into a larger flock (**Figure 3.1D**). However, as seen in **Video S3.1** (ESI) and **Figure 3.1E, F and G**, these self-organized flocks were dynamic; consequently due to fragments of BQ constantly and fluently associating and disassociating from the collective, the area occupied by an identified flock changes, increasing as the members of the flock drift away from the flock and decreasing as they return to the flock.

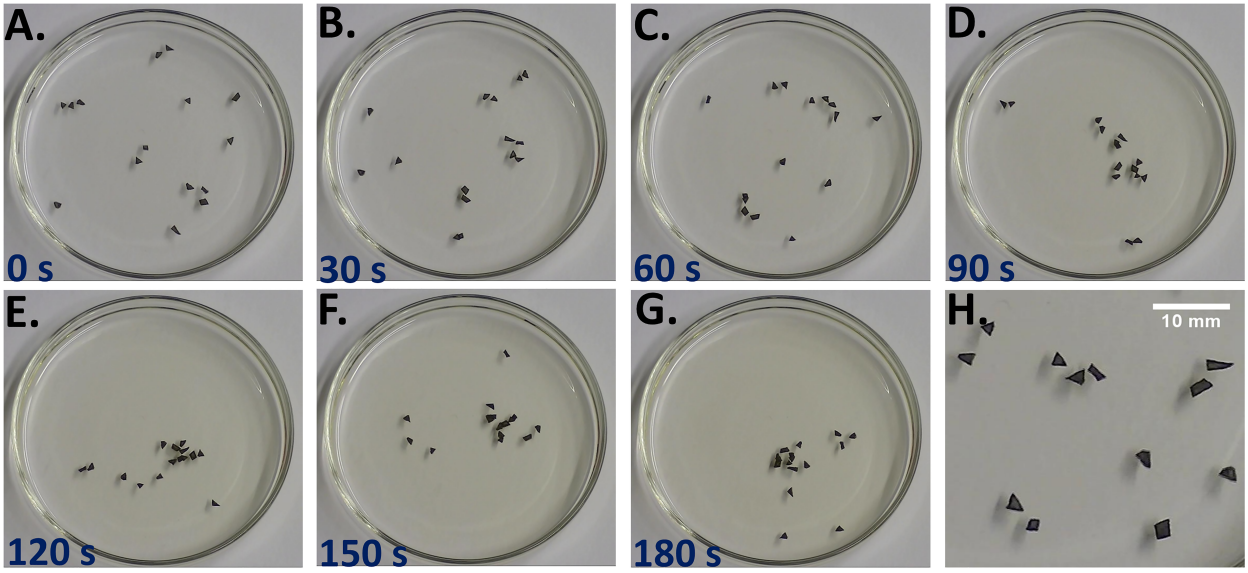

Figure 3.1: Illustration of collective, flocking structure formation among 15 irregularly shaped BQ particles at 30 s time intervals. Please view **Video S1** (ESI).

3.4.2 Thermotaxis of the Flock

3.4.2.1 Warmer Temperature Conditions

The dynamic self-organized, transient flock exhibited primitive forms of taxis. We generated thermotaxis conditions (both warm and cold), which demonstrated that our system, like biological systems, responded to changes to the environment. Specifically, either a cold or hot probe was positioned at the aqueous interface, which created a small temperature gradient zone within the petri dish; these temperature gradients were measured with an infrared camera. The presence of warmer or colder conditions affected the directional behavior of the dynamic flock. In particular, snapshots seen in **Figure 3.2** and **Video S3.2** (Please notice this phenomenon in ESI), revealed in the occurrence of a warmer temperature gradient, the flock migrated toward warmer conditions. More precisely, of the total 15 BQ fragments a flock of size N = 10 was collectively moving (**Figure 3.2A**) and its motion occurred at ambient conditions of 22°C

(**Figure 3.2B**). However, when a hot temperature probe was placed at the interface at a distance away from the flock (**Figure 3.2C**), the flock and other BQ fragments migrated in the direction of the hot probe. The temperature probe, **Figure 3.2D**, created a hot spot (d = 2 mm) at ~ 40°C and surrounding zone (d = 9 mm) ranging from ~ 26 to 30°C. Eventually, 13 out of 15 BQ fragments hovered at the temperature probe, more specifically; the particles remained in the warmer region zone ranging from ~ 27 to 32°C (**Figure 3.2E and F**).

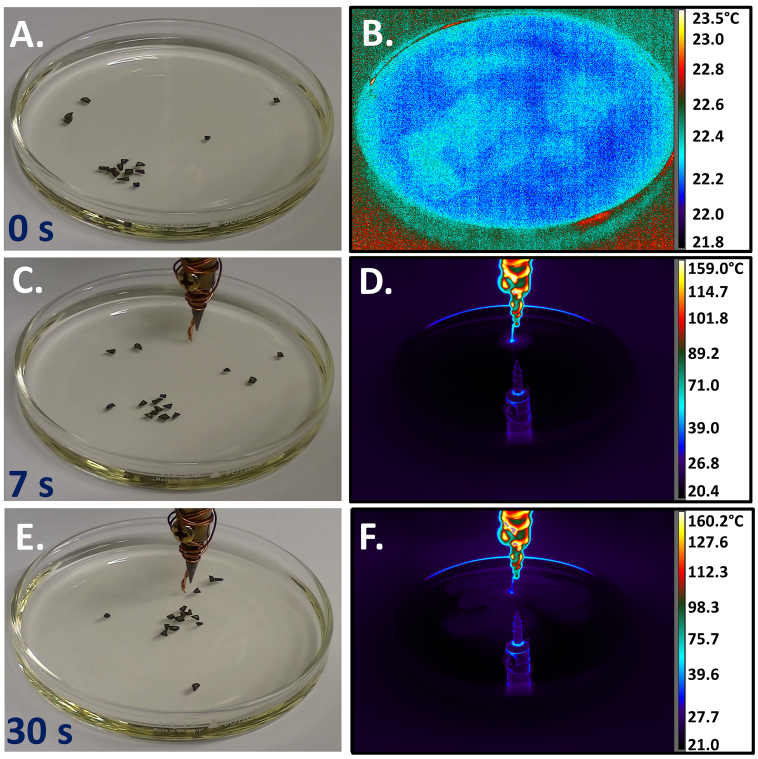

Figure 3.2: Snapshots at different time intervals and the corresponding temperature gradient for 15 irregularly shaped BQ particles under warm thermotaxis conditions. A) Particle addition to the surface lead to flock formation B) under ambient conditions, then C) after 7 s of self-motion the in-house temperature probe was added to the interface and the assembly began to migrate to the D) warmer conditions seen by the small purple and blue diameter circle, and then E) at 30 s a majority of the particles were hovered and continued to voyage around F) the warmer temperature zone seen by larger purple diameter. Please view **Video S3.2** (ESI).

3.4.2.2 Cooler Temperature Conditions

Contrasting behavior was observed under cooler temperature conditions. More specifically, the flocking collective moved away from cooler regions, opposite of what was witnessed in the aforementioned experiment. In particular, snapshots seen in **Figure 3.3** and **Video S3.3** (Please see video in ESI), revealed in the occurrence of a cooler temperature gradient, the flock drifted away from cooler conditions generated and rather migrated to warmer regions within the petri dish. More precisely, small group collectives (two N= 7 out 15) were cooperatively moving (**Figure 3.3A**) and their motion occurred at ambient conditions of 22°C (**Figure 3.3B**). Consequently, when a cold-finger probe was placed at the interface very near the flock structure (**Figure 3.3C**), BQ fragments immediately began to migrate away from the probe. The temperature probe, **Figure 3.3C**, created a cool spot (d = 3 mm) at ~ 13°C and surrounding zone (d = 5 mm) ranging from ~ 18 to 20°C. At 25 s, the particles (N = 11 of 15) still remained distant from the cool region (**Figure 3.3E and F**) as long as the temperature of the probe remained low.

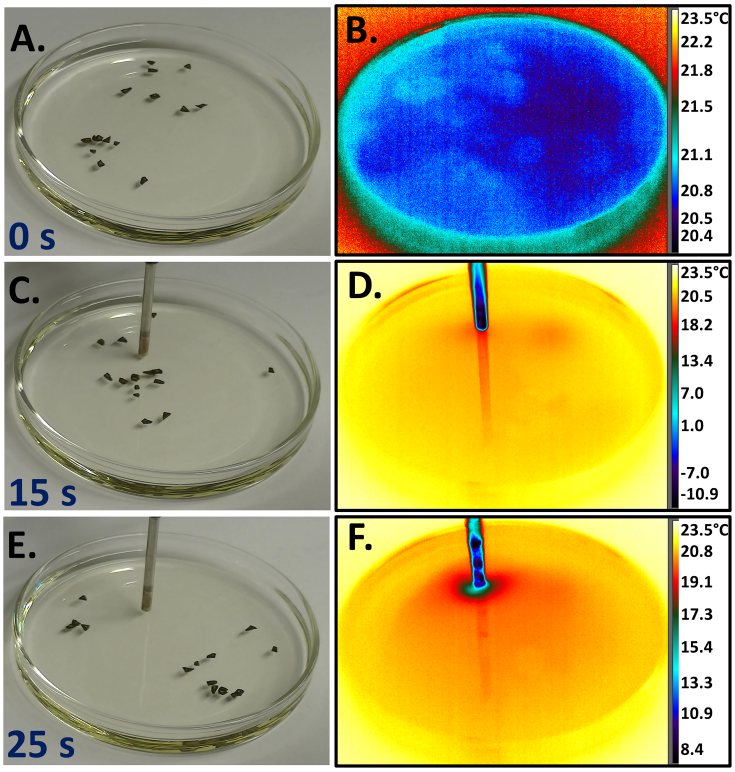

Figure 3.3: Snapshots at different time intervals and the corresponding temperature gradient for 15 irregularly shaped BQ particles under cold thermotaxis conditions. A) Particle addition to the surface lead to grouped collections B) under ambient conditions, then C) after 15 s of self-motion the in-house cold probe was added to the interface and the assembly migrated in the opposite direction of the D) cooler conditions seen by small red zone, and then E) at 25 s a majority of the particles continued voyaging distant the probe F) the cooler temperature zone seen by larger dark green and red diameter region. Please view the **Video S3.3** (ESI).

3.4.3. Magnetotaxis and Control of the Flock

3.4.3.1 Magnetotaxis of the Flock Structure

These BQ flocks of irregular fragments exhibit remarkable cohesiveness. One way this could be demonstrated is by making one of the fragments magnetic. By making one of the fragments magnetic, it was possible to make the entire flock sense and drift toward a magnetic

field. Such a collective property, of sensing a physical variable and moving toward a region as a response, is typical in biological systems. To study this aspect of the system, we designed a "proto-sensor" system. Our proto-sensor system was comprised of two types of elements, sensor and non-sensor elements. A sensor element was a single BQ-iron oxide particle and non-sensor elements were BQ fragments, each was prepared as described above. Iron (II, III) oxide nanopowder was implemented herein due to the attraction to a magnetic field. To begin, first, the sensor element was carefully placed on the aqueous interface. Then a magnet, held atop of the glass petri dish, was positioned at a specific height where the sensor element was free enough to move and become a part of the flock and not frozen by the force of the magnetic field, as shown in **Video S3.4** (ESI). The position of the magnet was such that the sensor was actually capable of self-motion throughout the entire petri dish, but only showed a tendency to be in the vicinity of the field, that is its self-motion had enough kinetic energy to overcome the magnetic potential energy well. The threshold height was checked and corrected for each experiment due to the variation in particle shape and size. Once the threshold height was determined, the magnet was removed, and the non-sensor fragment elements were added to the interface, **Figure 3.4A**. Cooperative, transient flocking occurred between both sensor and non-sensor elements (**Figure 3.4A**, flock size N = 12 out of 15) and then the magnet was placed away from the self-organized flock structure, as shown in **Figure 3.4B**. Over time, **Figure 3.4C and D**, the flock, including the sensor element "sensed" the magnetic field, though the sensor element by itself was unrestrained by the magnet. A majority of the elements (N > 11) maintained fluent flocking behavior beneath the magnet, as demonstrated in **Figure 3.4E and F** and **Video S3.5** (Please view sensing event in the ESI).

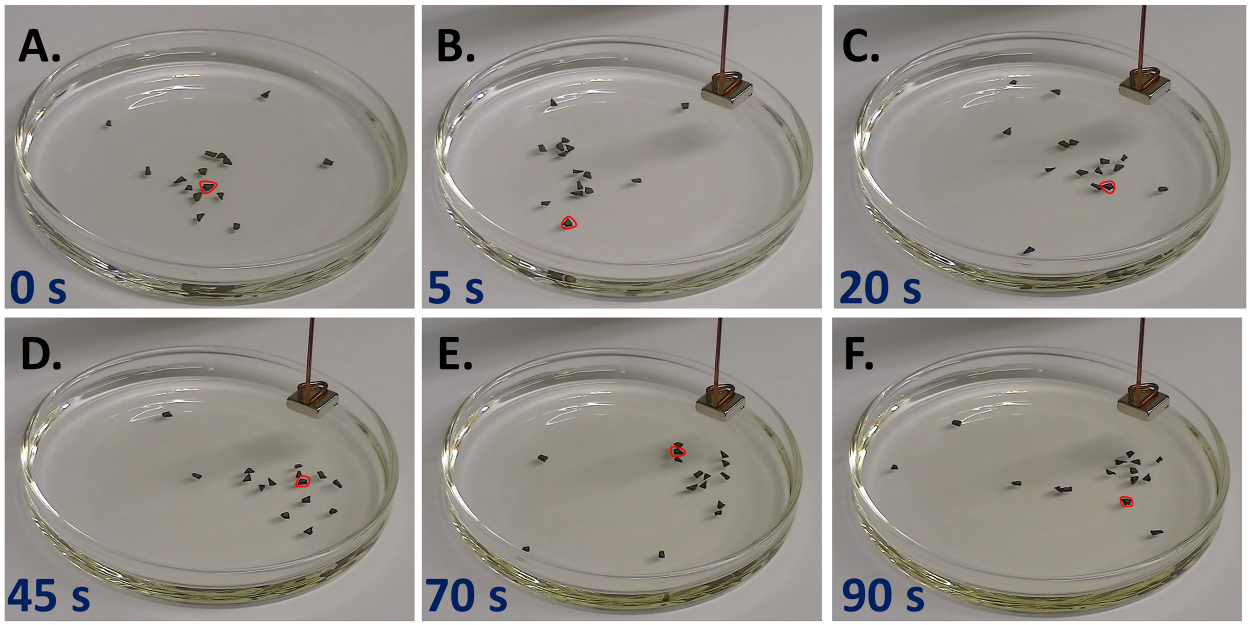

Figure 3.4: Illustration of a BQ flocking collective, constructed of a single sensor element (circled in red) and 14 non-sensor elements, sensing the addition of a magnetic field. See **Video S3.5** (ESI).

3.4.3.2 Evaluation of the Magnetotaxis with Control Experiments

This remarkable phenomenon was further evaluated by performance of control experiments to validate sensing of the magnetic field was reliant on the transient flock formation with both sensor and non-sensor components. First, as shown by an example in **Figure 3.5** and **Video S3.6** (Please view control result in ESI), 15 BQ non-sensor elements were placed on the air-water interface and self-organized collective motion was achieved, then as described above, the magnet was positioned away from the center of flock (**Figure 3.5B**). However, in the absence of a sensor element, these active BQ particles were incapable of sensing the magnetic field over time, as illustrated in **Figure 3.5C-F**. These experiments suggested that while transient flocking was existent, sensing required the combination of both components.

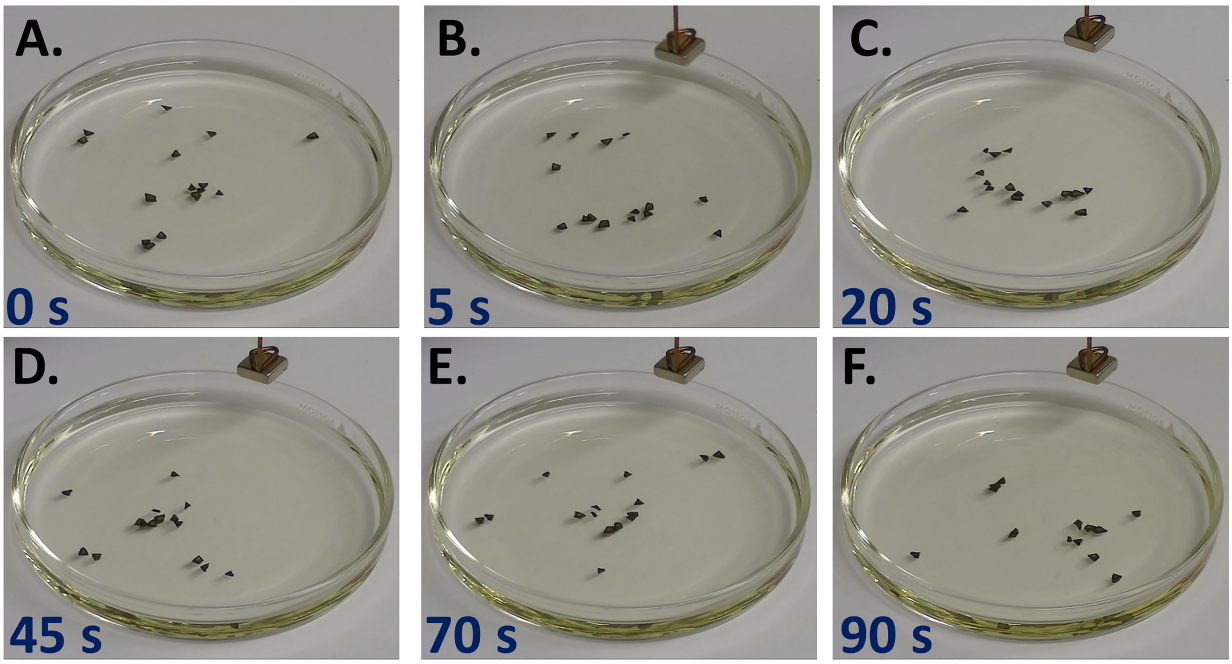

Figure 3.5: Snapshots of a BQ flocking collective, constructed from 15 non-sensor elements. The flocking structure was incapable of sensing the addition of a magnetic field due to the absence of the sensing BQ-iron oxide element. See **Video S3.6** (ESI).

A second control experiment was executed by employing circular BQ disks, as shown by an example in **Figure 3.6** and **Video S3.7** (Please see control experiment in ESI), to demonstrate sensing was dependent on the presence of both dynamic flock formation and sensor element. A single BQ-iron oxide 3 mm sensor disk and 14 non-sensor BQ 3 mm disk elements were employed at the air-water interface. As mentioned afore, the single BQ-iron oxide sensor disk was placed on the interface. Then a magnet, held atop of the glass petri dish, was positioned at a specific height where the sensor element was unaffected by the magnetic field (**Video S3.8**). After threshold height was determined, the magnet was removed from atop, and non-sensor disk elements were placed onto the interface, **Figure 3.6A**. Although collective, dynamic flocking, as will be described below, was not achieved in this scenario, the magnet was positioned above the self-moving active particles (**Figure 3.6B**). Though a sensor element was present in the system,

active BQ particles were incapable of sensing the magnetic field over time, as illustrated in **Figure 3.6C-F**. In particular, this experiment suggested that while a sensor element was present, the absence of transient flocking meant the system was unable to strongly sensing the secondary field.

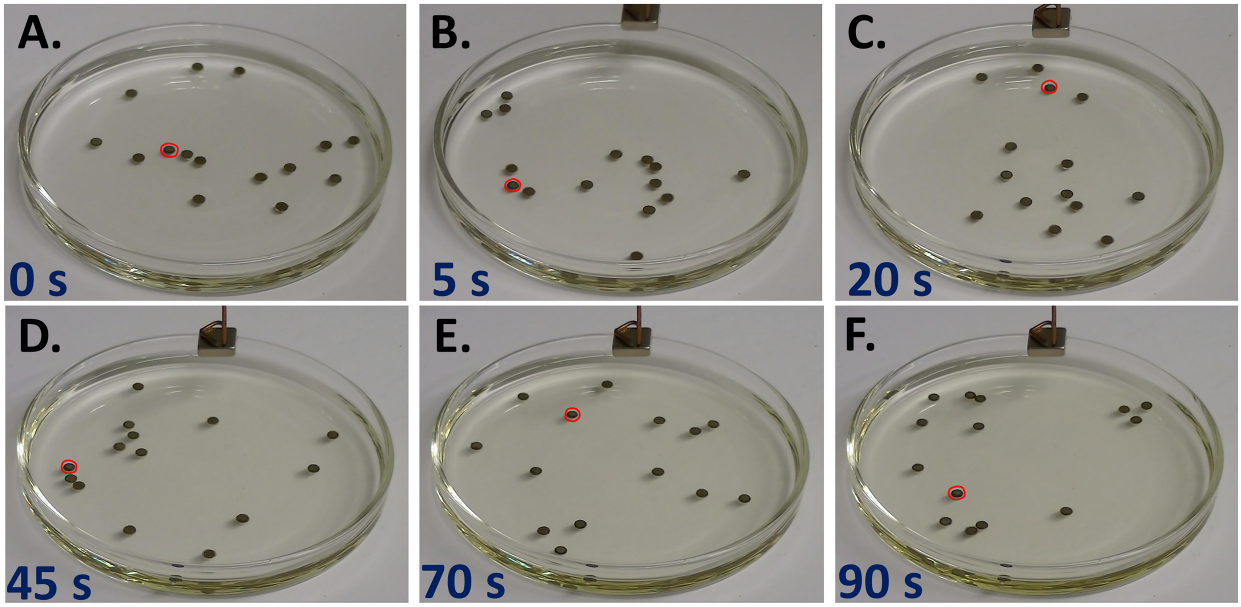

Figure 3.6: Snapshots of 1 sensor BQ-iron oxide 3 mm disk (circled in red) and 14 self-moving 3 mm BQ circular non-sensor disk elements at the interface, which were incapable of flock formation and sensing the addition of a magnetic field. See **Video S3.7** (ESI).

3.4.4 Statistical Analysis on a Flock

This notable flocking behavior was a characteristic collective motion observed only between irregularly shaped BQ fragments. Circular 3 mm disk were studied as well; however, collective flocking was not distinctively observed in these systems. Since particle shape affected whether the overall cooperative flocking motion was observed, it was important to delineate this evolving behavior. Therefore, to demonstrate the emergence of collective group motion observed with non-engineered, irregularly shaped BQ fragments, [x, y] trajectories were acquired for each

individual particle per BQ piece (N) series. These time-resolved 2D trajectory paths traced, **Figure 3.7**, graphically illustrated individual particle motion within the glass petri dish. As observed in **Figure 3.7**, independent particle traces were designated by a different color; additionally, these trajectories revealed rudimentary collective locomotion between particles existed by the closeness of their trace to another, as exemplified in **Figure 3.7B-C**. Since, however, these time-resolved 2D traced trajectories become quite complex (**Figure 3.7D-F**) due to overlapping with increased particle number, statistical modeling will be employed in the future to provide an enhanced definition of flocking behavior and underlying thermodynamic principles perceived herein.

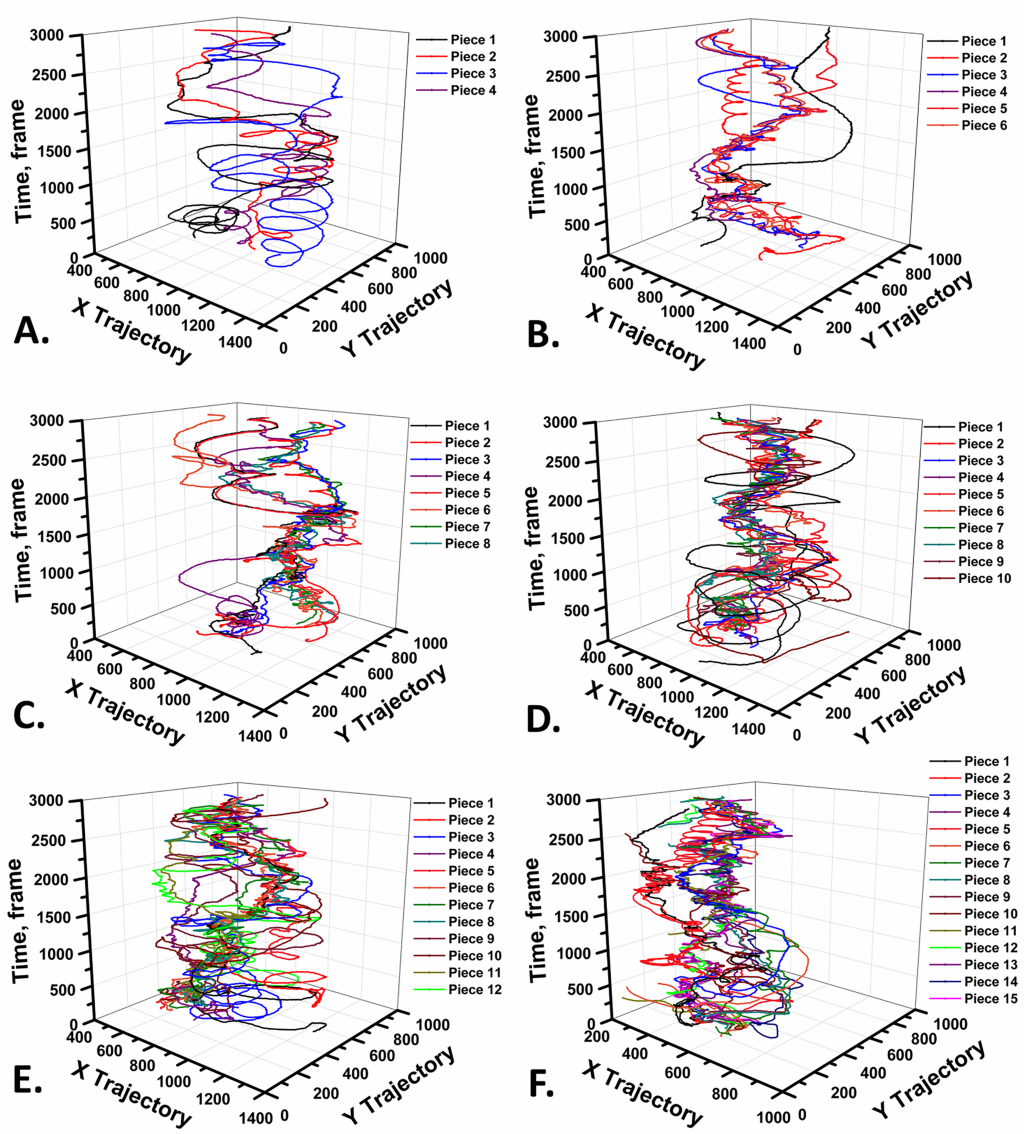

Figure 3.7: Trajectory traces of the irregularly shaped BQ fragments at the air-water interface for particle series A) four, B) six, C) eight, D) ten, E) twelve, and F) fifteen.

3.5 Discussion

Our system of active matter of BQ particles is fundamentally driven by the Gibbs energy of conversion of solid BQ phase to solution phase and, to a small and negligible extent, vapor phase. The transformation first generates a surface tension gradient, which in turn, generates Marangoni convection currents that result in a complex motion of interacting BQ particles. The

forces of the surface tension gradient are in the direction of higher surface tension, which is in the direction of lower concentration, because as shown in **Figure 3.8**, surface tension decreases with increasing concentration of BQ. In the case of active matter camphor infused gels, Soh el al. found that generally the Marangoni convection currents result in repulsive forces between the particles.[41] But this is not universally so: when the depth of the solution is small, in the range of 1.4 – 1.8 mm, the hydrodynamic and surface tension forces were repulsive when the particles were close but attractive when they were farther away, somewhat like intermolecular forces.[43] Soh et al. showed that, as a result of such forces, the camphor induced gel particles formed stable lattices of different geometries. The hydrodynamic origin of these forces was analyzed by numerically integrating Navier-Stokes equation. These studies show that hydrodynamic-surface tension forces can result in both attractive and repulsive forces between chemically driven active matter particles. The theoretical analysis was completed for rectangular particles. However, as is in the general case with hydrodynamic forces, for irregularly shaped particles, the hydrodynamic and surface tension forces can be expected to be highly complex, dependent on the particular shapes of the particles, making it practically impossible to obtain detailed hydrodynamic description of the system.

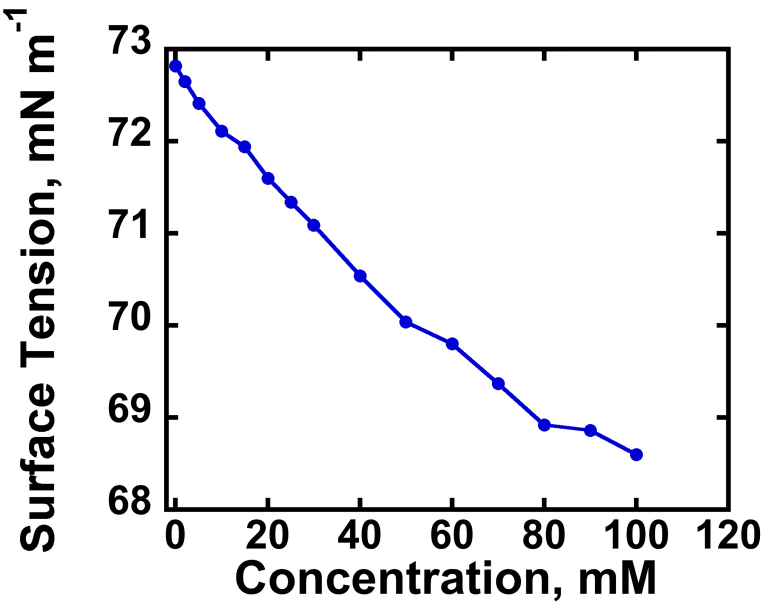

Figure 3.8: Surface tension measurements at different concentrations of aqueous 100 mM solutions of BQ.

In our study, multiple BQ particles at the air-water interface demonstrated continuous, spontaneous motion across the interface, due to attractive and repulsive interparticle interactions, in addition to their inherent capability to self-propel. When the particles had high symmetric circular shape, they in general exhibited attractive forces at some distance but repelled when close (noted as collisions previously); for systems of circular disks, there was no easily observable cooperative behavior. In a system consisting of irregularly shaped particles, remarkably, flocking behavior emerged and, as described below, these flocks demonstrated thermotaxis and the flock as a whole became a magnetic field-sensing flock when a single particle contained iron-oxide nanoparticles.

3.5.1 Flock Formation

Alongside continuous motion, the most attractive phenomenon was the spontaneous development of group collective motion, we termed *flocking*. It was observed largely from

asymmetrical BQ fragments, but did not explicitly appear in symmetrical circular BQ disks; the circular BQ particles moved about freely, encountering each other and moving on without any visible aggregation. The interesting flocking behavior, as seen in **Figure 3.1** and **Video S3.1** (ESI), developed over a short time and was observed to be quite dynamic over the remaining experimental run. Initially, these BQ fragments move indiscriminately around the petri dish; however, complexity and cooperativity begins to emerge between multiple small collectives that is entirely different from random motion. In most experimental cases herein, the multiple collectives blend to form a single transient, self-organized flock structure. Since this structure is maintained by continuous dissipation of Gibbs energy, it is a dissipative structure. The flock is dynamic, and BQ particles are associating and disassociating with the dissipative structure; furthermore, this structure is coexistent with particles in random motion that are not in the main fraction flocking.

We propose that numerous irregularly shaped BQ particles have stronger interparticle hydrodynamic interactions that permit them to cooperatively self-propel as a flock collective, because this dynamic behavior was not strongly observed in the presence of multiple circular BQ disks. In both shape cases, surface tension and concentration gradients are heterogeneous as are Marangoni convection flows. However, we suspect, that irregular BQ fragments have greater interfacial difference near particle points and edges; thus, driving each particle to cooperatively interact with one another. This conclusion was drawn, as the symmetric disks demonstrated more attractive and repulsive interactions previously reported as collisions. Nevertheless, statistical analysis was completed utilizing [x,y] coordinates to provide an additional explanation on the remarkable emergence of cooperative flock formation and will be described below.

3.5.2 Thermotaxis of the Flock

A characteristic locomotive feature of living systems is their ability to sense the environment in which they reside and respond to it.[45] This is called taxis. More precisely, taxis is the movement of an organism triggered by a stimulus to the environment, such as the presence of food, light, chemicals, temperature, and etc. The response is an intrinsic behavioral reaction and the movement can be toward or away from the external stimulus.[45] Thus, taxis encompasses two major factors: application of external stimulus and the response of the organism to this signal. Furthermore, the corresponding response also involves two major steps, which is first, the detection of the signal and then transduction of the external stimulus into an internal signal that triggers a response.[45] Hence, it is essential that newly constructed non-living self-propelled systems, that desire to mimic living systems, demonstrate enhanced sensory response to external stimuli.

There are several examples of inanimate systems exhibiting primitive forms of taxis. For example, self-propelled objects like camphor and camphoric acid boats, have shown chemotaxis by characteristically accelerating and decelerating with the addition of chemical stimuli.[46, 47] Furthermore, engineered gel infused camphor assemblies displayed forms of taxis to both solution depth and temperature gradients.[43] Therefore, not unexpectedly, our BQ dynamic flock structure likewise exhibited crude forms of taxis. While, solution depth did not seem to exhibit changes in the behavior of the flock, two thermotaxis conditions, warm (**Figure 3.2**) and cool (**Figure 3.3**), were applied to the system and response to theses stimuli were observed. Please review **Video S3.2** and **S3.3** (ESI), as these recordings reveal the dynamic flock reaction to warm and cool thermotaxis respectively.

A warm external stimulus, created by an in-house temperature probe, was applied to the air-water interface distant from the self-moving flock. This warm probe produced a hot spot and warm surrounding region (**Figure 3.2D** and **F**) as described above. The presence of this warm temperature gradient was then transduced via convection currents, an effect of self-propulsion, which then, in turn, triggered the dissipative flock structure to perceive and react to change to its environment. While, in general, surface tension decreases with increased temperature, our case is more complex than general solution circumstances. Inherently, our system already has interfacial heterogeneity present due to self-motion of particles on the surface and is thereby different. Consequently, addition of the hot probe thus increased the temperature at the air-water interface, which then caused surface BQ molecules to evaporate, to a small extent. This process decreased the BQ concentration within the region, hence increasing the surface tension. Therefore, as a response to the applied stimulus, the flock structure moved and hovered in the warmer region, as observed in **Video S3.2** (Please see recording in ESI file).

In contrast, a cool external stimulus, created by a cool metal probe, was positioned on the air-water interface nearest as possible to the flock. Addition of the probe created a cool spot and surrounding region that was cooler (**Figure 3.3D** and **F**) as described afore. Like the warm thermotaxis condition, the cool gradient was then transduced via convection currents, which triggered the dissipative flock to detect and then respond to the modification of its environment. In this case, the existence of a cool temperature gradient prompted the dissipative flock to move away from and remain distant in the warmer regions, as seen in **Video S3** (Please view recording in ESI file). Overall, both applied thermotaxis conditions, demonstrate our system has the capability to detect and respond to fluctuations in the surrounding medium.

3.5.3 Magnetic Sensing by the Flock

After our system exhibited primitive forms of taxis; we investigated further the capability of our cohesive flock structure to act as a physical self-serving system. To be self-served, the needed energy (and/or matter) is obtained by the system from its environment; therefore, the system forages for energy sources and termed here as a "proto-sensor" system. Our simple system has energy that can be used to seek further energy resources and through minimal changes demonstrated the capability of detecting information concerning a new energy source, and reacting to that information by cohesively moving to obtain it.

The dissipative structure described up until now was composed of one element, specifically, irregularly shaped BQ particles. To maintain simplicity, our proto-sensor system was designed with merely two elements: a single sensor (BQ-iron oxide nanopowder) and multiple non-sensors (BQ). Both elements should be responsive to the primary interfacial tension field, meaning both elements should be involved in the flock structure. However, only the BQ-iron oxide sensor element should be responsive to the secondary magnetic field. If the system is indeed self-served, the presence of the secondary magnetic field should affect the behavior of the sensor element, then since the energy flow that maintains the structure couples the two elements, the behavior of the non-sensor element should become affected, and thus the entire dissipative structure.

When both sensor and non-sensor irregularly shaped elements were placed on the interface, over a short time, the usual collective flocking behavior was observed (**Figure 3.4A**). Subsequent application of the secondary magnetic field attracted the BQ-iron oxide sensor element; in consequence, the BQ non-sensor fragments were also attracted due to energy from within the primary field, as witnessed in **Figure 3.4B-F** and **Video S3.5** (ESI). This remarkable

sensing phenomenon was validated with two control experiments. First, all non-sensor BQ irregularly shaped elements were positioned on the interface and allowed to flock, but the sensor element was absent. Thus, upon application of the secondary field, the lack of the sensor element meant the dissipative flock was incapable of detecting the secondary field, as coupled energy flows did not arise (**Figure 3.5** and **Video S3.6** (ESI)). Secondly, symmetric sensor and non-sensor BQ elements were employed; however, in this case, coupled energy was not induced, as a dissipative flock was not inherently formed, thus the secondary field was not detected (**Figure 3.6** and **Video S3.7** (ESI)).

3.5.4 Rate of Entropy Production of the Flock

Thermodynamics provides another level of description. One variable of interest in self-organizing dissipative structures is the rate of entropy production. In many cases, the rate of entropy production increases when a dissipative structure is formed. There are examples of systems, in which, the system evolves to states associated with higher entropy production.[15] In the case of active matter of BQ pellets, the rate of entropy production is proportional to the rate of Gibbs energy dissipation. The motion of the particles increases the rate of Gibbs energy dissipation because the surface tension gradient moves the fragments to regions of lower concentration and increases the rate of dissolution. It is then natural to wonder if the formation of the flock and the motion of the flock is yet another way the system increases dissipation and thus the rate of entropy production. In other words, the question is whether the rate of dissolution of a BQ system consisting of a flock is higher when compared to a system that does not exhibit flocking behavior.

In order to measure the rate of dissipation, the rate at which the concentration of the solution phase is increasing is to be measured. For our system, the concentration of BQ may be

measured by noting the UV absorption. Thus, solution samples were taken at various times and their UV absorption was measured, which means, time variation of the concentration was obtained. Measurements were evaluated for both circular disks and irregularly shaped particles, which exhibited negligible collective behavior and strong cooperative flocking behavior respectively.

As noted above, change in the Gibbs free energy of a chemical transformation drives the motion of active-matter particles such as BQ and camphor. In the case of BQ particles, the transformation is from the initial solid phase, BQ (s), to the final solution phase, BQ (aq). Including the conversion to the vapor phase BQ (g) we have these reactions:

$$\text{BQ (s)} \rightarrow \text{BQ (aq)} \qquad \textbf{Equation (3.1)}$$
$$\text{BQ (s)} \rightarrow \text{BQ (g)} \qquad \textbf{Equation (3.2)}$$

The fraction of BQ transforming into the vapor phase is very small, and could be neglected for quantitative calculations, but we include it here for theoretical completeness. Initially the solid phase dissolves and spreads on the liquid surface and decreases the surface tension. For a solution of BQ, the surface tension decreases with increasing concentration, form about 72.82 nN m^{-1} at zero concentration to nearly 68.60 mN m^{-1} at 100mM (**Figure 3.8**). Since the decrease in the surface tension is not uniform and isotropic, surface tension gradients are generated. These gradients move the particles towards regions of higher surface tension or lower concentration.[31] Thus, a complex of dynamics of particle dissolution, surface tension variation, and particle motion are initiated. The dynamics moves the particles to regions of lower concentrations and thus speeds up the process of dissolution.

If we denote the corresponding chemical potential of the three phases by μ_s, μ_{aq}, and μ_g respectively, then the affinity, A, the driving thermodynamic force for this reaction is:

$A = \mu_s - \mu_{aq}$ **Equation (3.3)**

$A' = \mu_s - \mu_g$ **Equation (3.4)**

Furthermore, if $d\xi_{aq}$ and $d\xi_g$ are the molar amounts of BQ converted from the solid phase to the aqueous phase and the gas phase in time dt, respectively, the total rate of entropy production for the process is:

$$\frac{dS}{dt} = A\frac{d\xi_{aq}}{dt} + A'\frac{d\xi_s}{dt} \qquad \textbf{Equation (3.5)}$$

In practice it is found that $d\xi_g/dt$ is very small and the amount of solid converted to the gas phase is virtually zero on the time scale of the experiment. Hence we ignore it and measure the total entropy production in terms of the conversion to the aqueous phase. It is interesting that the motion generated by the surface tension gradients increases $d\xi_{aq}/dt$ and hence the rate of entropy production. These entropy-generating processes not only generate self-motion, but also produce self-organized motion that we see by the flocking behavior of irregularly shaped fragments. As noted above, if the flocking behavior is not observed in circular pellets, it raises the question if the flocking behavior, in fact, increases the rate of entropy production as self-organization generally does in non-equilibrium systems. If indeed this is true, then it means the system that exhibits flocking behavior has a higher rate of dissolution. In terms of the concentration C(t) of the BQ solution, it would mean that C(t) would increase faster for the systems that demonstrates flocking behavior. Neglecting the conversion to the gas phase, we write the rate of entropy production as:

$$\frac{dS}{dt} = AV\frac{dC}{dt} \qquad \textbf{Equation (3.6)}$$

If C_0 is the concentration at saturation and C(t) is the concentration at any time, t, the rate of increase in the concentration is then proportional to the difference ($C_0 - C(t)$). Thus:

$$\frac{dC(t)}{dt} = k(C_0 - C(t)) \qquad \textbf{Equation (3.7)}$$

in which the rate constant k depends on surface area of the solid phase BQ pellets and other factors such as fluid convection around the solid phase, etc. With this kinetic law, the entropy production

$$\frac{dS}{dt} = AVk(C_0 - C) \qquad \textbf{Equation (3.8)}$$

For flocking, we expect k to be higher then it is for non-flocking behavior. The solution to equation **(8)** is:

$$C(t) = C_0 (1 - e^{-kt}) \qquad \textbf{Equation (3.9)}$$

By plotting $\ln(C_0 - C)$ vs t, k can be determined. To see if there is any strong indication that k is different between flocking and non-flocking behavior, time variant UV absorbance measurements were acquired to evaluate the multiple particle systems (N =4, 6, 8, 10, 12, and 15) for both circular and irregular shaped particle circumstances. The experiment conducted was described in detail above. For each case, by plotting $\ln(C_0 - C)$ vs t (**Figure 3.9**), a decay over time was acquired. From these plots, the value of k, or slope, was computed from the linear curve fitting. As shown in **Figure 3.10**, as the number of particle in a single petri dish increases, the value of k increases as expected. The values of k for irregular particles does not show an unambiguously higher value when compared to those of circular particles, though they are generally a little higher. To see the overall trend, the k values obtained were then plotted against

number of particles. The slopes of these curves (See **Figure 3.10**) show a 12% difference, suggesting that the entropy production may be slightly higher for irregular particles. However, in view of the size of fluctuations in the data, we can only conclude that there is enough reason to study this aspect with a better experimental procedure, which measures the average concentration in the whole system. The limitation of our measurements was that it was the concentration measured at one location in the solution. Though the concentration at one location might reflect the overall trend, its value has larger fluctuations, as can be seen in the above data.

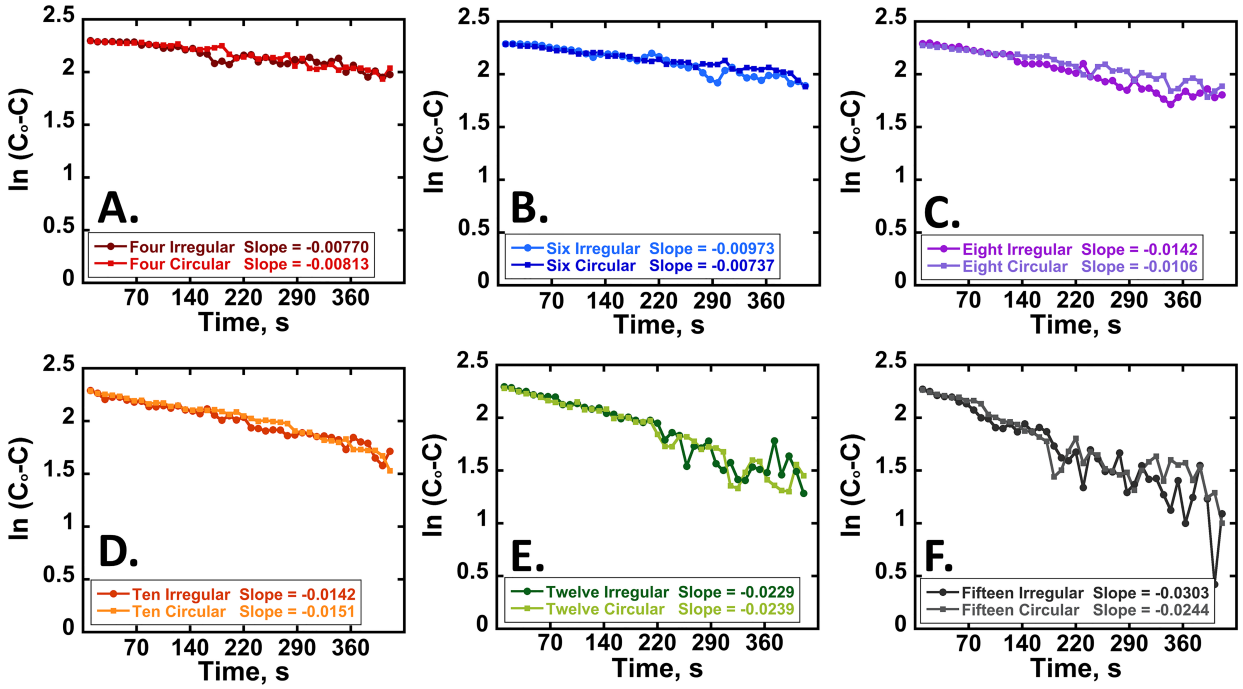

Figure 3.9: Comparison of both particle number and shape when ln(C_o-C) versus time was plotted and tabulated from time variation UV measurement studies.

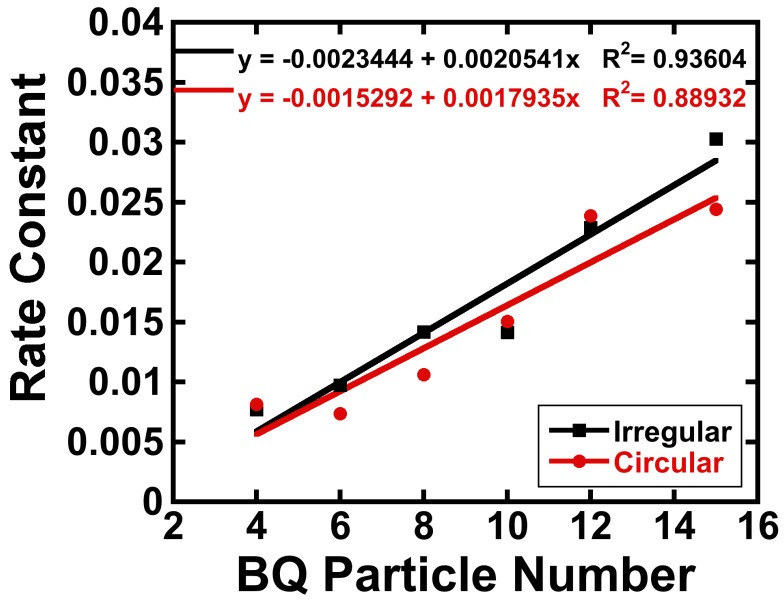

Figure 3.10: Plot of rate constant, extracted from the slopes in **Figure 3.9**, versus the number of BQ particles in the petri dish during time variation UV absorption studies.

3.6 Conclusion

Results described above illustrate a novel multiple particle self-motion system. Spontaneous flock formation emerged between multiple irregularly shaped BQ fragments; however, this flocking behavior was not explicitly observed in the symmetric circular disk shape circumstance. Complex relations between convection flows and inhomogeneous interfacial tension gradients formed as the particles slowly dissolve can explain these characteristic interparticle interactions known as flocking. This flocking dissipative structure demonstrated perception-action capabilities observed by detection and response to both thermotaxis and magnetotaxis scenarios. Primitive studies demonstrated the collective flocking structure was indeed affected by particle shape and statistical modeling validated the ideology. While our current study revealed a 12% increase for flocking structure formation, fluctuations and

complexity both within induced ambiguity in the measurement; therefore, further studies on the underlying thermodynamic rate of entropy production are underway.

3.7 Acknowledgments

This work was financially supported by National Science Foundation's INSPIRE Track 1 Program, Grant No. BCS-1344725. We thank Professors Bruce Kay, Michael Turvey, Claudia Carello, and Jeffrey Kinsella-Shaw (University of Connecticut) for helpful and critical discussions.

3.8 References

1. Zaikin, A. N.; Zhabotinsky, A. M. Concentration Wave Propagation in Two-dimensional Liquid-phase Self-oscillating System. *Nature* **1970***, 225*, 535-537.
2. Nicolis, G.; Prigogine, I. *Self-organization in nonequilibrium systems: From dissipative structures to order through fluctuations*. New York: Wiley,1977.
3. Haken, H. *Springer Series in Synergetics*, Springer-Verlag: Berlin, 1977, Vol. 1.
4. Petrov, V.; Ouyang, Q.; Swinney, H. L. Resonant pattern formation in achemical system. *Nature* **1997***, 388*, 655-657.
5. Vanag, V. K.; Yang, L.; Dolnik, M.; Zhabotinsky, A. M.; Epstein, I. R. Oscillatory cluster patterns in a homogeneous chemical system with global feedback. *Nature* **2000***, 406*, 389-391.
6. Rensing, L.; Jaeger, N. *Temporal order : Proceedings of a Symposium on Oscillations in Heterogeneous Chemical and Biological Systems, University of Bremen, September 17-22, 1984*; Springer-Verlag: Berlin, 1985; Vol 29.
7. Vicsek, T.; Czirok, A.; Ben-Jacob, E.; Cohen, I.; Shochet, O. Novel Type of Phase Transition in a System of Self-Driven Particles. *Phys. Rev. Lett.* **1995***, 75*, 1226-1229.
8. Marchetti, M. C.; Joanny, J. F.; Ramaswamy, S.; Liverpool, T. B.; Prost, J.; Rao, M.; Simha, R. A. Hydrodynamics of soft active matter. *Rev. Mod. Phys.* **2013***, 85*, 1143-1189.
9. De Magistris, G.; Marenduzzo, D. An introduction to the physics of active matter. *Phys. A (Amsterdam, Neth.)* **2015***, 418*, 65-77.
10. Takatori, S. C.; Brady, J. F. Forces, stresses and the (thermo?) dynamics of active matter. *Curr. Opin. Colloid Interface Sci.* **2016***, 21*, 24-33.
11. Kondepudi, D., Prigogine, I. *Modern Thermodynamics, From Heat Engine to Dissipative Structures*, 2nd ed; John Wiley: New York, 2015.
12. Goldbeter, A. *Biochemical Oscillations and Cellular Rhythms: The molecular bases of periodic and chaotic behavior*, Cambridge University Press, 1996.
13. Toussaint, O.; Schneider, E. D. The thermodynamics and evolution of complexity in biological systems. *Comp. Biochem. Physiol., Part A: Mol. Integr. Physiol.* **1998***, 120*, 3-9.
14. Pross, A. The Driving Force for Life's Emergence: Kinetic and Thermodynamic Considerations. *J. Theor. Biol.* **2003***, 220*, 393-406.
15. Kondepudi, D.; Kay, B.; Dixon, J. End-directed evolution and the emergence of energy-seeking behavior in a complex system. *Phys Rev E.* **2015***, 91*, 050902/1 - 050902/5.
16. Dumont, S.; Prakash, M. Emergent mechanics of biological structures. *Mol. Biol. Cell* **2014***, 25*, 3461-3465.
17. Lipowsky, R.; Klumpp, S. 'Life is motion': multiscale motility of molecular motors. *Phys. A (Amsterdam, Neth.)* **2005***, 352*, 53-112.
18. Huxley, H. E. Mechanism of muscular contraction. *Science.* **1969***, 164*, 1356-1366.
19. Wegmann, R. Our Molecular Nature. The Body's Motors, Machines and Messages by D. S. Goodsell. *Cell. Mol. Biol. (Paris)* **1997***, 43*, 254.
20. Hatwalne, Y.; Ramaswamy, S.; Rao, M.; Simha, R. A. Rheology of Active-Particle Suspensions. *Phys. Rev. Lett.* **2004***, 92*, 118101.
21. Lodish, H. *Molecular Cell Biology, 6th Edition;* W. H. Freeman: New York, 2008.
22. Sumpter, D. J. T. *Collective Animal Behavior.* Princeton University Press: Princeton, 2010.
23. Giardina, I. Collective behavior in animal groups: theoretical models and empirical studies. *HFSP Journal* **2008***, 2*, 205-219.

24. Vicsek, T.; Zafeiris, A. Collective motion. *Phys. Rep.* **2012***, 517*, 71-140.
25. Deutsch, A.; Theraulaz, G.; Vicsek, T. Collective motion in biological systems. *Interface Focus* **2012***, 2*, 689-693.
26. Nakata, S.; Iguchi, Y.; Ose, S.; Kuboyama, M.; Ishii, T.; Yoshikawa, K. Self-Rotation of a Camphor Scraping on Water: New Insight into the Old Problem. *Langmuir* **1997***, 13*, 4454-4458.
27. de Gennes, P. G. The dynamics of reactive wetting on solid surfaces. *Physica A (Amsterdam)* **1998***, 249*, 196-205.
28. Sekimoto, K. Langevin equation and thermodynamics. *Prog. Theor. Phys. Suppl.* **1998***, 130*, 17-27.
29. Nakata, S.; Hayashima, Y. Spontaneous dancing of a camphor scraping. *J. Chem. Soc., Faraday Trans.* **1998***, 94*, 3655-3658.
30. Kohira, M. I.; Hayashima, Y.; Nagayama, M.; Nakata, S. Synchronized self-motion of two camphor boats. *Langmuir* **2001***, 17*, 7124-7129.
31. Suematsu, N. J.; Ikura, Y.; Nagayama, M.; Kitahata, H.; Kawagishi, N.; Murakami, M.; Nakata, S. Mode-Switching of the Self-Motion of a Camphor Boat Depending on the Diffusion Distance of Camphor Molecules. *J. Phys. Chem. C* **2010***, 114*, 9876-9882.
32. Suematsu, N. J.; Miyahara, Y.; Matsuda, Y.; Nakata, S. Self-Motion of a Benzoquinone Disk Coupled with a Redox Reaction. *J. Phys. Chem. C* **2010***, 114*, 13340-13343
33. Matsuda, Y.; Suematsu, N. J.; Nakata, S. Photo-sensitive self-motion of a BQ disk. *Phys. Chem. Chem. Phys.* **2012***, 14*, 5988-5991.
34. Nakata, S.; Matsuda, Y.; Ikura, Y. S.; Takeda, A.; Izumi, S. Mode Change in the Self-Motion of a Benzoquinone Disk Coupled with a NADPH System. *Chem. Phys. Chem.* **2012***, 13*, 520-524.
35. Nakata, S.; Arima, Y. Self-motion of a phenanthroline disk on divalent metal ion aqueous solutions coupled with complex formation. *Colloids Surf., A* **2008***, 324*, 222-227.
36. Iida, K.; Suematsu, N. J.; Miyahara, Y.; Kitahata, H.; Nagayama, M.; Nakata, S. Experimental and theoretical studies on the self-motion of a phenanthroline disk coupled with complex formation. *Phys. Chem. Chem. Phys.* **2010***, 12*, 1557-1563.
37. Zhang, J.; Pelton, R. Poly(N-isopropylacrylamide) Microgels at the Air-Water Interface. *Langmuir* **1999***, 15*, 8032-8036.
38. Nakata, S.; Hayashima, Y.; Komoto, H. Spontaneous switching of camphor motion between two chambers. *Phys. Chem. Chem. Phys.* **2000***, 2*, 2395-2399.
39. Kitahata, H.; Hiromatsu, S.; Doi, Y.; Nakata, S.; Rafiqul Islam, M. Self-motion of a camphor disk coupled with convection. *Phys. Chem. Chem. Phys.* **2004***, 6*, 2409-2414.
40. Nakata, S.; Doi, Y.; Kitahata, H. Synchronized motion of a mobile boundary driven by a camphor fragment. *J. Colloid Interface Sci.* **2004***, 279*, 503-508.
41. Soh, S.; Bishop, K. J. M.; Grzybowski, B. A. Dynamic Self-Assembly in Ensembles of Camphor Boats. *J Phys Chem B* **2008***, 112*, 10848-10853.
42. Suematsu, N. J.; Tateno, K.; Nakata, S.; Nishimori, H. Synchronized Intermittent Motion Induced by the Interaction between Camphor Disks. *J. Phys. Soc. Jpn.* **2015***, 84*, 034802-034808.
43. Soh, S.; Branicki, M.; Grzybowski, B. A. Swarming in Shallow Waters. *J. Phys. Chem. Lett.* **2011***, 2*, 770-774.

44. Satterwhite-Warden, J.; Kondepudi, D. K.; Dixon, J. A.; Rusling, J. F. Co-operative motion of multiple benzoquinone disks at the air-water interface. *Phys. Chem. Chem. Phys.* **2015***, 17*, 29891-29898.
45. Berg, H. C. The rotary motor of bacterial flagella. *Annu. Rev. Biochem.* **2003***, 72*, 19-54.
46. Nakata, S.; Nagayama, M.; Kitahata, H.; Suematsu, N. J.; Hasegawa, T. Physicochemical design and analysis of self-propelled objects that are characteristically sensitive to environments. *Phys. Chem. Chem. Phys.***2015***, 17*, 10326-10338.
47. Shioi, A.; Katano, K.; Onodera, Y. Effect of solid walls on spontaneous wave formation at water/oil interfaces. *J. Colloid Interface Sci.* **2003***, 266*, 415-421.

Chapter Four:

Online Microfluidic Protein Capture Electrochemical Assay of CD62L for the Assessment of Metastasis in Bladder Cancer

4.1 Abstract

Increasing interest in targeting cancer diagnostics tools for personalized treatment plans creates a niche for analytical methodologies that can provide information regarding staging and metastatic potential in cancer patients. Such technologies would significantly assist in improving patient prognosis for bladder cancer, as late stage detection has very low 5-year survival rate of <40%. Herein, we describe a low-cost, sensitive bead-based electrochemical immunoarray for L-selectin (or CD62L protein), a potential biomarker for monitoring metastasis; that utilized a semi-automated modular system with online antigen capture and detection. The assay employed superparamagnetic beads decorated with thousands of detection antibodies and enzyme labels, amplifying signals generated during amperometric detection. Our assay provided a detection limit at 0.25 ng mL^{-1} with a dynamic range of 0.25 to 100 ng mL^{-1} and significantly higher sensitivity than ELISA. 41 patient samples at varying stages and metastatic advancement of bladder cancer were analyzed by both the immunoarray and ELISA. CD62L protein level for both assays showed an increasing trend with worsening locoregional spread of tumor; although, significantly decreased circulating concentrations for high-grade tumors with metastasis were observed. This approach highlights the potential of CD62L as a biomarker for regional and distant metastasis in bladder cancer cases.

4.2 Introduction

Bladder cancer distresses the cells that line the inner portion of the bladder; depending on how the cells appear, a class/type of bladder cancer is determined. Detection and diagnosis of bladder cancer is extremely essential as this solid tumor is the fourth most common in men and eighth in women.[1] Furthermore, according to the American Cancer Society, ~74,000 newly diagnosed cases (about 75% in men and 25% in women) and ~16,000 deaths are estimated to occur in 2016.[1] Currently, the five-year survival rates are dependent upon whether the cancer is localized in the inner layer, advanced regionally or deeper within the layers of the bladder (distant), these rates are 88%, 35% and 6%, respectively.[2, 3] Therapies for advanced bladder cancer are substandard, even after aggressive surgical procedures and medicinal treatments these patients succumb to the disease.[4, 5] The most predictive factor is the presence of lymph node metastasis; however, presently, tumor biomarkers are not clinically employed for determination of patient's progression, prognosis or treatment, and there are no set forecasters of metastatic potential.[1, 6, 7] Therefore, it is crucial that a sensitive diagnostic tool is developed to predict and further monitor the likelihood of metastasis during staging of bladder cancer.

Although most cases of bladder cancer are superficial and noninvasive, tumors can alternatively become low- or high-grade lesions. Low-grade lesions have the risk of recurrence; however, high-grade tumors possess the ability to spread to distant organs due to the tumor plaguing the muscle wall of the bladder; consequently metastasis, a multistep process, has potential to transpire.[6, 8] Metastasis emerges when tumor cells from a localized zone begin to proliferate, consequently tumor cells then spread intravenously or through the lymphatic pathway.[8-10] Therefore, knowledge of metastatic potential could serve as a diagnostic tool for

stage prognosis of bladder cancer lesions. This is essential as survival rates for locoregional bladder cancer are significantly high compared to distant.

Recent research has been directed at understanding the biological process involved in cancer progression to provide improved targeted and personalized therapy. More specifically, major attention has focused on the involvement and presence of metastatic lymph nodes as a prognosis factor that dictates the choice of treatment.[8, 11] Due to poor prognosis at advanced bladder cancer stages currently; it is particularly important to develop a biomarker-based test, which would aid in staging of the bladder cancer tumor.[11-14] Proteins participating in lymphatic pathways provide a pool of potential biomarkers for predicting metastasis. Thus, selectins, a class of mammalian vascular adhesion molecules, have been studied and subsequently implicated as indicators for advanced progression of diseases.[15-20] Specifically, L-selectin (also called sL-selectin), expressed on a variety of inflammatory cells, plays a crucial role in homing and migration mechanism of lymphocytes to lymph nodes.[21-23] A previous study comparing low-grade and high-grade bladder cancer samples showed an over-expression of L-selectin transcript in both primary tumor sections and lymph nodes tumors in metastatic cases.[6] More specifically, Choudhary et al. were able to confirm substantial correlation between the protein expression and tumor type by a variety of experimental studies, such as quantitative polymerase chain reaction (PCR), immunohistochemistry, enzyme-linked immunoabsorbent assay (ELISA), and flow cytometry.[6] This particular study established the potential of CD62L to serve as a tumor biomarker. Therefore, clinically relevant studies should be conducted with circulating levels of soluble L-selectin as a potential biomarker for increased risk of metastasis, leading to a more targeted approach in treatment plan.

Our biomarker discovery research and quantitation protocol employs a modular semi-automated microfluidic system with online capture and detection units, yielding a significantly more sensitive, timely assay than currently available ELISA or bead-based immunoassays.[24] Our approach incorporates magnetic beads, densely labeled with detection antibody and horseradish peroxidase (HRP), to complete a modified sandwich immunoassay followed by amperometric detection, providing a fast and low-cost alternative to traditional ELISA tests. The versatility of this approach has been shown in ultrasensitive quantitation of cytokines, such as interleukin-6 (IL-6) and interleukin-8 (IL-8)[24-26], prostate specific antigen (PSA)[27], and other protein markers[28, 29] at femtogram (fg) to picogram (pg) levels in human serum, in single biomarker and multiplexed detection mode.

Consequently, since CD62L has the potential to predict the presence or risk for developing metastatic potential/disease in patients with bladder cancer, our work focused on quantifying CD62L expression in patients with varied low- or high-grade growths using our electrochemical immunoarray strategy. Herein, we adapted our previously established modular approach to detect higher nanogram (ng) circulating protein levels of CD62L by modifying the number of enzyme labels on the magnetic bead bioconjugate, providing a new aspect of flexibility to the bead-based immunoassay protocol. This adjustment provided an assay detection limit of 0.25 ng mL^{-1} and accuracy was demonstrated by performing multiple method validation experiments. Serum samples from healthy and bladder cancer afflicted patients were analyzed by our method, and reflected a similar trend to one observed by employing a traditional ELISA platform. The analytical approach detailed in this paper was able to differentiate various stages of bladder cancer; in addition, provided metastatic potential information.

4.3 Experimental

4.3.1 Materials

Screen-printed 8-electrode carbon array (700 μm diameter) sensors were purchased from Kanichi Research Services Ltd (Manchester, England), poly(diallydimethylammonium chloride) (PDDA, MW 200,000-300,000, 20% in water), L-glutathione reduced (GSH, ≥98%), gold (III) chloride trihydrate ($HAuCl_4 \bullet 3H_2O$, ≥99.9%), sodium borohydride ($NaBH_4$, 99%), 1-(3-(dimethylamino)propyl)-3-ethylcarbodiimide hydrochloride (EDC), N-hydroxysulfosuccinimide (NHSS), bovine serum albumin (BSA), calf serum, Tween-20, sodium chloride (NaCl), potassium chloride (KCl), sodium phosphate dibasic (Na_2HPO_4, ≥98%), sodium phosphate monobasic monohydrate ($NaH_2PO_4 \bullet 3H_2O$, ≥98%), hydroquinone (HQ, ≥99%), hydrogen peroxide (H_2O_2, 30%) were purchased from Sigma-Aldrich (St. Louis, MO, USA). The polydimethylsiloxane (PDMS) kit was obtained from Dow Corning (Auburn, MI, USA). Streptavidin-coated superparamagnetic beads (MP, 1 μm Dynabeads) and biotinylated horseradish peroxidase (HRP, 2.5 mg mL^{-1}) were purchased from Life Technologies (Carlsbad, CA, USA). All solutions were prepared using 18 MΩ•cm water purified by passing house-distilled water through a Hydro Service and Supplies purification system (Durham, NC, USA).

Monoclonal anti-human L-Selectin (CD62L) antibody (Ab_1, Catalog Number: BBA24, Clone: 4G8), biotinylated anti-human L-Selectin antibody (Ab_2, Catalog Number: BAF728), recombinant human L-Selectin/CD62L protein antigen (Ag, Catalog Number: ADP2), and Human sL-Selectin/CD62L ELISA kit (Catalog Number: BBE4B) were purchased from R&D Systems (Minneapolis, MN, USA). Human serum samples were collected from healthy patients and cancer-inflicted patients between 2012 and 2013 from the University of Connecticut Health Center (UCHC). Upon approval from the IRB and Written Informed Consent from patients,

serum sample collection was completed at the time of surgery (TURBT or cystectomy). All samples were stored at or below -80°C until used.

4.3.2 Methods

4.3.2.1 Fabrication of Microfluidic System Device Chambers

The microfluidic capture and detection chambers were constructed as previously reported.[24, 27] Briefly, microfluidic channel molds were machined in-house for both the capture and detection chambers. These molds were then filled with PDMS and allowed to cure to form soft PDMS microfluidic channels of desired dimensions. Each microfluidic channel type was then sandwiched between two hard flat poly(methylmethacrylate) (PMMA) plates, which were also machined in-house, and at as support slabs that are then bolted together. For the capture chamber device, the top PMMA plate contained inlet and outlet female ports (4 mm diameter) for standard male plastic fittings (1.5 mm, Upchurch) to hold PEEK tubing (i.d.= 0.2 mm). These same inlet and outlet ports were machined on the detection chamber; however, this top PMMA plate also contained two parallel holes at 0.6 mm and two parallel holes at 0.2 mm for a Ag/AgCl wire and platinum wire, respectively. Machined microfluidic devices are shown in **Figure 4.1**.

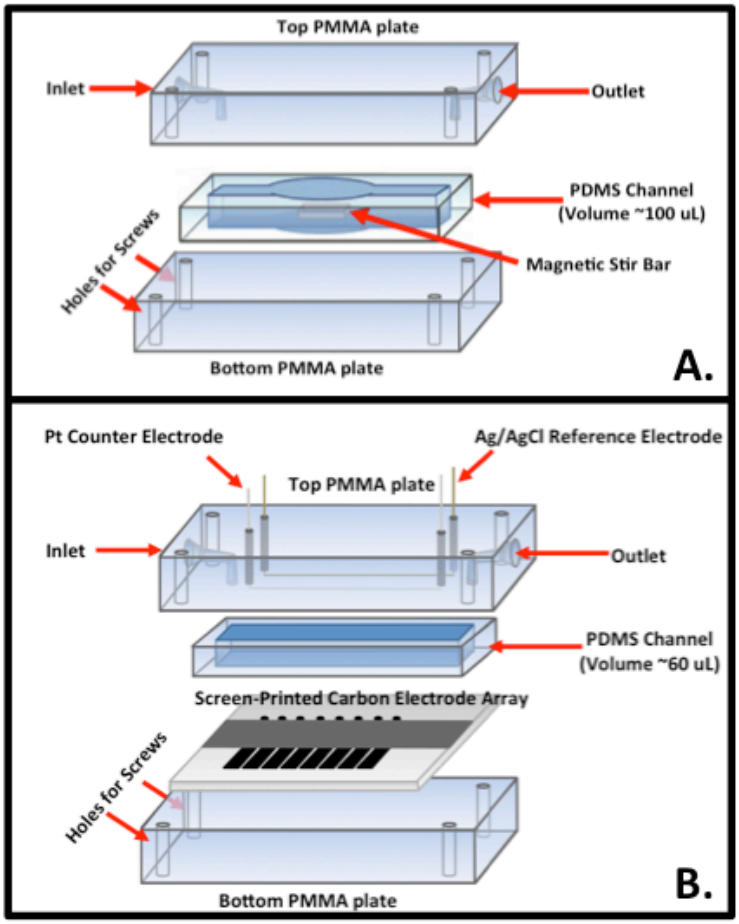

Figure 4.1: Schematic illustration of microfluidic in-house machined devices. A) The online capture chamber device for which the target protein becomes captured by heavily labeled bioconjugates to form the protein-antigen bioconjugates. B) The detection chamber device that houses the Ab_1 modified working electrode array, counter wire electrode, and reference wire electrode.

4.3.2.2 Immobilization of Proteins to Form Immunoarray Sensor

Screen-printed 8-electrode carbon array sensors were fabricated as previously described.[24, 25, 27, 28] Briefly, arrays were coated with successive layers of polycation PDDA and negatively charged 5 nm glutathione-coated gold nanoparticles (GSH-AuNPs) using layer-by-

layer (LBL) electrostatic adsorption for 20 min each, as previously reported and as illustrated in **Figure 4.2A**.[28, 30] Incubating a freshly prepared crosslinking solution of EDC and NHSS for 10 min activated terminal surface carboxyl groups on the GSH-AuNP layer. Then the electrode sensor arrays were subsequently spotted with primary antibody (Ab_1), which was allowed to incubate overnight at 4°C resulting in Ab_1 immobilization via an amidization reaction, **Figure 4.2A**.[27, 28] Furthermore, prior to utilizing, the arrays were blocked with 2% BSA in PBS for 1 hr at 4°C to inhibit non-specific binding (NSB).

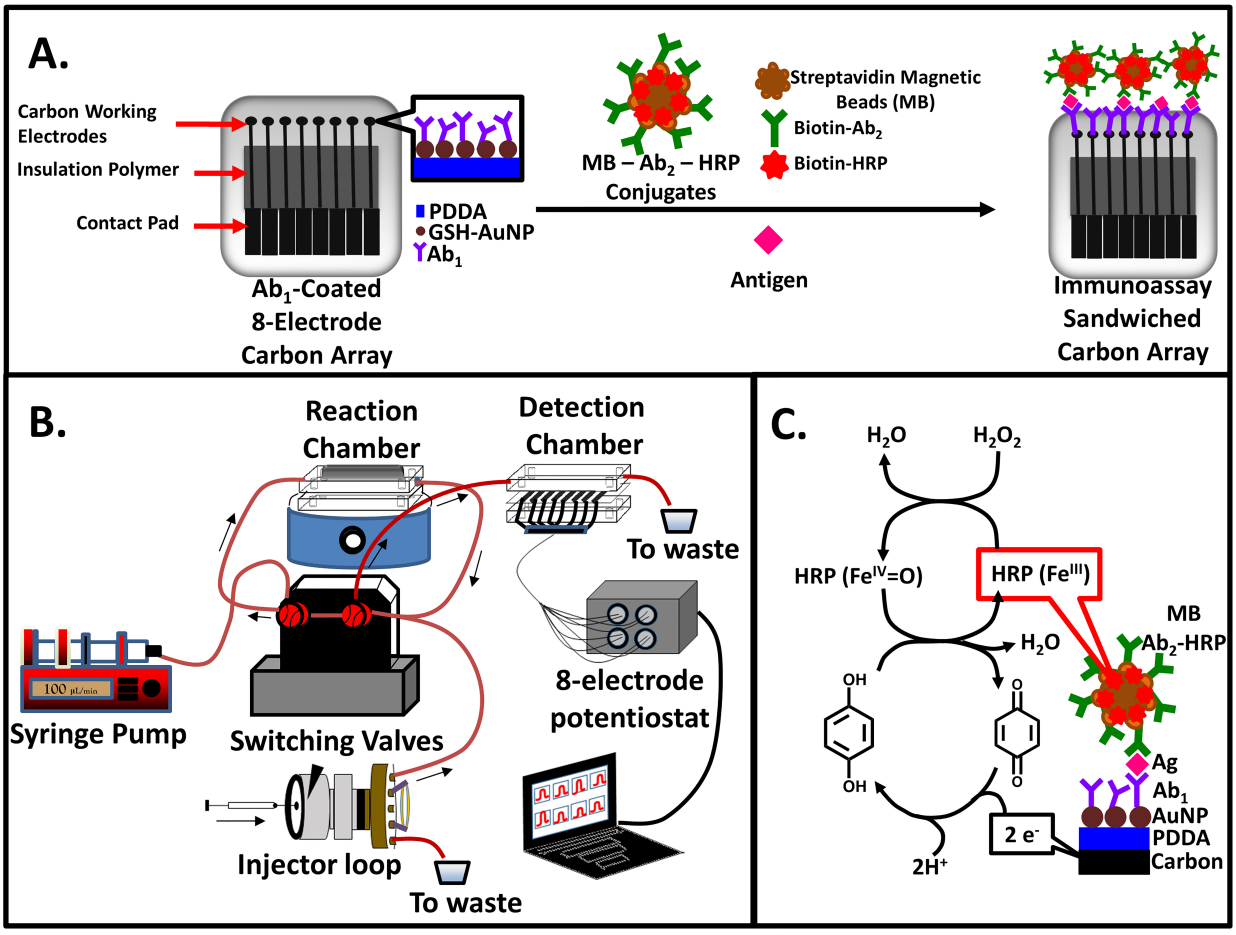

Figure 4.2: Schematic illustration of the online-capture microfluidic assay. A) Strategy for modified ELISA was performed on B) a modular semi-automatic setup, where MB-Ab_2-HRP conjugate was incubated with antigen in an online capture chamber and then flowed to the

detection chamber for incubation with surface-bound primary antibodies. C) 1 mM HQ and 0.1 mM H_2O_2 was injected for quantitative amperometric detection.

4.3.2.3 Preparation of Bioconjugates

A previous protocol was implemented for the attachment of numerous biotinylated–Ab_2 and biotinylated–HRP labels to 1 μm diameter streptavidin-coated superparamagnetic beads (MPs, 10 mg mL^{-1}), as illustrated in **Figure 4.2A**.[24, 25, 27, 28, 31] Briefly, MPs were magnetically separated using an Invitrogen DynaMag spin magnet and subsequently washed with PBS pH 7.4 three separate times. Then simultaneously biotinylated–Ab_2 and biotinylated–HRP were added into the MP dispersion containing 0.1% BSA in PBS pH 7.4 at a ratio of 1:2:4:4 (MP:Ab_2:HRP:BSA) followed by incubation at 37°C for 30 min. After conjugation, the bead bioconjugate (MP-Ab_2-HRP, **Figure 4.2A**) dispersion was magnetically separated and washed three distinct times with 0.1% BSA in PBS pH 7.4 to remove any NSB Ab_2 and HRP. Lastly, the bioconjugate was then reconstituted with 0.1% BSA in PBS pH 7.4 and stored at 4°C until needed.

Once optimized concentrations of both Ab_2 and HRP were determined, characterization assays were completed. Specifically, the average number of Ab_2 per MP was ~11,000 (± 1800), estimated via bicinchoninic acid assay (BCA) kit (Thermo Scientific, Rockland, IL, USA).[32] In addition, the average number of HRP per MP was estimated to be ~21,400 (± 3,600) by 2,2'-azino-bis(3-ethylbenzthiazoine-6-sulfonic acid) (ABTS) end-point assay (Sigma Aldrich, St. Louis, MO, USA).[33, 34] Absorbances were measured for each assay experiment using FlexStation 3 multi-mode microplate reader (Molecular Devices, Sunnyvale, CA, USA).

4.3.2.4 On-line Capture and Detection Protocol

The general immunoassay capture strategy is illustrated in **Figure 4.2**. An established modular on-line protein capture microfluidic system was employed, as shown in **Figure 4.2B**, and this system provided a semi-automated methodology for protein detection.[24, 25] More specifically, the system was constructed with an on-line capture chamber upstream from a detection chamber encasing an 8-electrode modified sensor array. This modular microfluidic system was previously reported; however, further detail on assay performance will be briefly described.[24, 25, 35]

To begin, the system was first subjected to a flow of water, using a syringe pump (Ne-1000 High Pressure, Harvard Apparatus), followed by PBS-Tween 20. The detergent solution was used to minimize adhesion and NSB of undesirable molecules. Once the fluidic system was washed, 50 μL of bioconjugate (MP-Ab_2-HRP) was added to 150 μL of 20 mM PBS pH 7.4. This bioconjugate dispersion was then loaded into a 100 μL sample loop, injected (Model No: 9725i, Rheodyne) at 100 μL min^{-1}, and allowed to fill the capture chamber. Next, protein antigen (standard or patient sample) in diluted calf serum was loaded and then injected into the capture chamber. Once the capture chamber was filled, stirring within the chamber was allowed for 30 min to facilitate protein capture. Throughout both sequentially injections, a magnet bar was held atop the capture chamber to ensure MP-Ab_2-HRP were captured.

After the 30 min incubation period, resultant protein antigen-MP-Ab_2-HRP bioconjugates were transferred to the detection chamber, which was housing a CD62L Ab_1 modified 8-electrode immunoarray, by switching the valves in the proper direction and pumping PBS-Tween 20 at 100 μL min^{-1} carried the protein antigen-MP-Ab_2-HRP into the detection chamber. The flow was stopped once the red-brown color of MPs filled the entire channel; this provided an

indication the transfer process was complete. Bioconjugates incubated at the electrode surfaces for 15 min to allow efficient capturing and completion of the immunoarray sandwich, **Figure 4.2A**. PBS-Tween 20 flow resumed to remove any unbound bioconjugates followed by further washing with hydroquinone (HQ) for production of an electrochemical background signal. Amperometric detection was completed at -0.2 V vs. Ag/AgCl by injecting a mixture of 1 mM HQ mediator and 0.1 mM hydrogen peroxide (H_2O_2) at 100 μL min^{-1} into the detection chamber via the sample loop to activate the HRP labels on the bioconjugates. Prior to detection, the 8-electrode sensor array, platinum (Pt) counter, and Ag/AgCl reference were connected to a CHI 1040BC multipotentiostat (**Figure 4.2B**). An electrochemical redox-cycle, **Figure 4.2C**, transpired and current signals developed.[24-26, 30] Amperometric current signals are proportional to concentration of protein analyte. Once electrochemical detection was complete, a fresh modified 8-electrode array was inserted into the detection chamber for exposure to the next sample, which was still undergoing protein capture.

4.3.2.5 Patient Sample Analysis and Data Processing

After method optimization and validation, 41 patient serum samples were analyzed using both ELISA kit BBE4B and the immunoarray procedure detailed above. Calibration, bar plots, correlation plots were processed with Kaleida graph, while further patient sample analysis, such as, box plots and receiver operating characteristic (ROC) studies, were performed on MedCalc statistical software.

4.4 Results

4.4.1 Optimization of Enzyme label

Enzyme labels densely attached onto MP bioconjugates were optimized prior to accessing CD62L protein antibodies. This critical optimization step permits extension of the dynamic range from pg mL^{-1} to ng mL^{-1}, which is explained in detail in the Discussion section. In particular, four different sets of MPs with varying concentrations of HRP labels, specifically 0.25, 0.5, 1.25 and 2.5 mg mL^{-1}, and a constant concentration of Ab_2 were prepared as previously described. Following preparation, assays were performed by injection of a control (0 ng mL^{-1}, no analyte protein), low (1 ng mL^{-1}), and high (10 ng mL^{-1}) antigen sample for each respective biotin–HRP concentration. As observed in **Figure 4.3A**, 0.5 mg mL^{-1} biotin–HRP provided the greatest signal difference between low and high concentrations; therefore, 0.5 mg mL^{-1} was utilized for further optimization processes and attainment of the standard calibration curve.

4.4.2 Optimization of Antibodies for Protein CD62L

Additionally, the capture antibody (Ab_1) and detection antibody (Ab_2) bound on the immunoarray platform and MP bioconjugate respectively were critically optimized to achieve maximum signal sensitivity prior to execution of a standard calibration curve. First, the detection antibody was optimized. In particular, the concentration of HRP and Ab_1 were kept constant and MP bioconjugates were prepared with three different Ab_2 concentrations, specifically 5, 10 and 20 μg mL^{-1}. Subsequently, assays were performed by injection of a control (0 ng mL^{-1}, no analyte protein), low (1 ng mL^{-1}), and high (10 ng mL^{-1}) antigen sample for each respective bioconjugate concentration and amperometric current signals were compared. The optimum concentration of 10 μg mL^{-1} Ab_2 was selected, as shown in **Figure 4.3B.**

The concentration of the primary antibody is crucial as this improves assay sensitivity and minimizes NSB. Therefore, arrays with varying concentrations of Ab_1, specifically 5, 20, and 100 μg mL^{-1}, were prepared and the immunoassay was completed by the aforementioned procedure. During this Ab_1 optimization process, biotin–Ab_2 and biotin–HRP concentrations were kept constant. After comparison between each of the amperometric current signals, 100 μg mL^{-1} Ab_1 was selected and employed as the optimum concentration, as indicated in **Figure 4.3C**. Therefore, the best immunoarray performance was obtained when 100 μg mL^{-1} Ab_1 was bound on the sensor surface, while 10 μg mL^{-1} Ab_2 and 0.5 mg mL^{-1} HRP were attached to the MP bioconjugates. These conditions were employed for all latter experiments.

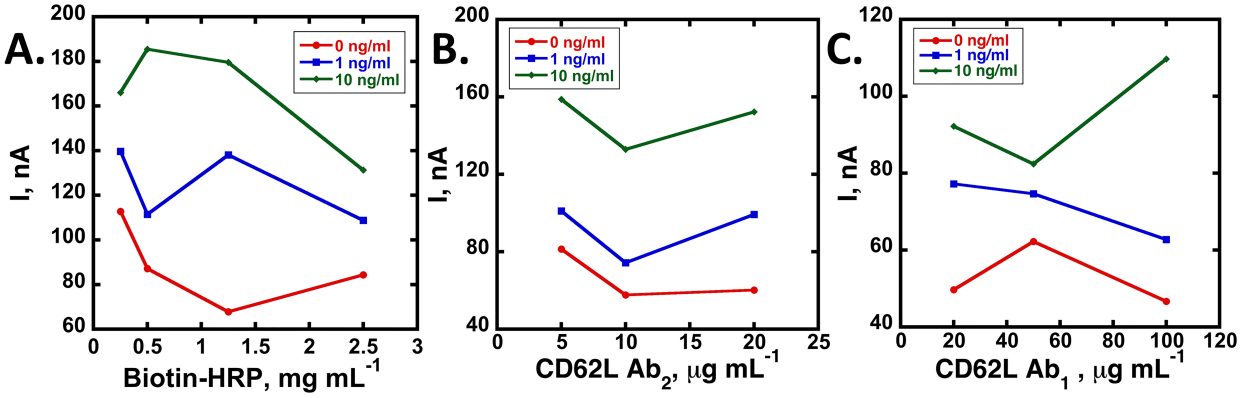

Figure 4.3: Optimization results for CD62L sandwich immunoarray performance upon employing standard concentrations of 0, 1 and 10 ng mL^{-1}. A) Optimization of Biotin-HRP using consistent Ab_1 and Ab_2 concentrations. Optimal concentration of biotin-HRP was determined to be 0.5 mg mL^{-1}. B) Optimized result for secondary antibody (Ab_2) using consistent Ab_1 and biotin-HRP label concentrations. Optimal concentration of Ab_2 was determined to be 10 μg mL^{-1} and C) Optimized outcome for primary antibody (Ab_1) using consistent Ab_2 and biotin-HRP label concentrations. Optimal concentration of Ab_1 was determined to be 100 μg mL^{-1}.

4.4.3 *Immunoarray Standard Calibration of Protein CD62L*

Implementation of the aforementioned immunoassay protocol utilizing optimized protein and enzyme label conditions provided a standard calibration curve for soluble CD62L. Amperometric signals for CD62L controls were a consequence of residual NSB of MP bioconjugates. A linear relationship between amperometric signal and log CD62L concentration was established in the ng mL^{-1} range. A detection limit, measured as three times the standard deviation of the control, was observed at 0.25 ng mL^{-1} and the dynamic range extended to 100 ng mL^{-1}, as shown in **Figure 4.4A and B**. Good reproducibility was signified by small error bars (n=8). Furthermore, excellent sensitivity (slope of calibration plot) of approximately 33.90 nA ± 1.32 $(\log[\text{CD62L}], \text{ng } mL^{-1})^{-1}$ and $R^2 \geq 0.98$, as revealed in **Figure 4.4A and B**, were achieved for our 30 min assay time.

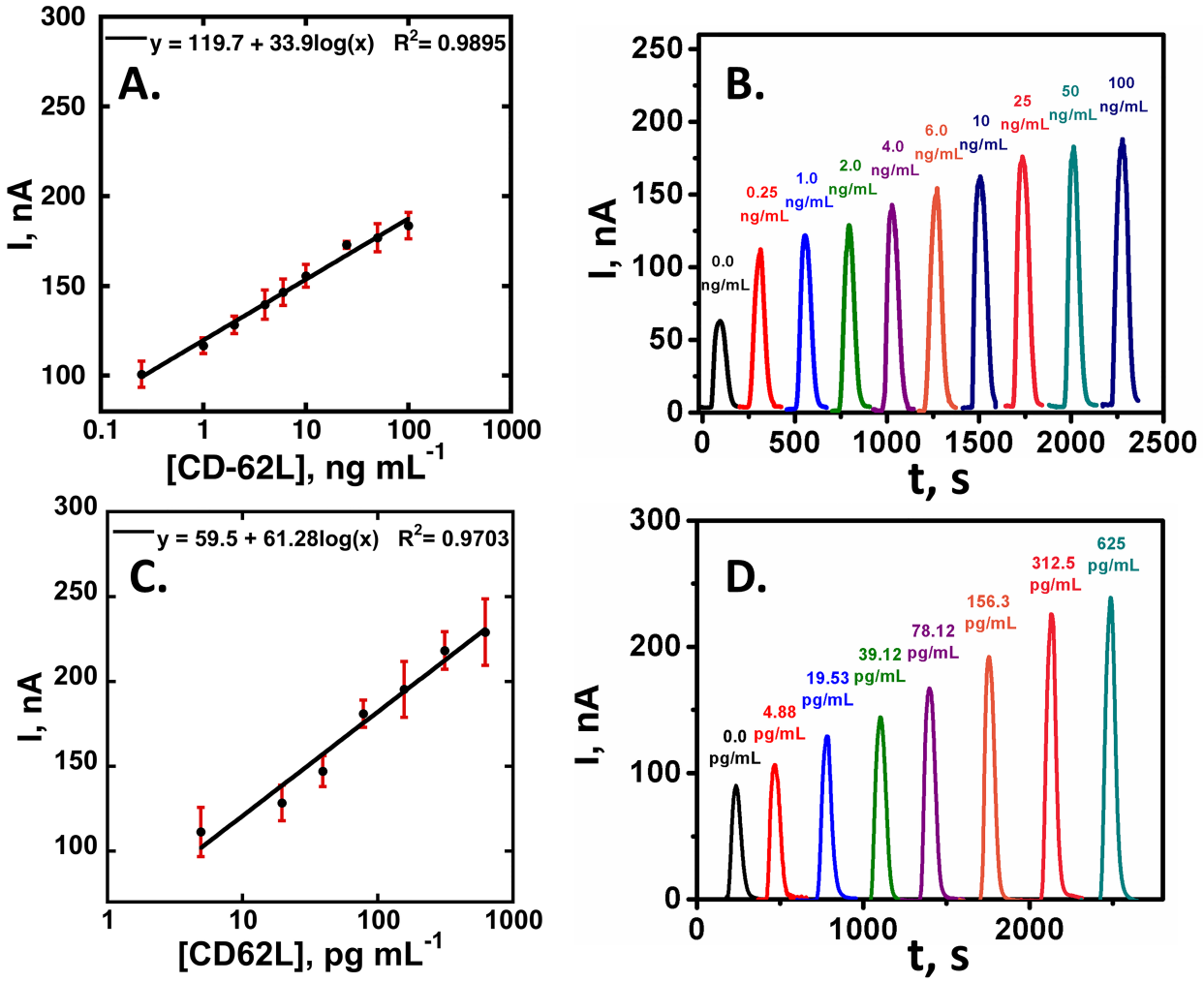

Figure 4.4: Calibration for protein CD62L standard was performed in 5-fold diluted calf serum and current signals were acquired by injecting a mixture of 1 mM HQ and 0.1 mM H_2O_2 at -0.2 V vs. Ag/AgCl. A) Reduced HRP acquired calibration plot and B) amperometric current signals with a dynamic range from 0.25 ng mL^{-1} to 100 ng mL^{-1}. C) Unreduced HRP attained calibration plot and D) amperometric current signals with dynamic range from 4.88 pg mL^{-1} to 625 pg mL^{-1}.

The calibration was observed to be reliable over numerous days with agreement in both slope and y-intercept. Moreover, three selected concentrations were assayed on different days to test reproducibility of the amperometric signal. (**Figure 4.5A**). Additionally, the stability of the Ab_1 modified immunoarray platform was scrutinized up to 7 days after modification and

discovered to be stable with minimal change in the amperometric response as seen in **Figure 4.5B**. Signals demonstrated good reproducibility as observed by relative standard deviations of less than 5%.

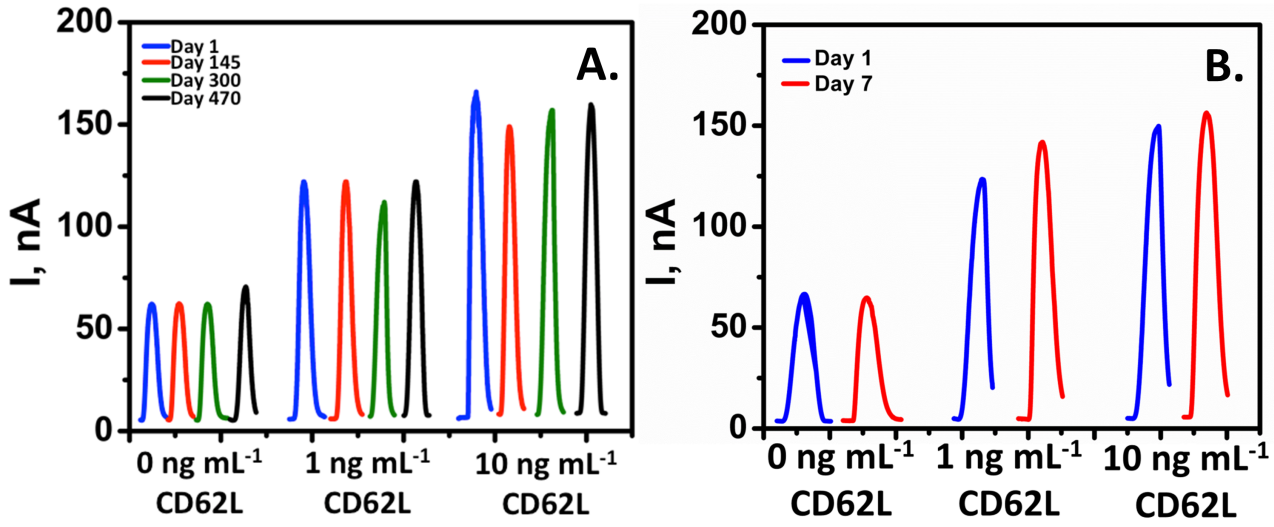

Figure 4.5: Amperometric signals to demonstrate assay reliability and stability. A) Current signals from four independent days for 0, 1, and 10 ng mL^{-1} CD62L. B) Comparison of current signals indicating stability of surface bound Ab_1 on the LBL sensor array over duration of one week for 0, 1, and 10 ng mL^{-1} CD62L.

4.4.4 Assay Validation Using Spiked Calf Serum Samples

Prior to performing patient samples, our capture and detection immunoarray system was assessed by spiking serum with different concentrations of CD62L standards to ensure accuracy and reliability. Human serum contained high levels of indigenous protein CD62L; therefore, calf serum was used to mimic the patient sample composition. Calf serum was spiked at 75, 250, 350, 550, 700, 1500, 3000 and 5500 ng mL^{-1} and diluted 100-fold with PBS pH 7.4 prior to analysis to replicate the patient sample pre-dilution protocol. The recovery amongst the eight spiked

samples was observed to be within 83–116% for our immunoarray system, which falls within analytical allowed limits, whereas ELISA yielded varying recoveries within 37–97%, as displayed in **Figure 4.6**.[36]

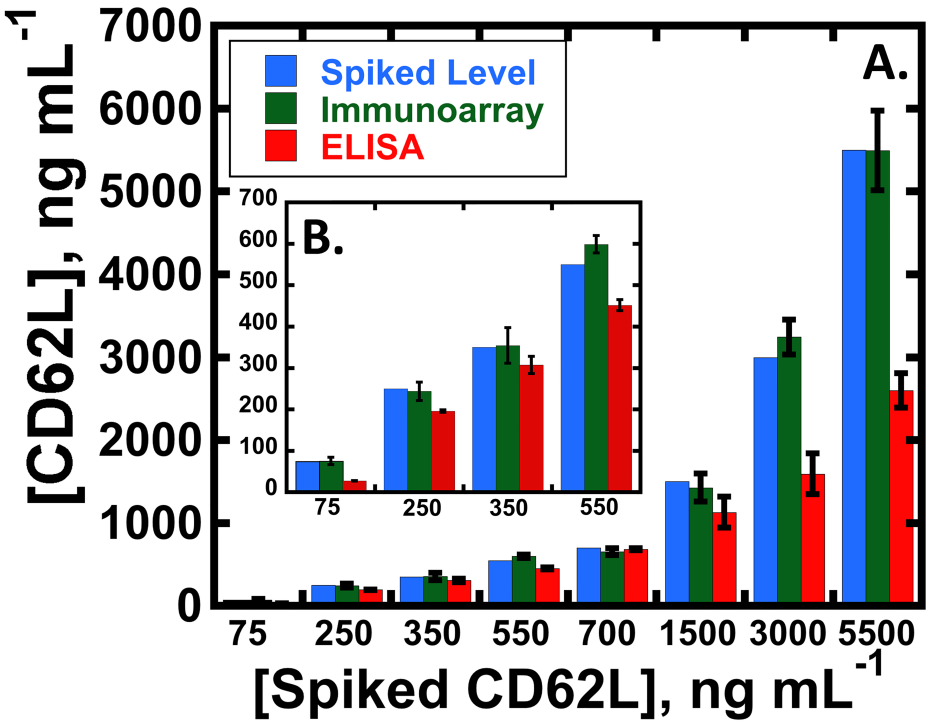

Figure 4.6: A comparison of our immunoarray results versus ELISA with known spiked levels (75, 250, 350, 550, 700, 1500, 3000 and 5500 ng mL-1) of CD62L standards in calf serum. Recovery was observed to be within 83%–116% for our immunoarray and 37–97% for standard ELISA. B) Zoomed inset for spiking levels 75, 250, 350, and 550 ng mL^{-1}.

4.4.5 Bladder Cancer Patient Serum Sample Analysis

The microfluidic online capture and immunoarray detection platform was utilized to measure CD62L in a total of 41 serum samples from bladder cancer patients. Specifically, 41 patient samples were analyzed, which comprise of 10 healthy individual samples and 31 cancer-infected human samples at various stages of bladder cancer. In particular, 11 samples were from

local low-grade tumors, while 20 were high-grade tumors, which were equally divided between those expressing either no metastasis or at least regional metastasis. Samples (5 μL) were diluted 100-fold in PBS pH 7.4 prior to assay performance to ensure samples were within the dynamic range of the standard calibration. The resultant immunoarray average CD62L protein level was 367.4 ± 141.8 ng mL^{-1} for healthy, 2243 ± 839 ng mL^{-1} for low-grade, 4551 ± 1662 ng mL^{-1} high-grade non-metastatic, and 1177 ± 532 ng mL^{-1} for high-grade metastatic tumors. Furthermore, standard ELISA was performed and yielded results for CD62L protein level at 811.3 ± 237.1 ng mL^{-1} for healthy, 1151 ± 250 ng mL^{-1} for low-grade, 1895 ± 539 ng mL^{-1} high-grade non-metastatic, and 917.0 ± 408.5 ng mL^{-1} for high-grade metastatic tumor samples.

4.5 Discussion

4.5.1 Modification of immunoassay protocol

Soluble CD62L protein in human serum was reported at high ng mL^{-1} levels previously employing standard ELISA analysis.[15, 37-40] For our bead-based modified ELISA a standard calibration curve for protein CD62L, generated by employing 2.5 mg mL^{-1} biotin-HRP (as previously reported[25]), 20 μg mL^{-1} Ab_2 and 50 μg mL^{-1} Ab_1, provided a dynamic range of 4.88 pg mL^{-1} to 625 pg mL^{-1} as seen in **Figure 4.4C and D**. While high sensitivity was achieved (slope of 61.28 ± 4.80 nA log[CD62L, pg mL^{-1}])$^{-1}$), patient sample dilution of >10,000-fold would be necessary to remain within the dynamic range. Consequently, a change to the immunoassay protocol herein was required to shift the calibration into a more relevant dynamic range ensuring clinical samples were not diluted immensely; to circumvent imparting dilution error. The two primary methodologies that could be exploited for the above mentioned purpose were a) modification in incubation times for antibody-antigen reaction[26] or b) modification in HRP labels

present on the MPs. To preserve future multiplexing capability across fg mL^{-1} to ng mL^{-1} protein levels, the latter of the two modification protocols was implemented.

On adaptation of the modified protocol with reduced enzyme label, detection limit increased from 4.88 pg mL^{-1} to 0.25 ng mL^{-1}, while extending the dynamic range to 0.25 ng mL^{-1} to 100 ng mL^{-1}, as seen in **Figure 4.4**. Hence, our modification to the protocol successfully adapted the assay to the required concentration range, while providing a greater biomarker multiplexing possibility in the future.

4.5.2 Assessment of Soluble CD62L Level for Staging Bladder Cancer

Dot box plots were employed to visualize trends in sL-selectin levels for four subsets of patient samples for both our electrochemical immunoarray and ELISA detection methods. An ascending trend in circulating protein levels was observed concurrent with increasing severity of bladder cancer stage; an exception was seen for high-grade metastatic tumors (**Figure 4.7A and B).** The box plots indicated minimal overlap between the pooled sample data for individual subsets, for our immunoarray protocol, which was corroborated by performing ROC analysis.

ROC plots were utilized to assess diagnostic accuracy, wherein true positive rate (sensitivity) was plotted versus false positive rate (specificity). Specifically, this assessment tool quantified the capability to distinguish healthy clinical samples versus disease stricken samples. In order to perfectly differentiate patients with and without cancer, an ROC plot must demonstrate 100% sensitivity, 100% specificity, and area under the curve (AUC) of 1.0. ROC plots were generated, as observed in **Figure 4.8A-G,** for all combinations of patient sample subsets to obtain corresponding sensitivity, specificity, AUC, and concentration cut-off criteria parameters (**Table 4.1**). Generally sensitivity $\geq$ 70%, specificity $\geq$ 70%, and AUC $\geq$ 0.50 were obtained for both Immunoarray and ELISA for all ROC combination groupings. Significant

differences were acquired by Two Sample Mean T-test ($P < 0.05$, **Table 4.4**) for all subset comparisons, expect for healthy vs. high-grade metastatic and low-grade vs. high-grade metastatic for ELISA and this will be further discussed in a latter subsection.[41] Although significant difference were obtained for both detection methods, our immnoarray protocol provided enhanced sensitivity and specificity compared to standard ELISA. Therefore, we concluded for each scenario, our Immunoarray detection method provided better discrimination between different tumor classifications.

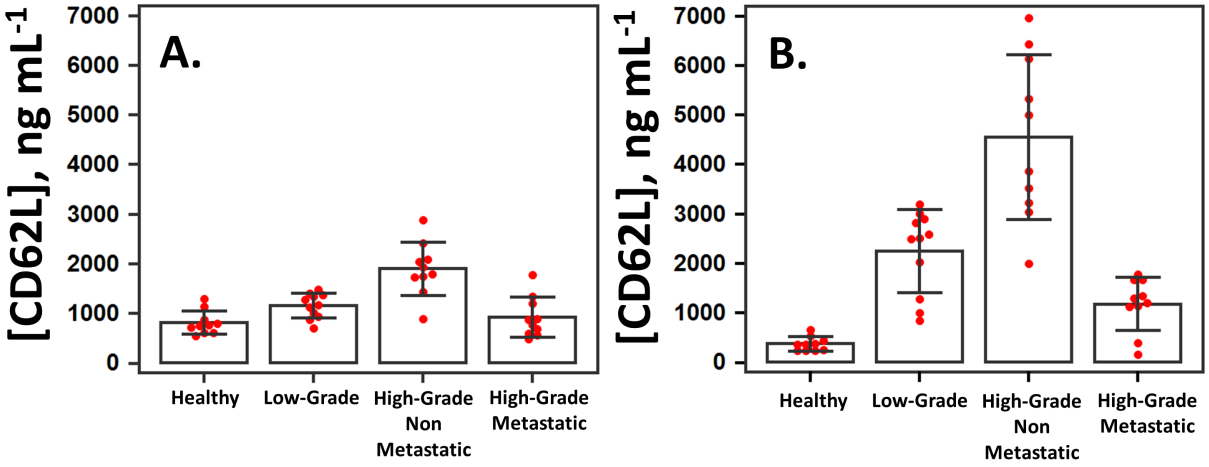

Figure 4.7: Dot box plot analysis for 41 patient samples for four different subsets tumors (healthy, low-grade, high-grade non-metastatic, and high-grade metastatic). A) ELISA B) Electrochemical Immunoarray, for which red dots represent individual recovered patient sample concentrations. Box plot height represents the mean and error bars were plotted at 1 standard deviation of the mean.

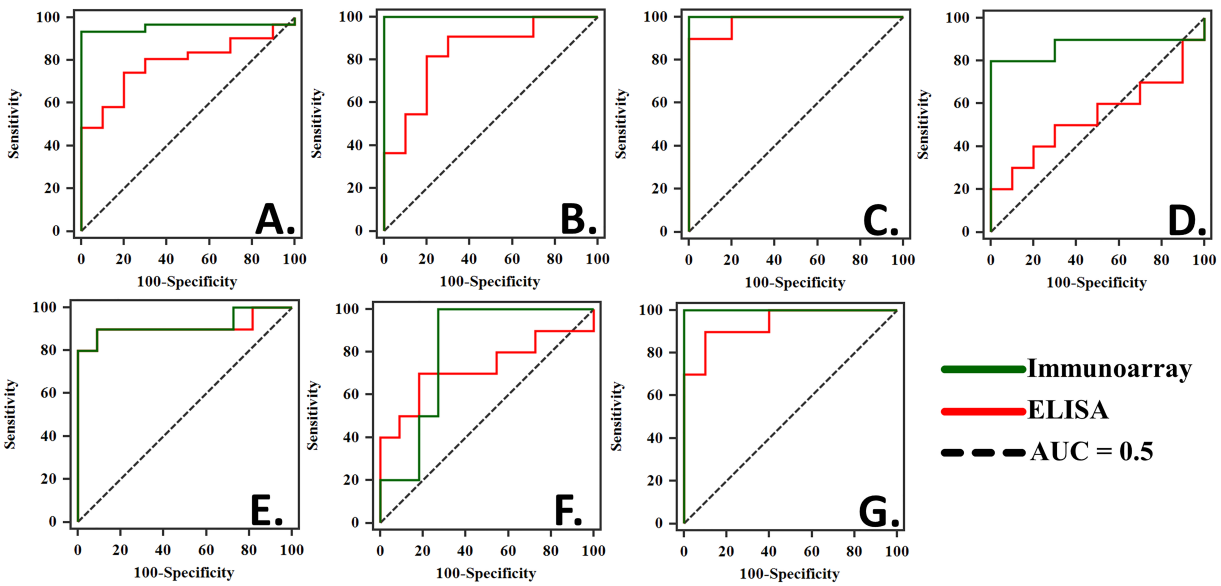

Figure 4.8: Receiver operating characteristic (ROC) curves comparing A) healthy vs. all cancer patient samples, B) healthy vs. low-grade C) healthy vs. high-grade non-metastatic, D) healthy vs. high grade metastatic, E) low-grade vs. high-grade non-metastatic, F) low grade vs. high-grade metastatic, and G) high-grade non-metastatic vs. high-grade metastatic.

Table 4.1: ROC analysis parameters for combination of four patient sample subsets.

ROC Comparison	Assay Type	Sensitivity	Specificity	AUC	Criterion
Healthy vs. All Cancers	Immunoarray	93.55	100.0	0.958	>649.7
	ELISA	74.19	80.00	0.787	>873.8
Healthy vs. Low-Grade	Immunoarray	100.0	100.0	1.000	>649.7
	ELISA	81.82	80.00	0.836	>873.8
Healthy vs. High-Grade Non-Metastatic	Immunoarray	100.0	100.0	1.000	>649.7
	ELISA	90.00	100.0	0.980	>1291
Healthy vs. High-Grade Metastatic	Immunoarray	80.00	100.0	0.870	>649.7
	ELISA	40.00	80.00	0.540	>873.8
Low-Grade vs. High-Grade Non-Metastatic	Immunoarray	90.00	90.91	0.918	>3010
	ELISA	90.00	90.91	0.909	>1401
Low-Grade vs. High-Grade Metastatic	Immunoarray	100.0	72.23	0.809	≤1783
	ELISA	70.00	81.82	0.727	≤881.0
High-Grade Non-Metastatic vs. High-Grade Metastatic	Immunoarray	100.0	100.0	1.000	≤1783
	ELISA	90.00	90.00	0.940	≤1338

4.5.3 Investigation of Differential Recoveries for ELISA and Immunoarray

Immunoarray results for circulating CD62L levels generated a linear correlation with standard ELISA for 41 samples (10 healthy and 31 cancer samples). More specifically, correlations produced a slope of 2.764 ± 0.283, y-intercept -1208 ± 371, and $R^2 = 0.7101$, as seen in **Figure 4.9A**. The slope is greater than 1 for our method; therefore, supporting our finding of higher sensitivity compared gold standard ELISA.

To comprehend the deviations in the slope and y-intercept, correlation plots for Immunoarray vs. ELISA for spiked sample recoveries (**Figure 4.9B**), ELISA vs. true spiked levels (**Figure 4.9C**), and Immunoarray vs. true spiked levels (**Figure 4.9D**) were generated. ELISA results versus true spiked levels yielded a slope of 0.4551 ± 0.0327 as seen in **Figure 4.9B**, well beneath the expected value of 1. This indicated the presence of a systematic error at low and high concentrations, specifically outside the concentration range of 350 - 1500 ng mL^{-1}. However, the error was not observed in the Immunoarray against true spiked levels (**Figure 4.9C**) as seen by a slope of 1.013 ± 0.020 with y-intercept at 0.1298 ± 0.4686. To investigate if systematic error was affecting both spiked and patient sample results regression studies and T-tests were performed.

Parameters obtained from correlation plots were treated to One Sample Mean T-Test, Two Sample Mean T-Test, and Linear Regression T-test, which are individually discussed in detail in the next subsection of the discussion. Briefly, these series of aforementioned T-tests confirmed uniform systematic error was present for both spiked and patient sample analysis. Therefore, we inferred that the recovered concentrations for patient samples from ELISA potentially were falsely elevated or depressed at the low (near 350 ng mL^{-1}) and high

concentrations (>1500 ng mL^{-1}) respectively, thus partially masking the distinction between the four patient sample subsets as observed in **Figure 4.7**. These statistical analyses support the reliable accuracy of our microfluidic CD62L immunoassay.

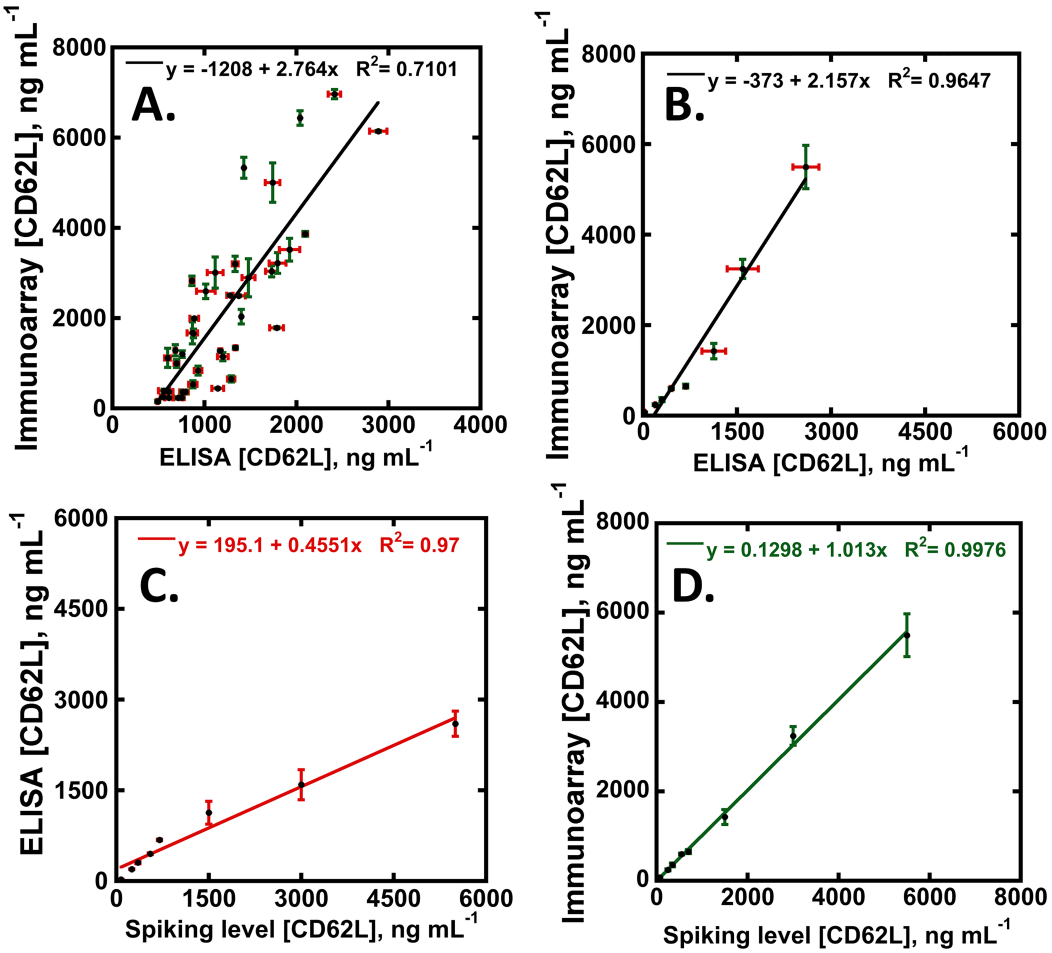

Figure 4.9: Linear correlation plots for both our immunoarray detection method and standard ELISA for protein CD62L. A) Plot of immunoarray results against ELISA for detection of CD62L in human serum samples from patient samples. B) Relationship between spiked sample recoveries for our immunoarray system against ELISA. C) Comparison result of known spiked level versus detected ELISA. D) Correlation outcome between spiked known CD62L level and detected level for the immunoarray.

4.5.2 Statistical Studies on Immunoarray versus ELISA Data

4.5.2.1 T-test Analysis for Assay Accuracy with Spiked Sample Analysis

Correlation plots were prepared for spiked sample analysis by plotting Immunoarray recoveries versus ELISA recoveries (**Figure 4.9B),** ELISA recoveries versus spiked levels (**Figure 4.9C**), and finally Immunoarray recoveries against spiked levels (**Figure 4.9D**). The first plot reported similarity between the two detection methods, while the latter two plots provided information on the accuracy of the detection method in reporting recovered concentration. All correlation plots demonstrated a linear relationship. However, from the set of correlations plotted, only Immunoarray recoveries against spiked levels yielded a slope close to 1 (1.013 ± 0.020) and y-intercept near 0 (0.1298 ± 46.86), as observed in **Table 4.2**.

Verification of statistically relevant differences in slopes was performed by Linear Regression T-tests at 95% confidence interval (CI).[41, 42] Recovered concentrations in comparison to true spiked levels were utilized, and resultant information from Linear Regression T-Test was evaluated upon differences observed in $t_{statistical}$ and $t_{critical}$. Specifically, $t_{statistical}$ was calculated using deviation from expected slope of 1 and observed standard error of the slope. Meanwhile, $t_{critical}$ was a tabulated value from required CI and degrees of freedom.[41, 42] In cases where $t_{statistical} > t_{critical}$ ($P < 0.05$), deviations from expected results are statistically significant. As observed in **Table 4.2**, the only concentration recoveries that were statistically similar to true spiked concentrations ($P > 0.05$) were for our Immunoarray detection method. ELISA recoveries compared to true spiked levels were statistically different at $P = <0.00001$. Hence, these results strongly demonstrated the presence of a systematic error with the ELISA kit used for CD62L analysis.

Table 4.2: Statistical results for Linear Regression T-Test was performed for correlation plot slopes at 95% CI.

Linear Regression Plot	Slope ± SD	y-intercept ± SD (ng mL^{-1})	T-Test at 95% CI
Immunoarray vs. Spiked level†	1.013 ± 0.020	0.1298 ± 46.86	no diff.
ELISA vs. Spiked level†	0.4551 ± 0.0327	195.1 ± 75.3	**sig. diff.**
Spiked sample recoveries† Immunoarray vs. ELISA	2.157 ± 0.169	-373.0 ± 201.0	**sig. diff.***
Patient sample recoveries‡ Immunoarray vs. ELISA	2.764 ± 0.283	-1208 ± 371	**sig. diff.***

† n = 8, ‡ n = 41, Null hypothesis was slope of correlation plot = 1.
* represents statistically similar systematic error between the patient sample recoveries and spiked sample recoveries, as analyzed by linear regression T-test
sig. diff. represents significantly different based on $t_{statistical} > t_{critical}$
no diff. represents statistically similar based on $t_{statistical} < t_{critical}$

For further validation, a One Sample Mean T-test was first performed for individual spiked levels and this process was completed for each distinctive detection method.[41, 42] More specifically, lower and upper concentration limits at 95% CI were calculated for individual recovered levels, as shown in **Table 4.3**. The specific detection method was considered accurate if the corresponding true spiked level was within the calculated range (For example, 75 ng mL^{-1} lies within the limits of 53.26 to 97.44 ng mL^{-1}). This test was also performed at 90% CI and yielded similar results (data not shown). From **Table 4.3,** we concluded that significant differences were obtained outside the concentration range of 350 - 1500 ng mL^{-1} for ELISA. Such trend was not observed for our method, specifically, our Immunoarray detection method yielded recovery concentrations statistically similar to true spiked levels at 95% CI at all spiked levels.

Furthermore, comparison between the distinctive methods was executed by employing the Two Sample Mean T-test.[41, 42] Specifically, in our case, null hypothesis was set such that the recovered ELISA concentrations would equal the recovered Immunoarray concentrations and

$t_{statistical} > t_{critical}$ ($P < 0.05$) signified significant difference in recoveries. Upon comparison at each spiked level per methodology we concluded good correlation for the concentration range of 350 - 1500 ng mL^{-1}, with exception of 550 ng mL^{-1} (**Table 4.3**). These statistical results support the reliable accuracy of our microfluidic CD62L immunoassay, and reveal large systematic errors in low and high concentration ranges for the ELISA kit used.

Table 4.3: Statistical results for One Sample Mean T-test and Two Sample Mean T-Test performed at 95% CI for spiked samples (n = 3 for Immunoarray, n = 2 for ELISA).

Spiked Level (ng mL^{-1})	**Immunoarray**		**ELISA**		**Two Sample Mean T-Test at 95% CI***
	Calculated Conc. Range	T-Test at 95% CI	Calculated Conc. Range	T-Test at 95% CI	
75	53.26 – 97.44	no diff.	18.95 – 35.97	**sig. diff.**	**sig. diff.**
250	201.1 – 304.8	no diff.	169.7 – 221.9	**sig. diff.**	**sig. diff.**
350	249.0 – 425.4	no diff.	121.2 – 493.2	no diff.	no diff.
550	555.9 – 641.9	no diff.	290.4 – 623.4	no diff.	**sig. diff.**
700	565.0 – 739.4	no diff.	578.6 – 784.8	no diff.	no diff.
1500	1008 – 1844	no diff.	-280.0 – 2333	no diff.	no diff.
3000	2722 – 3763	no diff.	601.7 – 2250	**sig. diff.**	**sig. diff.**
5500	4305 – 6681	no diff.	921.4 – 4465	**sig. diff.**	**sig. diff.**

*represents Two Sample Mean T-test analysis for the null hypothesis, ELISA recovered concentration = Immunoarray recovered concentration
sig. diff. represents significantly different based on $t_{statistical} > t_{critical}$
no diff. represents statistically similar based on $t_{statistical} < t_{critical}$

4.5.2.2 Assay Validation for Patient Sample Analysis with T-tests

Patient sample recoveries for all 41 samples (healthy and cancer) from our Immunoarray method when plotted against ELISA recoveries (for the same samples) possessed a linear correlation with $R^2 = 0.7101$; however the slope deviated from expected value of 1 (2.763 ± 0.283) and the y-intercept from expected value of 0 (-1208 ± 371) (**Figure 4.9A**, **Table 4.2**). These results were significantly different from expected linear correlation when subjected to

Linear Regression T-test (performed as explained above) at 95% CI ($P<0.05$) (**Table 4.2**) and at 90% CI (data not shown). Due to the observed deviations between standard CD62L ELISA and our analytical method, systematic error in ELISA for patient sample analysis was also suspected.

Therefore, to investigate if any systematic error was effecting the correlation studies completed for patient sample recoveries, linear regression T-Test was subsequently performed between correlation plots for patient sample recoveries (**Figure 4.9A**) and spiked sample recoveries (**Figure 4.9B**). This t-test yielded $P = 0.2196$ at 95% CI and since $P > 0.05$, systematic error in CD62L ELISA was uniformly present in both spiked and patient sample analysis, as denoted by the blue asterisk in **Table 4.2**. In conclusion, the patient sample recoveries with our bead-based method provided more accurate estimates of soluble CD62L levels in patient serum samples than the traditional ELISA assay kit.

4.5.2.3 Assessing Specificity of Immunoarray Method in Bladder Cancer Tumor Staging

The dot box plots (**Figure 4.7**) demonstrated analogous trends between the bladder cancer tumor stages for both ELISA and Immunoarray. Therefore, to confirm specificity of differentiation between patient sample subsets (healthy, low-grade, high-grade non-metastatic, and high-grade metastatic) Two Sample Mean T-Test was performed at 95% CI as previously described. From **Table 4.4**, both assay detection methods distinguished tumor grade based upon soluble detected CD62L, with the exception of ELISA for healthy vs. high-grade metastatic as well as low-grade vs. high-grade metastatic tumors. Although both assay detection methods differentiate between patient sample subsets, our immunoarray method performs at a higher confidence ($P_{Immunoarray} << P_{ELISA}$).

Table 4.4: Two Sample Mean T-Test at 95% CI to demonstrate differential CD62L protein level in patient sample subsets.

Patient Sample Subset Comparison Type	Assay Type	Two Sample Mean T-Test at 95% CI*
Healthy vs. All Cancers	Immunoarray	**sig. diff.**
	ELISA	**sig. diff.**
Healthy vs. Low-Grade	Immunoarray	**sig. diff.**
	ELISA	**sig. diff.**
Healthy vs. High-Grade Non-Metastatic	Immunoarray	**sig. diff.**
	ELISA	**sig. diff.**
Healthy vs. High-Grade Metastatic	Immunoarray	**sig. diff.**
	ELISA	no diff
Low-Grade vs. High-Grade Non-Metastatic	Immunoarray	**sig. diff.**
	ELISA	**sig. diff.**
Low-Grade vs. High-Grade Metastatic	Immunoarray	**sig. diff.**
	ELISA	no diff
High-Grade Non-Metastatic vs. High-Grade Metastatic	Immunoarray	**sig. diff.**
	ELISA	**sig. diff.**

*n = 10 for healthy patient subset, n = 11 for low-grade tumors subset, n = 10 for high-grade non-metastatic tumors and n = 10 for high-grade metastatic tumor subset. Null hypothesis was set as, mean of patient sample subset 1 = mean of patient sample subset 2.
sig. diff. represents significantly different based on $t_{statistical} > t_{critical}$
no diff. represents statistically similar based on $t_{statistical} < t_{critical}$

Furthermore, patient sample subset means for both detection methods were analyzed by implementing a Paired T-Test.[41, 42] Mean differences and standard deviation between the paired samples recoveries provided a $t_{statistical}$ value; meanwhile, $t_{critical}$ was calculated as mentioned previously. In cases where $t_{statistical} > t_{critical}$ ($P < 0.05$) deviations from expected results are statistically significant. Calculations were performed at 95% CI and 90% CI (data not shown for the latter). The analytical methods correlate well only for high-grade metastatic tumors, as the mean for this subset is within the 350 – 1500 ng mL^{-1} concentration range, as seen in **Table 4.5**. This statistical result further validated the presence of systematic error in low and high

concentration ranges for ELISA; therefore, our CD62L Immunoarray still exhibited higher reliability.

Table 4.5: Statistical results from Paired T-test for each bladder cancer tumor subset across all intra-subset samples at 95% CI.

Sample Type	Average Concentration ± SD (ng mL^{-1})		Paired T-Test at 95% CI*
	Immunoarray	ELISA	
Healthy	367.4 ± 141.8	811.3 ± 237.1	**sig. diff.**
Low-Grade	2243 ± 839	1151 ± 250	**sig. diff.**
High-Grade Non-Metastatic	4551 ±1662	1895 ± 539	**sig. diff.**
High-Grade Metastatic	1177 ± 532	917.0 ± 408.5	no diff.

*n = 10 for healthy patient subset, n = 11 for low-grade tumors subset, n = 10 for high-grade non-metastatic tumors and n = 10 for high-grade metastatic tumor subset. Null hypothesis was set as, Immunoarray detected concentration – ELISA detection concentration = 0.
sig. diff. represents significantly different based on $t_{statistical} > t_{critical}$
no diff. represents statistically similar based on $t_{statistical} < t_{critical}$

Whilst such recovery errors were commonly attributed to matrix interferences in the ELISA platform, such as high-dose Hook effect, differential dilution factors within sample sets have been successfully employed to ensure quantification with high accuracy.[43-46] However, our method provided an additional benefit by allowing a single dilution factor over the entirety of the calibration range, indicating higher sensitivity achieved for our method. Due to higher sensitivity achievement, this semi-automated assay module provides a promising tool, with less technical burden, for bladder cancer protein CD62L in a short time of 30 mins for minimal patient sample requirement.

Overall, our sensitive, reliable immunoassay procedure when compared to the gold standard ELISA, demonstrated a substantial increase in soluble CD62L protein expression level between the subsets for healthy vs. all tumor samples, healthy vs. low-grade tumors, and low- vs. high-grade non-metastatic tumors. However, the decreased circulating protein concentration

from high-grade non-metastatic to high-grade metastatic tumor samples was a deviation from our hypothesized theory. Such observation can be potentially explained by two distinctive concepts. First, the high-grade metastatic tumor subset could possibly have tumor heterogeneity. More specifically, the dramatic divergence from the expected tumor progression trend could be due to changes in the molecular biomarker due to structurally alternations. These deviations of the primary tumor hypothetically can explain the underexpression of CD62L in the metastatic case. Secondly, although the mainstream process of a tumor during muscle invasion is the mechanical loss and shedding of the related cellular protease, which in turn increases soluble protein, may not actually transpire for CD62L. Since, there is distinctive underexpression of circulating CD62L in the high-grade metastatic subset, this suggests that CD62L is not being cleaved and/or shed. To confirm our theory and further validate the staging information we can infer from our immunoarray results, cell lysate studies using our electrochemical immunoarray system need to be employed. These studies could validate the results acquired in study and could provide a biological explanation for the underexpression observed.

4.6 Conclusion

The sensitive bead-based immunoarray method employed in this paper allowed alteration to the calibration dynamic range by optimizing the number of enzyme labels on magnetic bead bioconjugates. Application of this method for detection of circulating CD62L protein achieved differentiation between concentrations of CD62L at varying stages of bladder cancer. Our assay provided useful information for assessing metastatic potential in patients; therefore, our study offers support that CD62L can be employed in alternative clinical studies to further assess the potential as a protein tumor biomarker for staging and grading bladder cancer. Consequently,

since our system has increased adaptability, a panel of biomarkers, such as NMP22 or IL-6 including CD62L could be investigated for staging bladder cancer with enhanced confidence.

4.7 Acknowledgments

This work was financially supported by Connecticut Institute for Clinical and Translational Science (CICATS) and grant no. EB014586 from the National Institute of Biomedical Imaging and Bioengineering (NIBIB), NIH. The authors thank Drs. Gregory Bishop, Chandra Dixit, and Brunah Otieno for critical discussion and Saira Bakshi for experimental input.

4.8 References

1. American Cancer Society. Cancer facts and figures. Atlanta: American Cancer Society; 2016
2. Herr, H. W.; Donat, S. M. Outcome Of Patients With Grossly Node Positive Bladder Cancer After Pelvic Lymph Node Dissection And Radical Cystectomy. *J. Urol.* **2001***, 165*, 62-64.
3. Ries, L. A. G.; Melbert, D.; Krapcho, M.; Stinchcomb, D.G.; Howlader, N.; Horner, M. J.; Mariotto, A.; Miller, B. A.; Feuer, E. J.; Altekruse, S. F.; Lewis, D. R.; Clegg, L.; Eisner, M. P.; Reichman, M.; Edwards, B. K. (eds) SEER Cancer Statistics Review, 1975-2005, National Cancer Institute. Bethesda, MD, http://seer.cancer.gov/csr/1975_2005/, based on November 2007 SEER data submission, posted to the SEER web site, 2008 (accessed Aug 19, 2016).
4. Watts, K. L.; Ristau, B. T.; Yamase, H. T.; Taylor III, J. A. Prognostic implications of lymph node involvement in bladder cancer: are we understaging using current methods? *BJU Int.* **2011***, 108*, 484-492.
5. Shariat, S. F.; Karakiewicz, P. I.; Palapattu, G. S.; Lotan, Y.; Rogers, C. G.; Amiel, G. E.; Vazina, A.; Gupta, A.; Bastian, P. J.; Sagalowsky, A. I.; Schoenberg, M. P.; Lerner, S. P. Outcomes of Radical Cystectomy for Transitional Cell Carcinoma of the Bladder: A Contemporary Series From the Bladder Cancer Research Consortium. *J. Urol.* **2006***, 176*, 2414-2422.
6. Choudhary, D.; Hegde, P.; Voznesensky, O.; Choudhary, S.; Kopsiaftis, S.; Claffey, K. P.; Pilbeam, C. C.; Taylor III, J. A. Increased expression of L-selectin (CD62L) in high-grade urothelial carcinoma: A potential marker for metastatic disease. *Urol. Oncol.: Semin. Orig. Invest.* **2015***, 33*, 387.e17-387.e27.
7. Stein, J. P.; Lieskovsky, G.; Cote, R.; Groshen, S.; Feng, A.; Boyd, S.; Skinner, E.; Bochner, B.; Thangathurai, D.; Mikhail, M.; Raghavan, D.; Skinner, D. G. Radical Cystectomy in the Treatment of Invasive Bladder Cancer: Long-Term Results in 1,054 Patients. *J. Clin. Oncol.* **2001***, 19*, 666-675.
8. Mitra, A. P.; Datar, R. H.; Cote, R. J. Molecular Pathways in Invasive Bladder Cancer: New Insights Into Mechanisms, Progression, and Target Identification. *J. Clin. Oncol.* **2006***, 24*, 5552-5564.
9. Christiansen, A.; Detmar, M. Lymphangiogenesis and Cancer. *Genes Cancer* **2011***, 2*, 1146-1158.
10. Williams, S. G.; Stein, J. P. Molecular pathways in bladder cancer. *Urol. Res.* **2004***, 32*, 373-385.
11. Milowsky, M. I.; Rumble, R. B.; Booth, C. M.; Gilligan, T.; Eapen, L. J.; Hauke, R. J.; Boumansour, P.; Lee, C. T. Guideline on Muscle-Invasive and Metastatic Bladder Cancer (European Association of Urology guideline): American Society of Clinical Oncology Clinical Practice Guideline Endorsement. *J. Clin. Oncol.* **2016**.
12. Schiffer, E.; Vlahou, A.; Petrolekas, A.; Stravodimos, K.; Tauber, R.; Geschwend, J.; Neuhaus, J.; Stolzenburg, J.; Conaway, M. R.; Mischak, H.; Theodorescu, D. Prediction of Muscle-invasive Bladder Cancer Using Urinary Proteomics. *Clin. Cancer Res.* **2009***, 15*, 4935-4943.
13. Frantzi, M.; Latosinska, A.; Fluhe, L.; Hupe, M. C.; Critselis, E.; Kramer, M. W.; Merseburger, A. S.; Mischak, H.; Vlahou, A. Developing proteomic biomarkers for bladder cancer: towards clinical application. *Nat. Rev. Urol.* **2015***, 12*, 317-330.

14. Ye, F.; Wang, L.; Castillo-Martin, M.; McBride, R.; Galsky, M. D.; Zhu, J.; Boffetta, P.; Zhang, D. Y.; Cordon-Cardo, C. Biomarkers for bladder cancer management: present and future. *Am J. Clin. Exp. Urol.* **2014***, 2*, 1-14.
15. Haznedaroğlu, I. C.; Benekli, M.; Ozcebe, O.; Savaş, M. C.; Güllü, I. H.; Dündar, S. V.; Kirazli, Ş. Serum L-selectin and P-selectin levels in lymphomas. *Haematologia* **2000***, 30*, 27-30.
16. Matsuura, N.; Narita, T.; Mitsuoka, C.; Kimura, N.; Kannagi, R.; Imai, T.; Funahashi, H.; Takagi, H. Increased Level of Circulating Adhesion Molecules in the Sera of Breast Cancer Patients With Distant Metastases. *Jpn. J. Clin. Oncol.* **1997***, 27*, 135-139.
17. Wittig, B. M.; Kaulen, H.; Thees, R.; Schmitt, C.; Knolle, P.; Stock, J.; Meyer zum Büschenfelde, K. H.; Dippold, W. Elevated serum E-selectin in patients with liver metastases of colorectal cancer. *Eur. J. Cancer* **1996***, 32*, 1215-1218.
18. Bélanger, S. D.; St-Pierre, Y. Role of selectins in the triggering, growth, and dissemination of T-lymphoma cells: implication of L-selectin in the growth of thymic lymphoma. *Blood* **2005***, 105*, 4800-4806.
19. Vlad, A.; Deglesne, P.; Letestu, R.; Saint-Georges, S.; Chevallier, N.; Baran-Marszak, F.; Varin-Blank, N.; Ajchenbaum-Cymbalista, F.; Ledoux, D. Down-regulation of CXCR4 and CD62L in Chronic Lymphocytic Leukemia Cells Is Triggered by B-Cell Receptor Ligation and Associated with Progressive Disease. *Cancer Res.* **2009***, 69*, 6387-6395.
20. Ay, C.; Simanek, R.; Vormittag, R.; Dunkler, D.; Alguel, G.; Koder, S.; Kornek, G.; Marosi, C.; Wagner, O.; Zielinski, C.; Pabinger, I. High plasma levels of soluble P-selectin are predictive of venous thromboembolism in cancer patients: results from the Vienna Cancer and Thrombosis Study (CATS). *Blood* **2008***, 112*, 2703-2708.
21. McEver, R. P. Selectin-carbohydrate interactions during inflammation and metastasis. *Glycoconj. J.* **1997***, 14*, 585-591.
22. Qian, F.; Hanahan, D.; Weissman, I. L. L-selectin can facilitate metastasis to lymph nodes in a transgenic mouse model of carcinogenesis. *Proc. Natl. Acad. Sci. U. S. A.* **2000***, 98*, 3976-3981.
23. Arbonés, M. L.; Ord, D. C.; Ley, K.; Ratech, H.; Maynard-Curry, C.; Otten, G.; Capon, D. J.; Teddert, T. F. Lymphocyte homing and leukocyte rolling and migration are impaired in L-selectin-deficient mice. *Immunity* **1994***, 1*, 247-260.
24. Otieno, B. A.; Krause, C. E.; Latus, A.; Chikkaveeraiah, B. V.; Faria, R. C.; Rusling, J. F. On-line Protein Capture on Magnetic Beads for Ultrasensitive Microfluidic Immunoassays of Cancer Biomarkers. *Biosens. Bioelectron.* **2013***, 53*, 10.1016/j.bios.2013.09.054.
25. Krause, C. E.; Otieno, B. A.; Bishop, G. W.; Phadke, G.; Choquette, L.; Lalla, R. V.; Peterson, D. E.; Rusling, J. F. Ultrasensitive microfluidic array for serum pro-inflammatory cytokines and C-reactive protein to assess oral mucositis risk in cancer patients. *Anal. Bioanal. Chem.* **2015***, 407*, 7239-7243.
26. Krause, C. E.; Otieno, B. A.; Latus, A.; Faria, R. C.; Patel, V.; Gutkind, J. S.; Rusling, J. F. Rapid Microfluidic Immunoassays of Cancer Biomarker Proteins Using Disposable Inkjet-Printed Gold Nanoparticle Arrays. *ChemistryOpen* **2013***, 2*, 141-145.
27. Chikkaveeraiah, B. V.; Mani, V.; Patel, V.; Gutkind, J. S.; Rusling, J. F. Microfluidic Electrochemical Immunoarray for Ultrasensitive Detection of Two Cancer Biomarker Proteins in Serum. *Biosens. Bioelectron.* **2011***, 26*, 4477-4483.
28. Malhotra, R.; Patel, V.; Chikkaveeraiah, B. V.; Munge, B. S.; Cheong, S. C.; Zain, R. B.; Abraham, M. T.; Dey, D. K.; Gutkind, J. S.; Rusling, J. F. Ultrasensitive Detection of Cancer

Biomarkers in the Clinic using a Nanostructured Microfluidic Array. *Anal. Chem.* **2012***, 84*, 6249-6255.
29. Chikkaveeraiah, B. V.; SoldÃ , A.; Choudhary, D.; Maran, F.; Rusling, J. F. Ultrasensitive nanostructured immunosensor for stem and carcinoma cell pluripotency gatekeeper protein NANOG. *Nanomedicine (London, England)* **2012***, 7*, 957-965.
30. Mani, V.; Chikkaveeraiah, B. V.; Patel, V.; Gutkind, J. S.; Rusling, J. F. Ultrasensitive Immunosensor for Cancer Biomarker Proteins Using Gold Nanoparticle Film Electrodes and Multienzyme-Particle Amplification. *ACS Nano* **2009***, 3*, 585-594.
31. Otieno, B. A.; Krause, C. E.; Rusling, J. F. Chapter Seven - Bioconjugation of Antibodies and Enzyme Labels onto Magnetic Beads. *Meth. Enzymol.* **2016***, 571*, 135-150.
32. Smith, P. K.; Krohn, R. I.; Hermanson, G. T.; Mallia, A. K.; Gartner, F. H.; Provenzano, M. D.; Fujimoto, E. K.; Goeke, N. M.; Olson, B. J.; Klenk, D. C. Measurement of protein using bicinchoninic acid. *Anal. Biochem.* **1985***, 150*, 76-85.
33. Keesey, J. *Biochemical Information,* 1st ed.; Boehringer Mannheim Biochemicals; Indianapolis, 1987, pp. 58.
34. Pütter, J.; Becker, R. Evaluation of Experimental Results. In: *Methods of Enzymatic Analysis;* Bergmeyer, H.U, Ed.; Verlag Chemie Weinheim; New York, 1983; Vol. 3; p. 286–293.
35. Dixit, C. K.; Kadimisetty, K.; Otieno, B. A.; Tang, C.; Malla, S.; Krause, C. E.; Rusling, J. F. Electrochemistry-based approaches to low cost, high sensitivity, automated, multiplexed protein immunoassays for cancer diagnostics. *Analyst* **2016***, 141*, 536-547.
36. Rozet, E.; Marini, R. D.; Ziemons, E.; Boulanger, B.; Hubert, P. Advances in validation, risk and uncertainty assessment of bioanalytical methods. *J. Pharm. Biomed. Anal.* **2011***, 55*, 848-858.
37. Font, J.; Pizcueta, P.; Ramos-Casals, M.; Cervera, R.; García-Carrasco, M.; Navarro, M.; Ingelmo, M.; Engel, P. Increased serum levels of soluble l-selectin (CD62L) in patients with active systemic lupus erythematosus (SLE). *Clin. Exp. Immunol.* **1999***, 119*, 169-174.
38. Girón-González, ‚J.A.; Rodriíguez-Ramos, C.; Elvira, J.; Galán, F.; Del Álamo, C. F-G.; Díaz, F.; Martiín-Herrera, L. Serial analysis of serum and ascitic fluid levels of soluble adhesion molecules and chemokines in patients with spontaneous bacterial peritonitis. *Clin. Exp. Immunol.* **2000***, 123*, 56-61.
39. [1]. Hartung, H.; Reiners, K.; Archelos, J. J.; Michels, M.; Seeldrayers, P.; Heidenreich, F.; Pflughaupt, K. W.; Toyka, K. V. Circulating adhesion molecules and tumor necrosis factor receptor in multiple sclerosis: Correlation with magnetic resonance imaging. *Ann. Neurol.* **1995***, 38*, 186-193.
40. Kubo, Y.; Ogasawara, K.; Kakino, S.; Kashimura, H.; Tomitsuka, N.; Sugawara, A.; Ogawa, A. Serum inflammatory adhesion molecules and high-sensitivity C-reactive protein correlates with delayed ischemic neurologic deficits after subarachnoid hemorrhage. *Surg. Neurol.* **2008***, 69*, 592-596.
41. McDonald, J.H. *Handbook of Biological Statistics*, 3rd ed; Sparky House Publishing; Baltimore, 2014.
42. Harris, D.C. *Quantitative Chemical Analysis*, 7th ed; W.H. Freeman and Company; New York, 2007, p 57-62.
43. Christoforidou, S.; Malissiova, E.; Gortzi, O.; Hadjichristodoulou, C. Comparative evaluation of ELISA kits' reliability for the aflatoxin M1 determination in goat milk. *Euro. Food Res. and Technol.* **2015***, 240*, 701-706.

44. Tate, J.; Ward, G. Interferences in Immunoassay. *Clin. Biochem. Rev.* **2004***, 25*, 105-120.
45. Revenant, M. C.; Beaudonnet, A. Serum ferritin determination by enzyme immunoassay: importance of sample dilution (the "Hook effect"). *Clin. Chem.* **1982***, 28*, 253-254.
46. Schiettecatte, J.; Anckaert, E.; Smitz, J. Interferences in Immunoassays. In *Advances in Immunoassay Technology*; Chiu, N. H. L.; Christopoulos, T. K., Ed.; InTech:2012, DOI: 10.5772/35797. Available from: http://www.intechopen.com/books/advances-in-immunoassay-technology/interference-in-immunoassays (accessed Aug 19, 2016).